University of Cincinnati

Date: 6/30/2015

I, Jason M. Cesta , hereby submit this original work as part of the requirements for the degree of Master of Science in Geology.

It is entitled:

Timing of alluvial fan development along the Chajnantor Plateau, Atacama Desert, northern Chile: Insights from cosmogenic 36Cl

Student's name: **Jason M. Cesta**

This work and its defense approved by:

Committee chair: Dylan Ward, Ph.D.

Committee member: Craig Dietsch, Ph.D.

Committee member: Lewis Owen, Ph.D.

17366

Timing of alluvial fan development along the Chajnantor Plateau, Atacama Desert, northern Chile: Insights from cosmogenic ^{36}Cl

A thesis submitted to the

Graduate School of the University of Cincinnati

in partial fulfilment of the

requirements of the degree of

Master of Science

in the Department of Geology

of the McMicken College of Arts and Sciences

by

Jason M. Cesta

B.S. (Geology), The Richard Stockton College of New Jersey,
May 2013

June, 2015
Cincinnati, OH

Advisory Committee:

Dr. Dylan J. Ward, Ph.D. (Chair)

Dr. Craig Dietsch, Ph.D. (Member)

Dr. Lewis A. Owen, Ph.D. (Member)

Keywords: Alluvial fans, debris flows, cosmogenic nuclides, Atacama Desert, central Andes

Timing of alluvial fan development along the Chajnantor Plateau, Atacama Desert, northern Chile: Insights from cosmogenic ^{36}Cl

Jason M. Cesta

Abstract

An extensive alluvial apron of coalescing gravel fans blankets the western flank of the Chajnantor Plateau in the Atacama Desert of northern Chile. Remnant alluvial surfaces, terraces, and intermittent debris flow deposits preserved in this bajada indicate multiple intervals of aggradation, incision and terrace abandonment, and deposition. The high preservation potential and sensitivity to climate shifts of the region provides a unique opportunity to elucidate the sedimentary response to climate variations at an extreme of Earth's climate. Cosmogenic ^{36}Cl exposure dating, aided by mapping, is used to establish a detailed chronology of the depositional history of the Chajnantor alluvial apron. Alluvial surfaces and gravel deposits yield cosmogenic exposure ages ranging from 20.7 ± 1.4 ka to 419.2 ± 39.6 ka. Debris flow boulders confined to modern and ancient channels yield cosmogenic exposure ages ranging from 9.3 ± 1.1 ka to 202.5 ± 19.6 ka. One localized (*Qcf1*) and two extensive (*Qcf2* and *Qcf3*) abandoned alluvial fan surfaces yield cosmogenic exposure ages of ~33 ka, ~55 ka, and ~145 ka respectively. These abandonment ages coincide with periods of moraine stabilization and deglaciation on the adjacent Chajnantor Plateau. Protracted periods of aggradation appear to coincide with periods of increased precipitation and glacial occupation of the Chajnantor Plateau, and are punctuated by phases of incision and surface abandonment during interglacial periods. Cosmogenic exposure ages reveal a transition from aggradation to incision during marine oxygen isotope stage II (MIS II). These results suggest that climate, specifically precipitation, is the dominant control on alluvial fan formation along the western margin of the Chajnantor Plateau.

Acknowledgements

Foremost, I would like to acknowledge my advisor, Dylan Ward, and my committee members, Lewis Owen and Craig Dietsch, for their continual support, guidance, and expertise throughoutmy Master's degree program. This manuscript benefited immeasurably from their reviews and suggestions. I express my thanks to Sarah Hammer, Joseph Radler, and Madhav Murarri for their patience and assistance with laboratory techniques. Thanks are due to Esteban Sagredo and Chris Sheehan for their assistance and discussion while in the field, and to the rest of the faculty, staff, and graduate students in the Department of Geology at the University of Cincinnati.

Grant Information

This work was supported by grants from the National Science Foundation (EAR-1226611) awarded to J. Galewsky and D. Ward and the Geological Society of America (10482-14) awarded to J. Cesta

Table of Contents

List of Figures

List of Tables

Chapter 1: Introduction and Background

1.1 Introduction

One of the foremost concerns to the geomorphology community is the response of landscapes to climate change, particularly over Quaternary timescales (National Research Council, 2010). Landscapes provide a record of how surface processes interact over geologic timescales, and how they are influenced by tectonics and climate while their modification in the present offers insight into modern, active processes. A detailed examination of Quaternary landscapes and their generation or degradation through time offers insight into how surface processes, and thus the landscapes themselves, respond to external forcing. Fluvial landscape evolution and alluvial landforms (e.g. strath terraces and fans) appear to be particularly sensitive to tectonic and climatic forcing (Ritter et al., 1995; Harvey et al., 1999; Ritter et al., 2000; Hartley et al., 2005).

Alluvial fans are landforms associated with deposition along mountain fronts where valleys go from confined to unconfined, and at transitions to lower gradients. They are typically fan-shaped in map view and composed of relatively thick (10's of meters) gravel and sand packages dissected by fluvial channels. Alluvial fans form under an array of climatic and geomorphic settings and are controlled by autogenic depositional processes that vary spatially and temporally (Ventra and Nichols, 2014), as well as external factors such as climate and tectonics (Bull and Schick, 1979; Viseras et al., 2003; Haug et al., 2010; Enzel et al. 2012). The processes that exert control on the timing and rate of formation of alluvial surfaces are often debated, and vary from region to region. Tectonics, climate, paraglacial, and periglacial processes have been suggested as the primary drivers of alluvial surface development (Church and Ryder, 1972; Ritter et al., 1995; Hall et al., 2008; Dorn 2009). The coupling of several variables in time and space such as sediment supply, source area lithology, tectonics, climate, base-level change, etc., adds spatial and temporal complexity to the deposits, and often inhibits deciphering the contribution of a specific variable on the development of an alluvial system (Hartley et al., 2005). In arid and hyper-arid environments climatic change, specifically changes in precipitation, has been implicated as the primary

driver on the evolution of alluvial fans, particularly regarding the transition from phases of aggradation to periods of stability (Gunster and Skowronek, 2001; Dorn, 2009; Enzel et al., 2012; McPhillips et al., 2013). For example, an increase in precipitation could lead to increased runoff from adjacent slopes and incision of alluvial fan deposits, or an increase in precipitation could liberate more sediment in the headwaters of the catchment and promote an aggradational response in the alluvial apron.

Establishing detailed chronologies for stratigraphic relationships among deposits in an alluvial system is required to constrain the influence of primary drivers (e.g. climate) on fan surface development. Geomorphic and stratigraphic relationships among alluvial deposits can be influenced by changes in climate at the local, regional, and global scales. Correlations between periods of development and abandonment of alluvial surfaces and local, regional, or global climate events can be evaluated through the use of independent climate records. Such comprehensive chronologies achieved either on local or regional scales can then be utilized in paleoclimate and tectonic studies, particularly in regards to their ability to provide additional constraints on climatic or tectonic events (Hedrick et al., 2013).

Arid environments exhibit high precipitation variability, typically on the order of 100 to 300 mm of precipitation annually. In contrast, hyper-arid environments such as the Atacama Desert of northern Chile receive less than 100 mm of annual precipitation. The high preservation potential and sensitivity to climate shifts of arid and hyper-arid alluvial systems provides an excellent opportunity to test the influence of climatic events on the timing of alluvial surface development (Enzel et al. 2012). The Atacama Desert provides a unique opportunity to gain insight into the sedimentary response to precipitation at an extreme of Earth's climate (Fig. 1-1, 1-2). Previous studies in arid regions have primarily utilized relative age dating techniques such as surface morphology, soil development, and weathering parameters to assign relative ages to alluvial surfaces (Bull, 1977; Wells, 1977; Bull and Schick, 1979; McFadden et al., 1989). Until recently the paucity of numerical ages for arid alluvial fans stemmed from the exclusion of the standard numerical dating techniques – radiocarbon geochronology and optically stimulated luminescence – due to the sparse availability of organic matter and fine sand

lenses. Recent advances in terrestrial cosmogenic nuclide (TCN) surface exposure dating (e.g. using ^{10}Be, ^{36}Cl, ^{26}Al, ^{3}He, ^{21}Ne) has: 1) allowed for the assignment of numerical ages to surfaces and deposits that were ineligible for previous numerical dating techniques, and 2) expanded the array of Quaternary landforms suitable to numerical dating techniques (e.g. Gonzáles et al., 2006; Frankel et al., 2007; Hall et al., 2008; Placzek et al., 2010; Jungers et al., 2013; Owen et al., 2014; Sarikaya et al., 2015).

1.2 Geologic and Climatic Setting

1.2.1 Geologic Setting

The Atacama Desert of northern Chile is located between the Pacific Ocean and the central Andes, in the active Andean forearc. Four major morphotectonic divisions are defined in the Andean forearc region: the Coastal Cordillera, the Central Depression, the Cordillera Domeyko, and the Andean Flank (Fig. 1-1). The Andean Cordillera as a whole comprises a number of distinct volcanic provinces along the Andean chain. The Central Volcanic Province (CVZ) of the Central Andes extends from 14° to 28° S and hosts extensive Tertiary ignimbrite provinces (de Silva, 1989). The late Tertiary Altiplano-Puna Volcanic Complex of the CVZ extends from 21° to 24° S and hosts widespread volcanic deposits. Over the last 10 million years, the volcanics have been dominated by dacitic ignimbrites that form extensive ignimbrite sheets (de Silva, 1989; Schmitt, et al. 2001). A number of these eruptive units form broad volcanic "shields" or "domes" that define extensive, isolated plateaus along the Andean chain.

The Chajnantor Plateau (23° S, 67° W) is a late Cenozoic, arid, volcanic plateau set within the framework of the subtropical Andes Mountains (Fig. 1-3, 1-4). The plateau reaches elevations of 5,000 m above sea level (asl), and is adorned by a number of more recent volcanic peaks that range in elevation from 5,600 to 5,900 m asl. A major succession of ignimbrites associated with the 4.5 – 4.1 Ma eruptions of the La Pacana caldera form the core of the plateau (Gardeweg and Ramírez, 1987; Lindsay et al., 2000). This older sequence of ignimbrites is overlain by the Purico complex, which comprises an apron of three ignimbrite flow units. The Lower Purico Ignimbrite, designated the Cajón Ignimbrite by Guest

(1969) and later by Gardeweg and Ramírez (1982, 1987), is the most extensive of the flow units, and caps the majority of the western Chajnantor Plateau (Schmitt et al., 2001). The Cajón Ignimbrite has been dated by yielding an eruption age of 1.38 ± 0.07 Ma. A number of post-ignimbrite stratovolcanoes and domes overlie the Purico Complex, however, radiometric ages for them are generally lacking. The moderately pristine morphology and high degree of preservation of the post-ignimbrite stratovolcanoes and domes implies relatively young ages for them, < 0.5 Ma as suggested by Francis and others (1984). Schmitt and others (2001) suggest post-glacial formation for two of the volcanic peaks, C. Aspero and C. Chascon. The ignimbrite sheets dip away from the vent at approximately 4°, generating the broad, dome-like structure of the plateau (Schmitt et al., 2001).

Neighboring the western margin of the Chajnantor Plateau, the Salar de Atacama Basin is located in the active Andean forearc between the Cordillera Domeyko and the western flank of the Andean Cordillera (Fig. 1-1, 1-3). The basin extends from 22.5° S to 24.5° S, and is located in a region that has been subjected to subsidence since the Paleozoic (Ramírez and Gardeweg, 1982; Hartley et al., 1992a). The center of the basin is occupied by the modern Salar de Atacama salt flat. An 8 km thick succession of nonmarine strata provides a nearly complete record of Cenozoic sedimentation (Bobst et al., 2001; Lowenstein et al., 2003; Arriagada et al., 2006; Jordan et al., 2007). There is considerable debate over the tectonic evolution of the Salar de Atacama Basin, and several conflicting models are described in the literature. Arriagada and others (2002) and Mpodozis and others (2005) suggest that the Salar de Atacama Basin developed during the Late Cretaceous following the inversion of the Tarapacá back arc basin. Uplift of the Cordillera Domeyko occurred as a consequence of the tectonic closure and inversion of the Tarapacá basin (Jolley et al., 1990; Pananont et al., 2004). Other authors argue that the basin evolved under extensional conditions for the entirety of the Mesozoic and Cenozoic (Flint et al., 1993) or initiated during an extensional regime which later transitioned to compression (Muñoz et al., 1997).

Along the western flank of the Chajnantor Plateau, a broad bajada extends from the base of the plateau to the margin of the Salar de Atacama salt flat (Fig. 1-3, 1-4, 1-5). The coalescing gravel fans of

this alluvial apron emanate from large bedrock canyons (*quebradas*) and smaller, fracture-controlled bedrock channels that have incised into the volcanic stratigraphy of the plateau. Hoke and others (2004) propose a groundwater sapping mechanism for the large quebradas, and argue that the smaller channels formed prior to the onset of aridity in the region ca. 5.8 Ma. Irwin and others (2014) propose flood erosion of strong-overlying-weak stratigraphy and flood erosion of vertically jointed rock as two other mechanisms of quebrada formation. The origin and mechanisms of formation of the smaller channels that appear in the study area are enigmatic; however they must postdate the 1.38 Ma Cajón Ignimbrite (Fig. 1-5). Recent work has shown that wind abrasion plays a significant role in modifying channel morphology and extending bedrock canyons (Perkins et al., 2015). The gravels that constitute the alluvial fans are predominantly andesitic, and are sourced from the andesitic peaks and volcaniclastic deposits (e.g. lahars) on the higher reaches of the plateau. Along the base of the plateau, remnant alluvial surfaces and terraces stand proud (10 – 15 m) of the modern channel surface, and multiple intervals of incision, terrace abandonment, and deposition are apparent. Younger fluvial activity has incised into these surfaces and terraces, and in these young channels numerous debris flow deposits (Fig. 1-5). These debris flows contain multiple lobes which consist of tens of meter long trains of 0.5 to 2.0 m boulders, suggesting an amalgamation of discrete events into an expansive deposit. On the ignimbrite plateau, intermittent broad gravel fans remain perched, and stratigraphic sections of these gravels suggest multiple stages of deposition (Fig. 1-5). These deposits may indicate volcaniclastic, glacial, or glaciofluvial generation or mobilization of sediment that has subsequently been reworked and removed from regions of the ignimbrite surface. Age constraints on the alluvial deposits along the western flank of the Chajnantor Plateau are sparse, but these deposits have been mapped as Quaternary alluvium or Quaternary gravels (Ramírez and Gardeweg, 1982; Marinović and Lahsen, 1984).

1.2.2 Climatic Setting

The extreme paucity of precipitation in the Atacama Desert is the result of several factors (Fig. 1-2). These include: (1) the Atacama lies in the Andean rain shadow which inhibits moisture from the

Atlantic (Houston et al., 2006); (2) its proximity to the descending limb of the Hadley circulation, resulting in the subtropical high pressure belt (Houston and Hartley, 2003); (3) the Humboldt Current and upwelling cold water to the west limits the evaporation of ocean water (Caviedes, 1973; Houston et al., 2006; Amundson et al., 2012); and (4) a regional circulation of subsiding air along the Altiplano (Houston et al., 2006). The seasonal precipitation observed along the western Andean flank is a consequence of the South American Summer Monsoon (SASM) which controls the position of the Bolivian High and the incursion of extratropical precipitation events derived from the Atlantic (Lenters and Cook, 1997). These occur in the form of austral spring and summer storm events (Rech et al., 2003; Mather and Hartley, 2005; Houston, 2006; Placzek et al., 2009). Winter precipitation may also occur, especially during El Nino years (Garreaud and Aceituno, 2001; Vuille, 1999).

The mean annual temperature of the Chajnantor Plateau ranges from -3° to -4 °C while the mean annual temperature of the central Atacama spans 10° to 15°C at ~3,000 m (Latorre et al., 2003). Modern precipitation in the Altiplano region displays a steep precipitation gradient. On the upper reaches of the Chajnantor Plateau (4,500 m asl) precipitation averages ~200 mm yr^{-1}, which diminishes westward to < 20 mm yr^{-1} along the western slope (2,500 to 3,000 m asl) and < 10 mm yr^{-1} in the Salar de Atacama Basin (2,000 m asl; Latorre et al., 2003; Rech et al., 2003, Placzek et al., 2014).

There is considerable debate regarding the timing of the onset of hyperaridity in the Atacama Desert, and a number of postulations exist in the literature. Hoke et al. (2004), Clark (2005), Dunai et al. (2005), Nishiizumi et al. (2005), Nalpas et al. (2008), Rech et al. (2006), Placzek et al. (2014), and others argue for a Miocene onset of hyperarid conditions. Others propose a Pliocene-Pleistocene onset of hyperaridity in the region (Hartley and Chong, 2002; Amundson et al., 2012; Jungers et al., 2013). Many recent studies have challenged the longstanding view that the central Atacama is a static, relict landscape with minimal to negligible Quaternary modification. Placzek and others (2010, 2014), Amundson and others (2012), and Jungers and others (2013) offer evidence for a dynamic landscape in the central Atacama that has been subject to significant modification on Pleistocene and Holocene timescales. Indeed

the hyperaridity of the central Atacama Desert, particularly in the region encompassing the Salar de Atacama and the adjacent Chajnantor Plateau, has been punctuated by periods of increased precipitation throughout the Quaternary. Regional paleoclimate records that show increased precipitation include salt cores from the Salar de Atacama and the Salar de Uyuni in adjacent Bolivia (Bobst et al., 2001; Baker et al., 2001), sediment cores from high altitude lakes (Geyh et al., 1999; Grosjean et al., 2001; Placzek et al., 2006, 2013), and rodent middens and paleowetland deposits (Betancourt et al., 2000; Rech et al., 2002; Latorre et al., 2003; Quade et al., 2008; Díaz et al., 2012).

The Salar de Atacama salt core records wet and dry phases of the salar over the past 106 ka (Bobst et al., 2001). Prominent wet phases appear at ~70 ka, ~45 ka, ~20 ka, 16-14 ka, and 3-6 ka, which are substantiated by synchronous records from the Salar de Uyuni and the Sajama ice core (Baker et al., 2001). Lake records within the Uyuni Basin also suggest the presence of shallow lakes between ~95 and ~80 ka (Placzek et al., 2009). Archives of paleowetland deposits and high altitude saline lakes support these wet phases at times when their ages overlap, in addition to suggesting that the Salar de Atacama has experienced intermittent wet phases throughout the Holocene (Latorre et al., 2005; Grosjean et al., 2001; Rech et al., 2002; Rech et al., 2003; Quade et al., 2008). These paleoclimate proxies argue for periods of increased precipitation during the Last Glacial Maximum (~26.5-22 ka), deglacial to early late glacial (~17.5-15 ka), and late glacial times (~13-10 ka). In addition, recent evidence from the Chajnantor Plateau suggests multiple stages of glacial occupation (Ward et al., in review). Mapping and surface exposure dating of glacial landforms and scoured bedrock on the southern Altiplano and Chajnantor Plateau by Ward and others (in review) suggests at least three periods of moraine stabilization. Deposits associated with Stage III stabilization likely formed prior to ~100 ka. Stage II deposits suggest stabilization around ~50 ka, with continued glaciation or reglaciation around ~30-25 ka suggested by Stage I deposits. On the basis of this chronology, Ward and others argue for glaciation of the Chajnantor Plateau ca. 50 ka, with reglaciation or continued glaciation until ~30 ka, followed by deglaciation by ~25 ka. The glacial chronology on the southern Altiplano is synchronous with wet phases indicated by

paleoclimate archives and correlations with regional glaciations, suggesting an easterly moisture source (Ward et al., in review).

1.3 Scientific Problem

An extensive surficial record of discrete sedimentation events is preserved within the bajada along the western flank Chajnantor Plateau. Among the coalescing gravel fans of the alluvial apron there, remnant alluvial surfaces, terraces, and intermittent debris flow deposits indicate multiple intervals of incision, terrace abandonment, and deposition (Fig. 1-5). These well-preserved landforms provide a unique opportunity in which to understand the sedimentary response to precipitation at the hyperarid extreme of Earth's climate. The limited exposure ages available for individual cobbles and boulders among these preserved surfaces are relatively young, suggesting active Quaternary landscape modification (Placzek et al., 2010, 2014). In order to elucidate the primary drivers of alluvial development and modification along the Chajnantor Plateau, it is necessary to construct a detailed chronology of the remnant alluvial surfaces, terraces, and intermittent debris flow deposits.

Numerical ages for the remnant alluvial surfaces would permit the correlation of disjointed deposits and offer understanding the chronology of filling and downcutting events. Once established, the chronology of aggradation and incision can be compared to regional paleoclimate archives to assess the influence of local, regional, and/or global climate shifts. If the aggradation and development of the alluvial fans is coincident with wet phases of the salars and an abundance of paleowetland deposits, an increase in mean annual precipitation or an increased frequency of storm events may induce alluvial fan formation (Bull and Schick, 1979; Enzel et al., 2012). If these deposits are not synchronous with known periods of increased precipitation, perhaps their formation is controlled by large scale climate oscillations, or exclusive of climate modulation altogether. Furthermore, if aggradation is coeval with glacial occupation of the adjacent plateau, a linkage between alluvial fan development and glaciation or deglaciation is suggested (Church and Ryder, 1972; 1989). Fan development concurrent with deglaciation

would imply a paraglacial cycle of sediment supply, which would be followed by a diminishing sediment supply and subsequent fan entrenchment. If this is the case, a progression from alluvial fan development to incision and debris flow events suggests the transition from a transport-limited to supply-limited system. These correlations would offer insight to how these sedimentary systems respond to precipitation in an area where they should be less sensitive to other variables (e.g. vegetation and temperature changes) which modulate sediment production and storage in many settings, allowing us to isolate the influence of precipitation on alluvial systems. Moreover, resolving the major drivers of fan development in the central Atacama has implications for the controls on Quaternary landscape modification in arid regions globally.

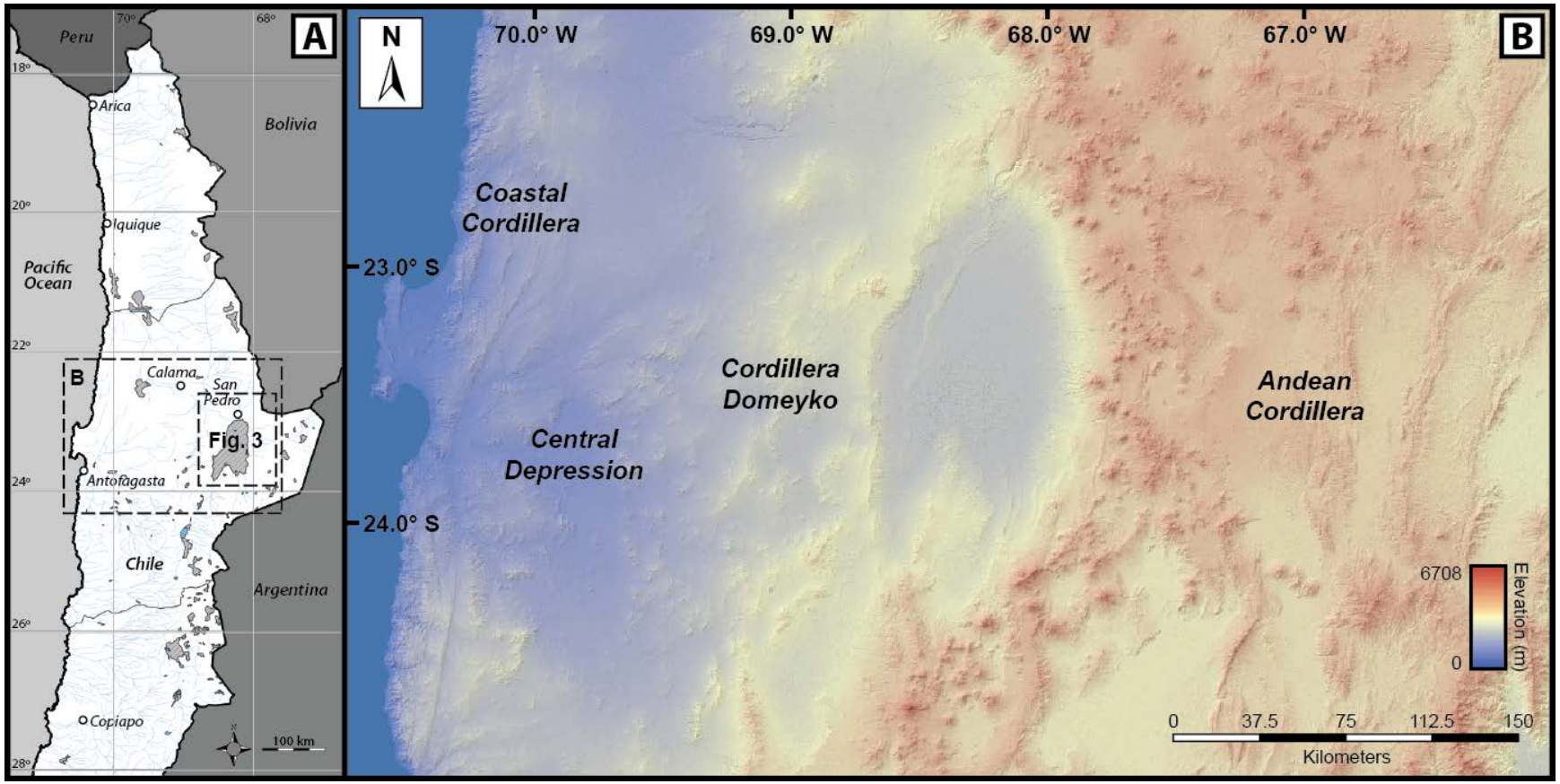

Figure 1-1: Regional maps of the study location. **A**. Location map of the study area in the subtropical Andes of Chile. Dashed boxes denote the extent of Fig. 1-1 B and Fig. 3. **B**. Regional digital elevation map of the central Atacama Desert with major morphotectonic divisions labeled. Shaded relief base image from ASTER (30 m resolution).

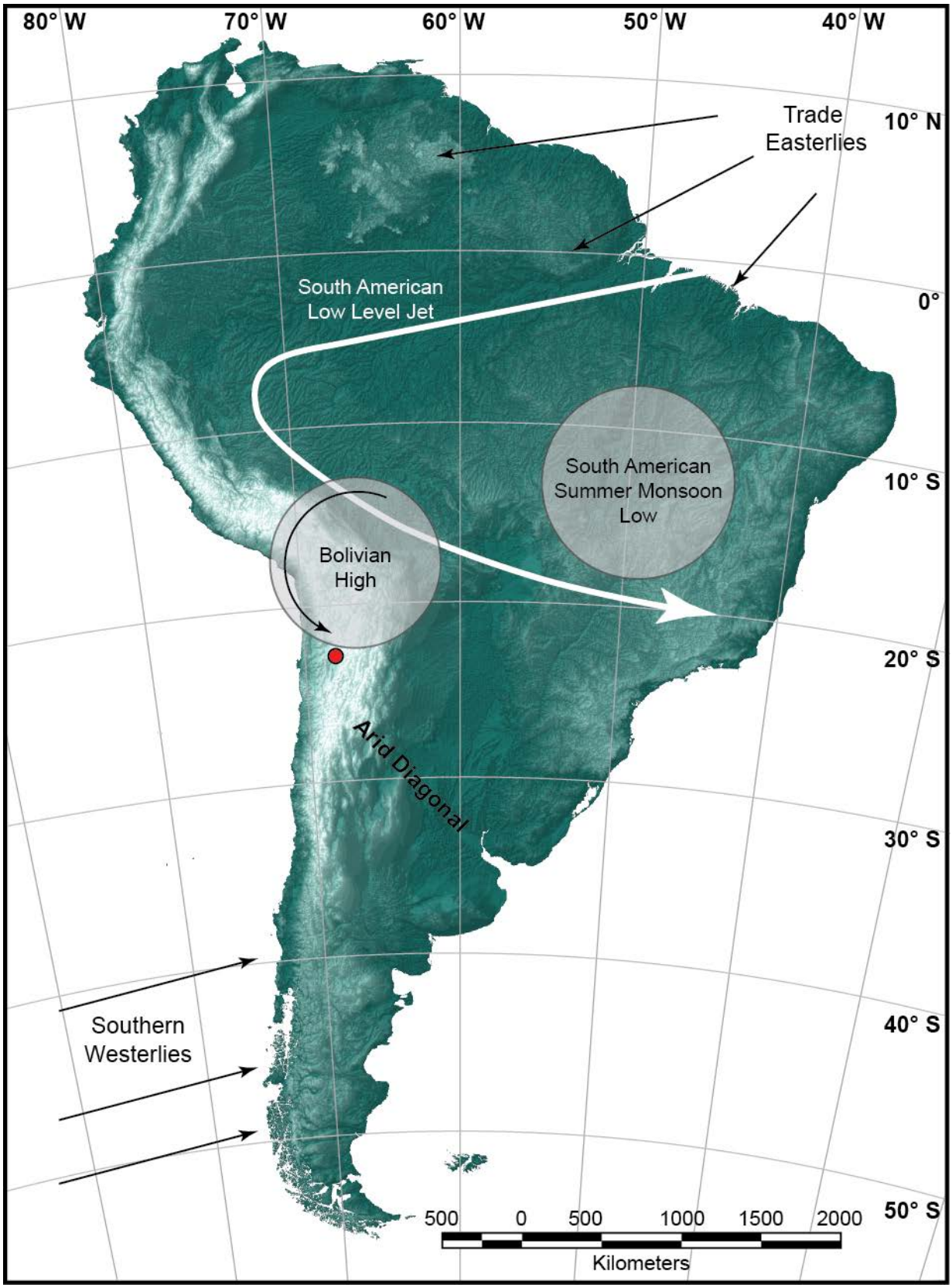

Figure 1-2: Modern climate features of South America. Study area indicated with a red circle.

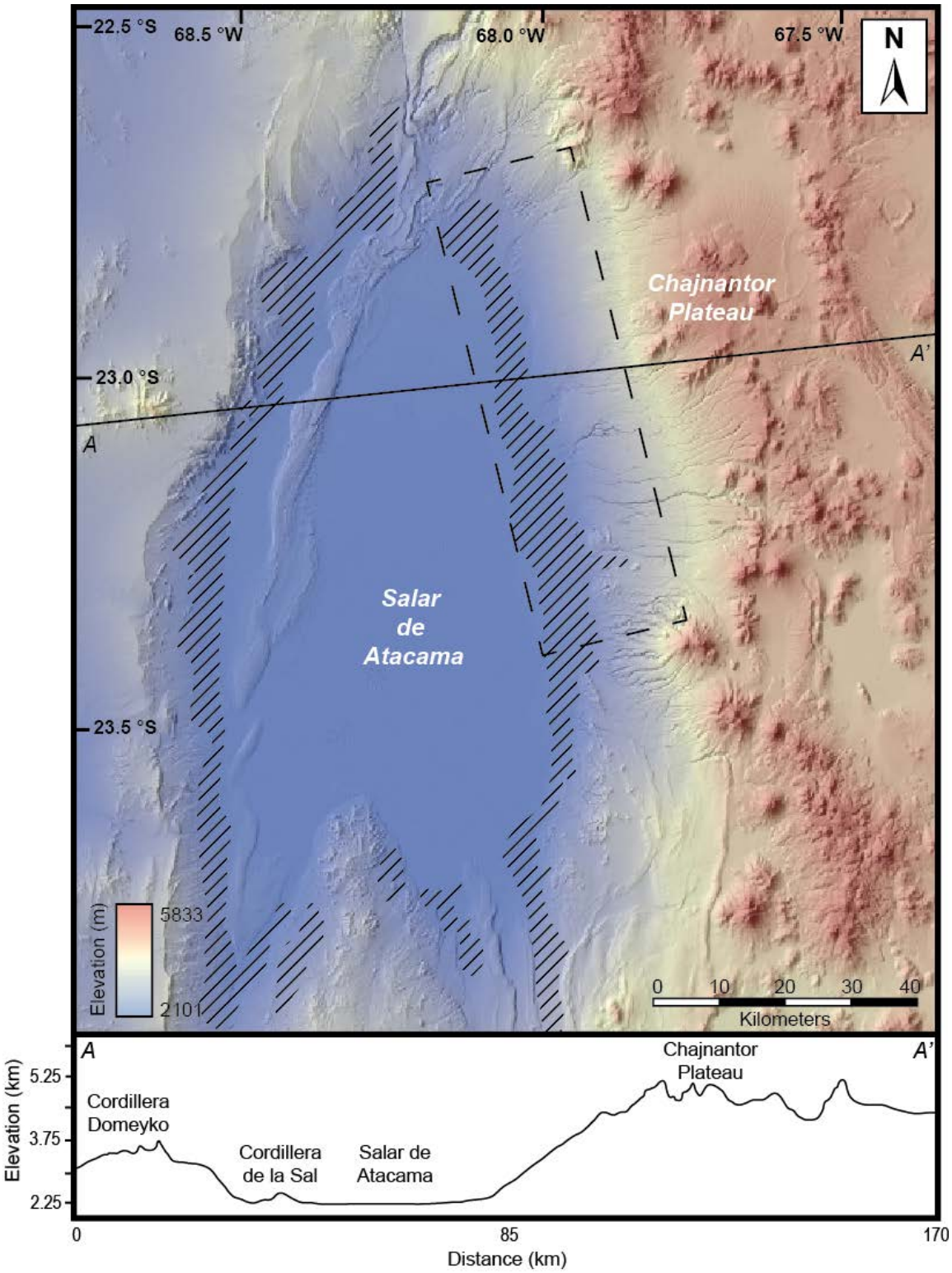

Figure 1-3: Shaded relief map of the Salar de Atacama Basin and surrounding features (ASTER 30 m resolution). Dashed box outlines the location of the study area. Diagonal lines indicate alluvial deposits along the margins of the salar and the western Altiplano. Elevation profile shows representative topography.

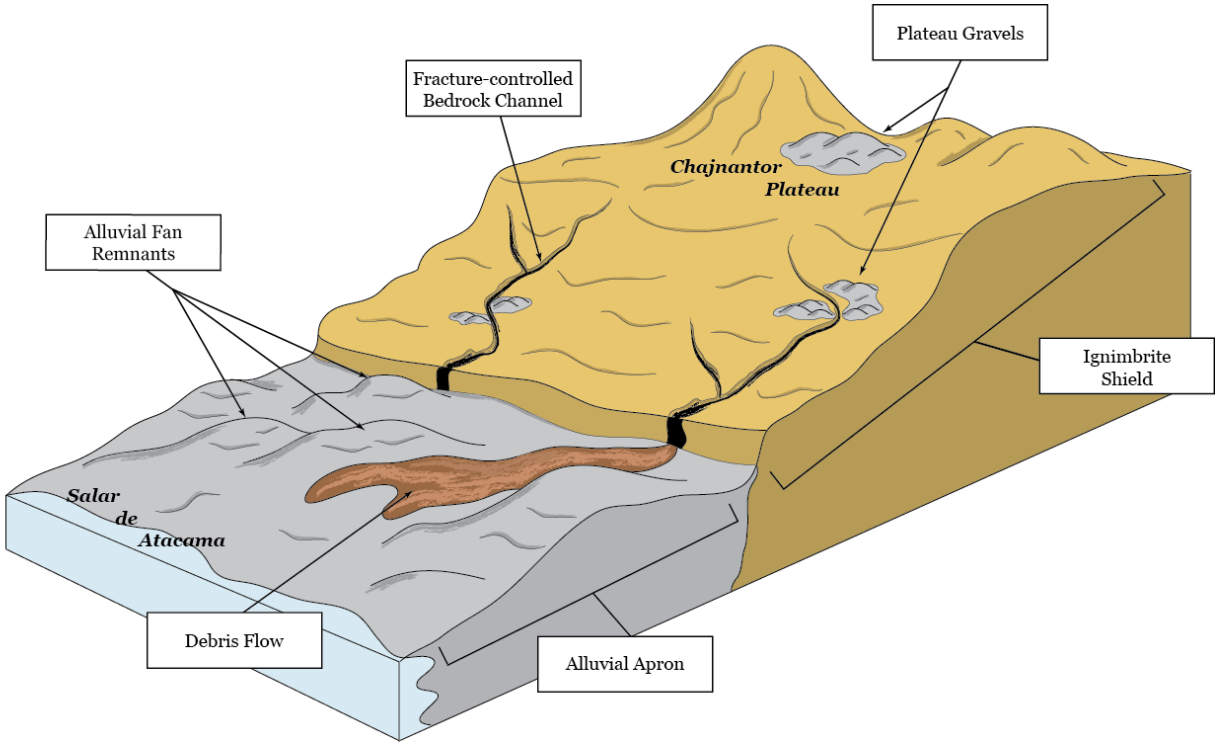

Figure 1-4: Schematic diagram illustrating the general geomorphic landforms and features of the study area.

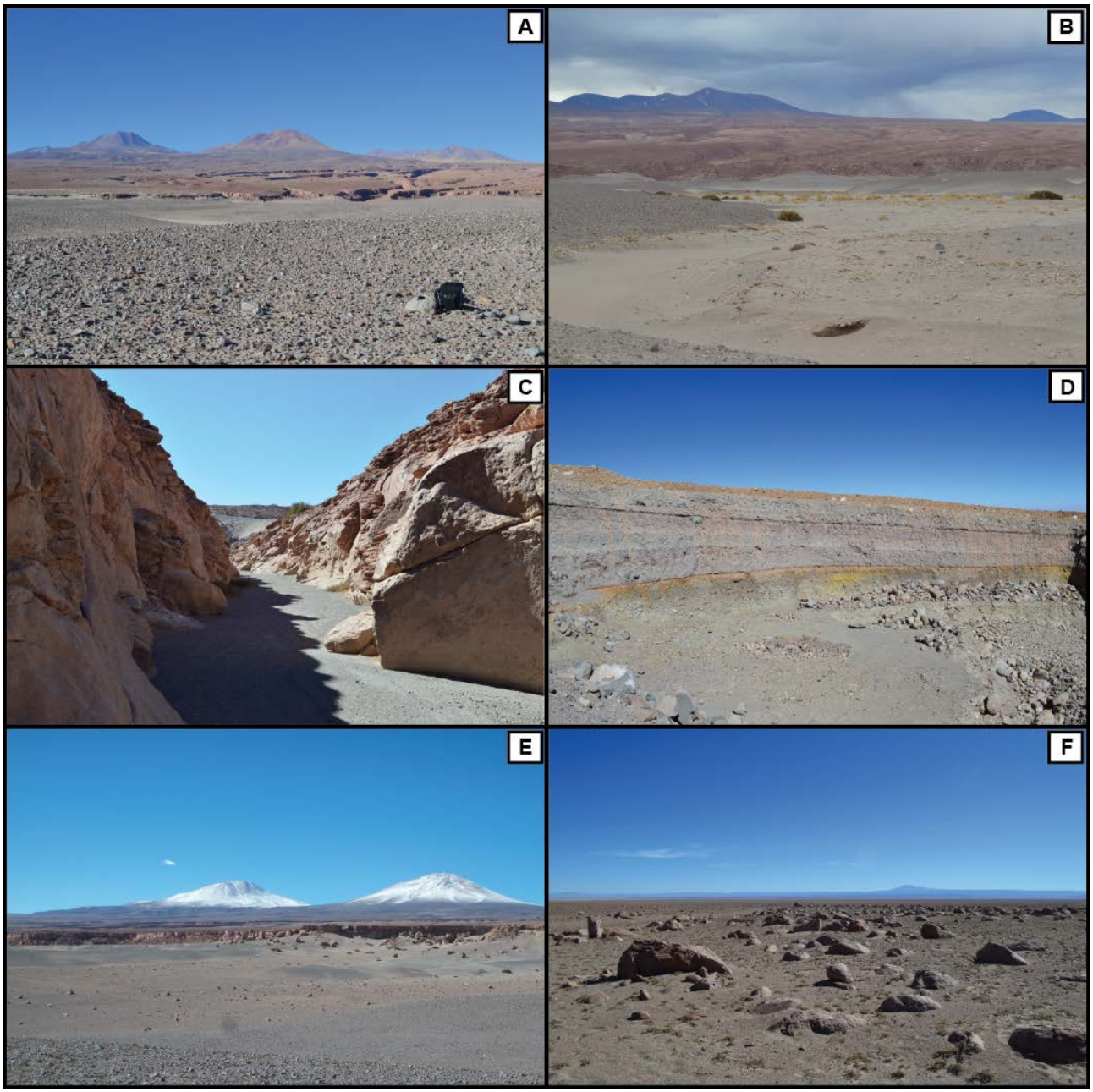

Figure 1-5: General geomorphic features of the study area. **A**. Chajnantor Plateau in the distance featuring incised bedrock channels and volcanic peaks C. Negro and C. de Macón. Alluvial gravels of the adjacent bajada in the foreground. **B**. Modern channel downcutting through the coalescing alluvial fans, vegetation suggests presence of minor groundwater. **C**. Bedrock channel carved into the ignimbrite shield, note sedimentary fill along the floor of the channel. **D**. Alluvial deposits preserved on the Chajnantor Plateau below C. Toco. **E**. Debris flow deposits entrained in downcut channels among remnant fan surfaces. **F**. Typical boulder field associated with debris flows.

Chapter 2: Aerial Mapping and Morphometrics

2.1 Introduction

Satellite imagery was used to construct a generalized map of alluvial deposits preserved on the plateau and abandoned fan surfaces and debris flow deposits of the alluvial apron. A suite of weathering and erosion parameters were measured on several surfaces to assess the utility of using relative age dating techniques to differentiate these Quaternary deposits, in addition to providing support to the absolute chronology of surface exposure ages.

2.2 Aerial Mapping

Geologic maps (Ramírez and Gardeweg, 1982; Marinović and Lahsen, 1984) and satellite imagery were utilized to identify remnant alluvial surfaces and debris flow deposits. These features were then used to construct a generalized map of alluvial deposits along the Chajnantor Plateau. Detailed examination of the identified surfaces and deposits was completed in the field. Morphology, location, and stratigraphy of remnant alluvial surfaces suggest allowed three broad surfaces to be mapped: Pls1, Qs1, and Qs2 (Fig. 2-1).

Isolated Pliocene gravel deposits (Pls1), mapped by Marinović and Lahsen (1984) as the Vilama Formation (3.7 ± 1.0 Ma, Mpodozis et al., 2000), are preserved along the northern margin of the plateau, overlying the Chaxas ignimbrite (4.0 ± 0.1 Ma, Salisbury et al., 2010). The Pliocene gravels are composed of limestone, claystone, and sandstone clasts with volcanic fragments, and are deeply incised and disjointed. Discontinuous, broad Pleistocene gravel and lahar deposits (Qs1) are preserved erratically along the upper reaches of the plateau. The Qs1 deposits are generally well preserved on the higher elevations of the ignimbrite shield, and become considerably fragmented, dissected, and incised at lower elevations. Andesitic clasts dominate the lithologies, and several deposits suggest multiple periods of deposition (Fig. 1-5). Reworked gravels sourced from these perched Pliocene and Pleistocene deposits coalesce along the base of the plateau and delineate the youngest regional surface (Qs2). These extensive

coalescing Qs2 fans show evidence of multiple periods of deposition, suggesting a complex history: younger fans, recognized by their relatively continuous surfaces overlie am older, dissected alluvial surface. Delineation of these multiple depositional events requires detailed mapping and the acquisition of numerical ages for the surfaces to resolve the timing of their formation.

Several boulder fields were identified in channels incised into the alluvial apron along the base of the plateau. These boulder fields are interpreted as amalgamated debris flow deposits (Qd1), and are stratigraphically and morphologically distinct from the adjacent Qs2 fan surfaces (Fig. 2-1). The Qd1 deposits are entrained in contemporary channels incised up to 10 meters below the adjacent Qs2 abandoned alluvial surfaces. The association of the Qd1 deposits with modern, active channel surfaces suggests they formed relatively recently, in contrast to adjacent Qs2 fan surfaces and terraces. The active alluvial surface and modern alluvium were designated as Qm. All of the mapped surfaces and deposits provide evidence for a complex depositional history, and illustrate substantial modification of the landscape during the Quaternary.

2.3 Morphometrics

Prior to the advent of numerical dating methods that could be applied to these geologic deposits, geomorphic surfaces were correlated or differentiated though the use of multi-parameter relative-age dating (RA) techniques pioneered by Blackwelder (1931), Sharp and Birman (1963) Burke and Birkeland (1978), and McFadden and others (1989). These techniques work on the basis that the weathering properties of lithologically similar deposits in analogous climatic and geomorphic settings are time dependent (Burke and Birkeland, 1979; McFadden et al., 1989). Morphometric properties employed in RA dating techniques aid in validating terrestrial cosmogenic nuclide surface exposure ages, and provide additional parameters for correlation of surface deposits. The RA dating techniques and parameters described in Burke and Birkeland (1979) and McFadden and others (1989) were slightly modified and

applied to the disjointed Qs2 alluvial surfaces and Qd1 debris flow deposits observed along the western margin of the Chajnantor Plateau.

2.3.1 Relative Age Dating Parameters

Descriptions of several weathering and erosion parameters were taken or modified from McFadden and others (1989) and are outlined here.

Percent Rounded: Surface clasts exposed to weathering become progressively more rounded with time (Fig. 2-2). Alluvial surface pebbles and debris flow boulders are classified as angular, subangular, subrounded, or rounded.

Percent Pitted: Pits are defined as concave depressions on the surface of the boulder resulting from granular disintegration. A clast is considered to be pitted if the surface exhibits one or more pits. Pit depth is measured from the bottom of the pit to the surface of the boulder, and is expressed as the maximum pit depth for the deposit, and the average depth of the pits for all clasts in the deposit.

Percent Fractured: A clast is classified as fractured if it exhibits one or more planar cracks exclusive of surface spalling (Fig. 2-2). The fracture ratio is expressed as fractured clasts ÷ nonfractured clasts.

Grain Relief: Surface weathering produces single mineral grain relief, where resistant mineral grains stand proud of the clast surface. A clast must display single grain relief on ≥ 25 percent of the exposed surface to be considered to have grain relief. Single mineral grain relief is expressed as the maximum relief for the deposit and the average grain relief for all clasts in the deposit.

Ventifaction: A clast is considered to be ventifacted if one or more surfaces display aeolian abrasion. In the study area, ventifaction manifests on andesitic and ignimbrite clast surfaces as protruding "fingers" of material preserved behind more resistant mafic inclusions (Fig. 2-2). Ventifaction orientation was determined by measuring the trend of these protruding "fingers", and was primarily utilized to assess whether the clast has been subject to post-deposition reorientation.

2.3.2 Methodology

Observations in the field suggest the Qs2 alluvial surface encompasses multiple periods of surface abandonment and reactivation. These disjointed surfaces and intermittent debris flows suggest a complex history of deposition and incision. The entire suite of weathering and erosion parameters was utilized in an attempt to further delineate and classify the Qs2 surfaces. These parameters were measured on several representative sites, located on abandoned alluvial surfaces and amid boulder field deposits (Fig 2-3).

On abandoned alluvial surfaces, 30 m by 30 m quadrants were established on a suitable, representative section and care was taken to avoid surfaces that displayed evidence of disturbance. For each site, 100 pebbles with intermediate axes ≥ 1.5 cm were selected by random-walk sampling. These clasts were measured for intermediate axis length and assessed for angularity, pitting, ventifaction, and lithology. On each boulder field, a representative distal and proximal 30 m by 30 m quadrant was established, and all boulders with intermediate axes ≥ 30 cm were included in the analysis. For each eligible boulder, several weathering parameters were measured: long, intermediate, and short axes, angularity, lithology, pitting, pit depth, ventifaction, ventifaction orientation, height of single mineral grain relief, and fracturing. Measurements of length were made with a ruler with an estimated precision of ± 1.0 mm. Data was collected on bench sheets and digitized upon returning from the field. Means for each weathering parameter were determined on the respective surfaces. These means were then compared among the surfaces sampled to determine if meaningful trends in weathering were apparent.

2.3.3 Results

Generally, weathering parameters among alluvial surfaces were comparable and values between different sampling sites were reasonably clustered. Clast angularity ranged from 48 to 80 percent rounded, with six of the seven sampling sites displaying values between 48 to 62 percent rounded. Percent of pitted clasts ranged from 11 to 83 percent, with five of the seven sampled surfaces displaying

values that fall between 51 and 66 percent. Across alluvial surfaces, average intermediate axes measurements on cobbles ranged from 2.8 to 8.8 cm. The percent of ventifacted cobbles displayed a spread of values between sampled surfaces, ranging from 7.0 to 84.0 percent, but clustering of values among surfaces was not apparent. Angularity and pitting among sample locations were generally comparable across sampling locations, with notable exceptions at sites Qs2a2 and Qs2b2. Values for weathering parameters from sampling site Qs2b2 were consistently greater than those observed at the other sampling sites.

Due to the presence of andesite and ignimbrite lithologies in the boulder field deposits, weathering parameters for sampling locations were assessed independently for the two different rock types. Ignimbrite boulders were observed in all boulder field deposits sampled, while andesite boulders were only observed in four of the deposits. Where andesite boulders were present, weathering parameters were fairly consistent across the deposits. A wider range of weathering parameters was observed on the ignimbrite boulders across the deposits.

On andesite lithologies, boulder angularity ranged from 71 to 81 percent rounded across the sampling sites. Percent of pitted boulders ranged from 66 to 68, with pit depths falling between 0.18 and 0.27 cm. Fracturing of andesite boulders ranged from 0 to 23 percent across sampling sites. Across sampled boulder fields, average mean intermediate axis measurements on andesite boulders ranged from 36.7 to 55.7 cm. For ignimbrite boulders, boulder angularity ranged from 41 to 83 percent rounded across the sampling sites. The percent of pitted ignimbrite boulders ranged from 44 to 69, with pit depths falling between 0.14 and 0.64 cm. Ignimbrite boulders displaying fractures ranged from 14 to 35 percent across sampling sites. Across sampled boulder fields, average mean intermediate axis measurements on ignimbrite boulders ranged from 44.9 to 87.4 cm.

Examination of clasts on seven alluvial fan surfaces and seven boulder field deposits did not reveal any clear trends with stratigraphic position i.e. relative age indicators on alluvial surfaces that

appear to be stratigraphically younger show no clear distinction from those on older surfaces (Fig. 2-4, Table 2-1). Similarly, weathering parameters across boulder field deposits do not reveal consistent trends to allow a time progression to be defined (Fig. 2-5, Table 2-2). Raw weathering parameter data are included as Appendix A.

2.3.4 Conclusions

The relative-age method lacks the resolution to differentiate between surfaces and deposits of Pleistocene age in the study area. Clast weathering data do not allow surfaces and deposits to be discriminated through the RA parameters utilized in this study. It is possible that the RA technique was inadequate at delineating surfaces of differing ages because an insufficient amount of time has elapsed to develop a clear age progression among deposits or that the age differences among the surfaces and deposits sampled are small. It is also conceivable that differences in clast size among deposits diminished any observable trends due to the sensitivity of rock weathering parameters to particle size (McFadden et al., 1989). An alternative conclusion is that the Qs2 surfaces are similar in age and the "noise" observed in the weathering parameters results from surface reworking. The absence of a clear age progression among the debris flow boulder fields could be attributed to the fact that each debris flow deposit is composed of multiple depositional events, and each subsequent event would introduce relatively unweathered clasts into the deposit, dampening the weathering signal. McFadden and others (1989) found that soil characteristics and varnish cover did allow for the discrimination of late Pleistocene and Holocene surfaces in the Mojave Desert of California. The substantial aeolian erosion, indicated by up to ~15 cm ventifacts, likely precludes the use of varnish cover as a relative-age indicator in the study area. However, soil characteristics may be a useful parameter to consider in this geologic setting. One important outcome of these relative weathering parameters is that it illustrates the difference in resistance to weathering between these two rock types. Ignimbrite is more susceptible to weathering than andesite, as indicated by higher single mineral grain relief and larger pit depths.

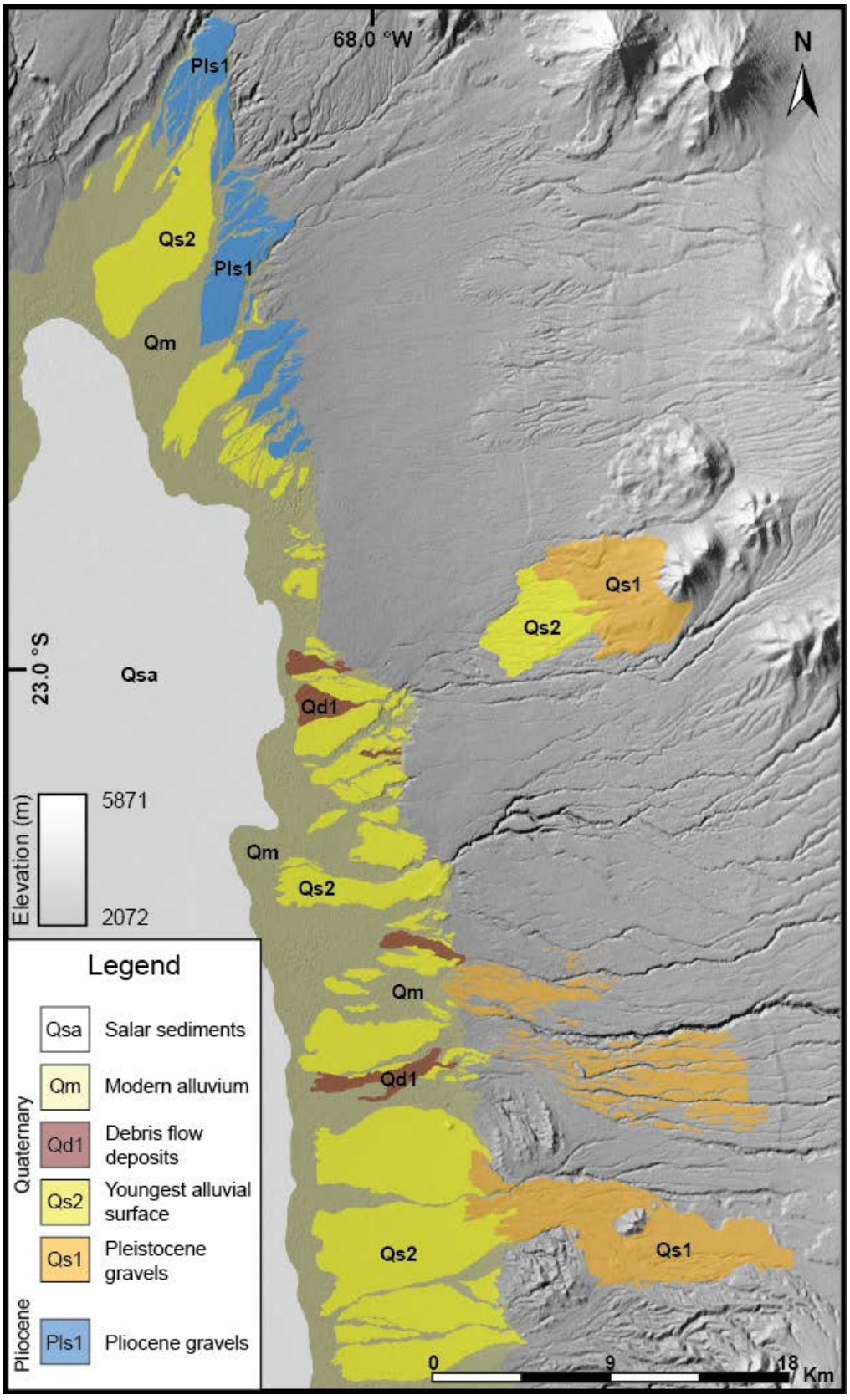

Figure 2-1: Geomorphic map of the study area showing general surficial geology.

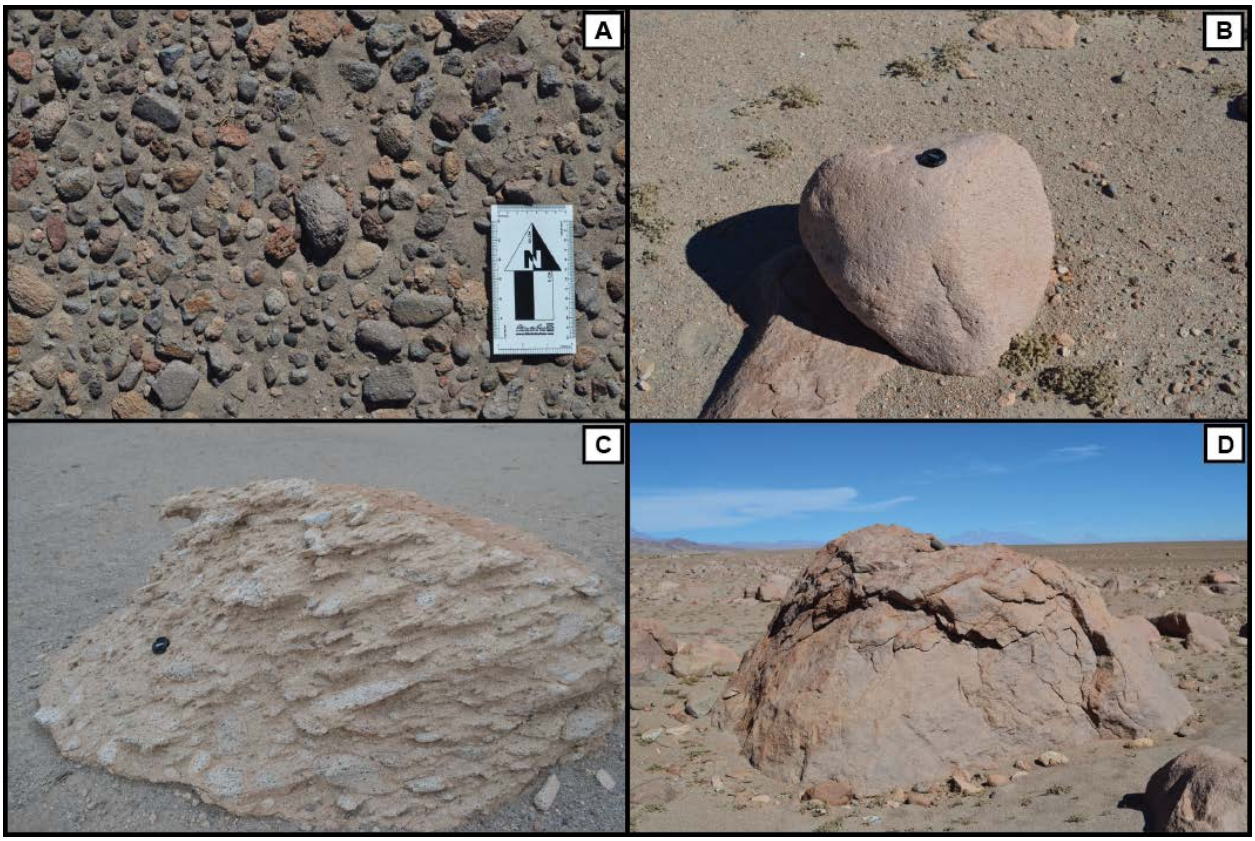

Figure 2-2: Examples of morphometric parameters from the study area. **A**. Typical alluvial fan surface cobbles. **B**. Pitted and rounded andesitic boulder. **C**. Ventifacted ignimbrite boulder. **D**. Fractured andesitic boulder.

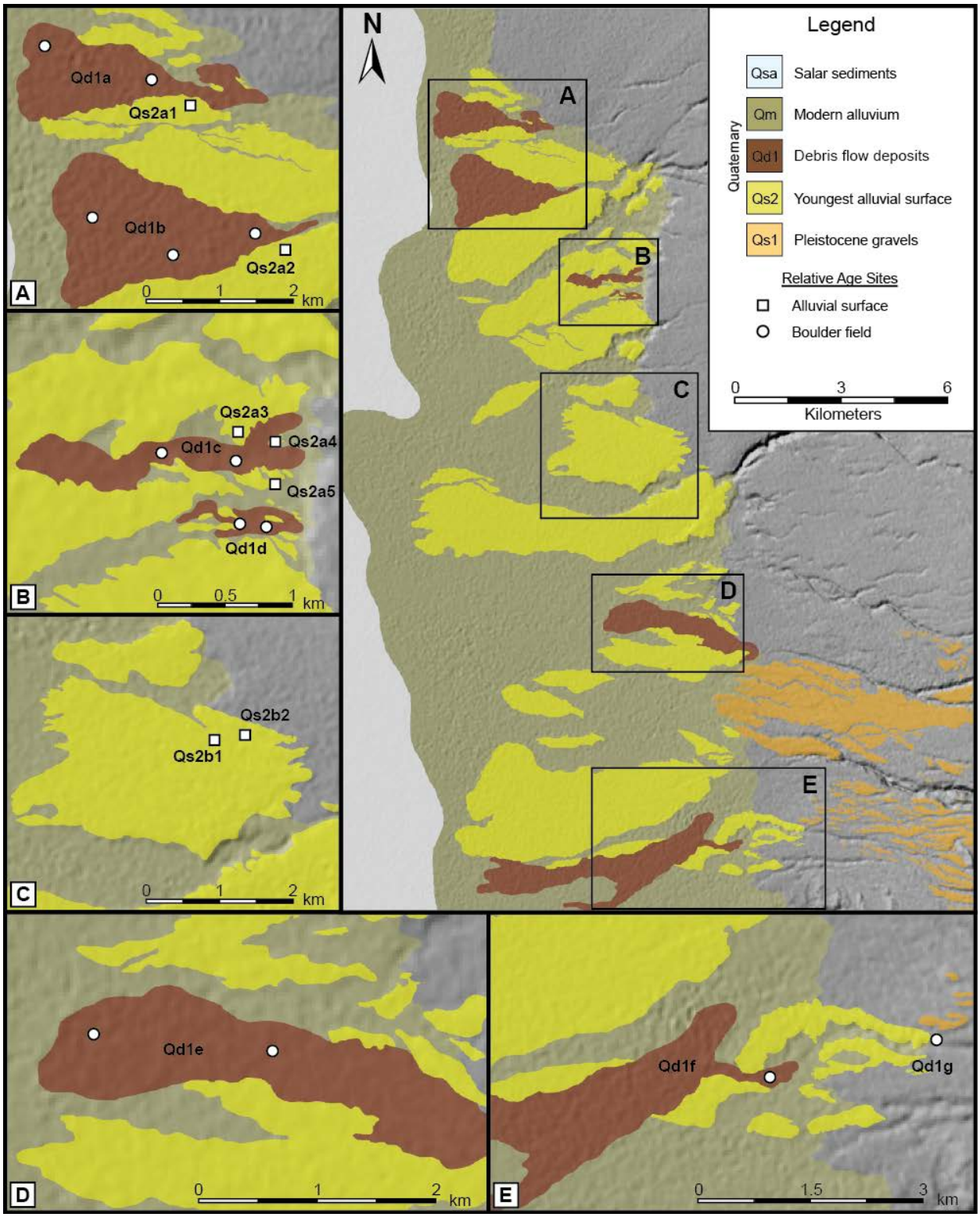

Figure 2-3: Locations of sampling sites for relative age parameters.

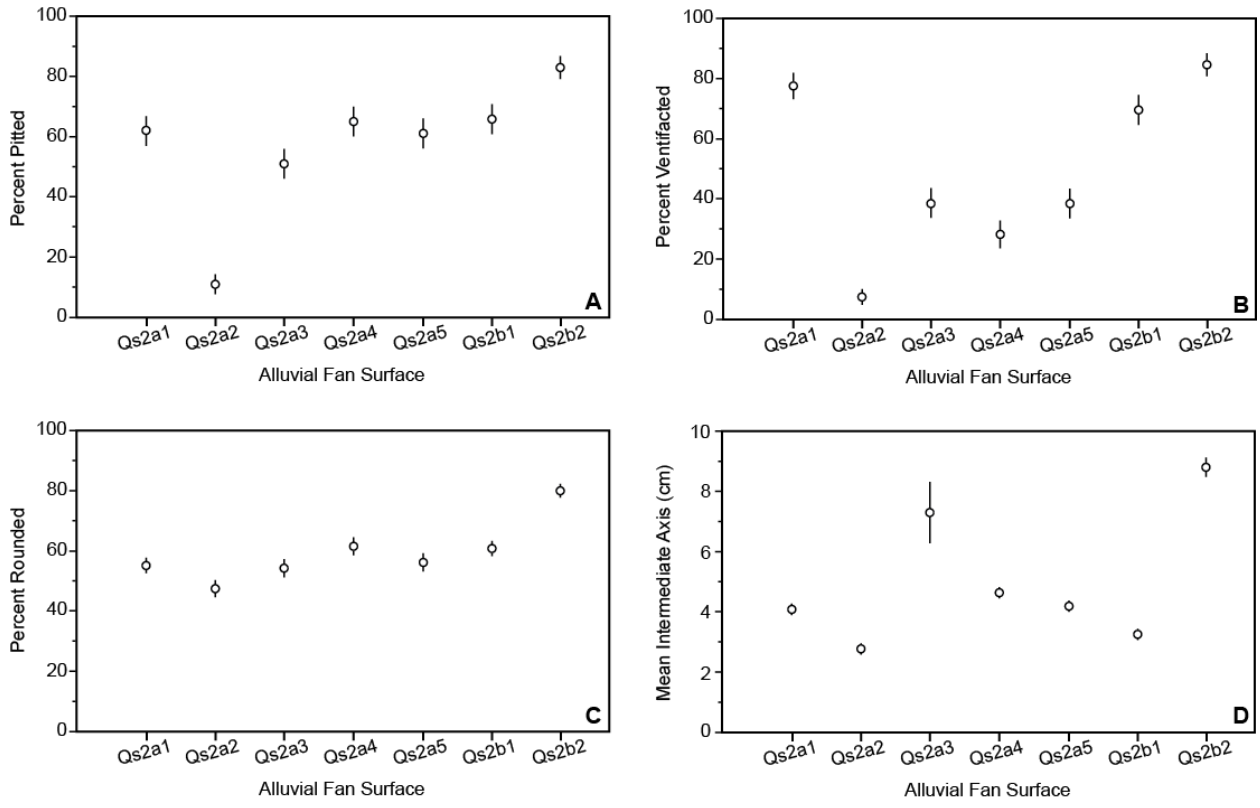

Figure 2-4: Measured morphometric parameters for alluvial fan surfaces. (A) Percent of cobbles that displayed pitting. (B) Percent of cobbles that displayed ventifaction. (C) Angularity of cobbles. (D) Intermediate axis lengths. Data compiled from 100 measured cobbles on each alluvial surface. Vertical error bars represent standard error, not shown when smaller than the point representing the value. Alluvial surfaces are arranged from oldest (left) to youngest (right) on x-axis on the basis of stratigraphic field relations.

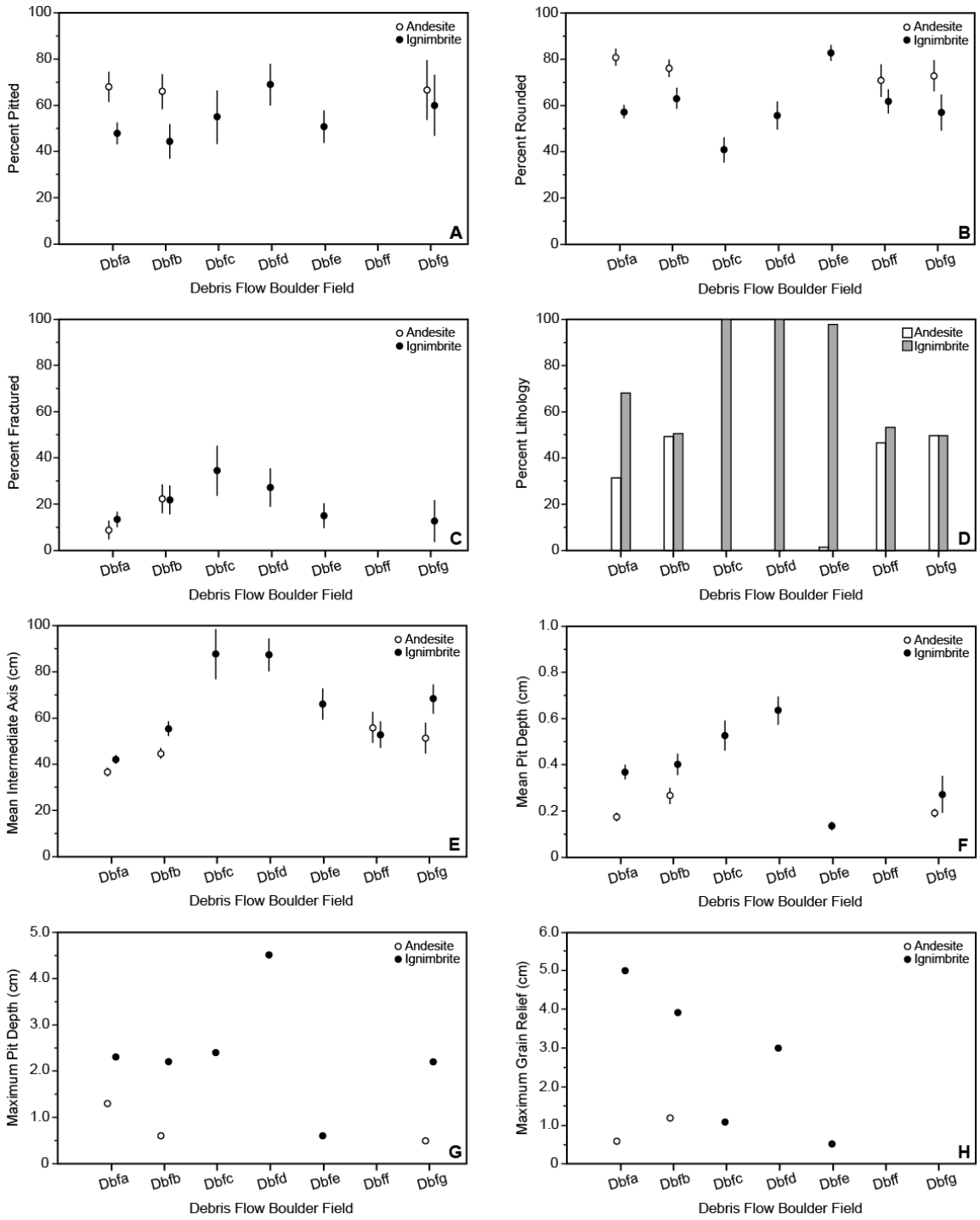

Figure 2-5: Measured morphometric parameters for debris flow boulder field deposits. (A) Percent of boulders that displayed pitting. (B) Angularity of boulders. (C) Percent of boulders that displayed fractures. (D) Boulder composition. (E) Boulder mean intermediate axis lengths. (F) Mean pit depth observed in each deposit. (G) Maximum pit depth observed in each deposit. (H) Maximum grain relief observed in each deposit. Vertical error bars represent standard error, not shown when smaller than the point representing the value. Debris flows are arrange from oldest (left) to youngest (right) on x-axis on the basis of stratigraphic field relations.

Table 2-1.

Relative-Age data for alluvial fan surfaces.

Relative Age Parameter[a]	Alluvial Fan Surfaces						
	Qs2a1	Qs2a2	Qs2a3	Qs2a4	Qs2a5	Qs2b1	Qs2b2
Pitted (%)	62 ± 5	11 ± 3	51 ± 5	65 ± 5	61 ± 5	66 ± 5	83 ± 4
Ventifacted (%)	77 ± 4	7 ± 3	38 ± 5	28 ± 5	38 ± 5	69 ± 5	84 ± 4
Rounded (%)	55 ± 3	48 ± 3	54 ± 3	62 ± 3	56 ± 3	61 ± 3	80 ± 2
Andesite (%)	94	100	89	92	98	100	98
Mean. Int. Axis (cm)	4.1 ± 0.16	2.8 ± 0.13	7.3 ± 1.01	4.6 ± 0.16	4.2 ± 0.13	3.3 ± 0.10	8.8 ± 0.32

Uncertainties expressed as Standard Error.

[a] Techniques for measurement of parameters and descriptions discussed in text.

Table 2-2.

Relative-Age data for debris flow boulder field deposits.

Relative Age Parameter[a]	Debris Flow Boulder Field Unit						
	Qd1a	Qd1b	Qd1c	Qd1d	Qd1e	Qd1f	Qd1g
Andesite							
Pitted (%)	68 ± 7	66 ± 7	-	-	0.0	ND	67 ± 13
Rounded (%)	81 ± 4	76 ± 4	-	-	0.0	71 ± 7	73.0 ± 7
Fractured (%)	9 ± 4	23 ± 6	-	-	100	ND	0
Lithology (%)	32	49	0.0	0.0	2	47	50
Mean Int. Axis (cm)	36.7 ± 1.1	44.4 ± 2.3	-	-	55.0	55.7 ± 6.5	51.1 ± 6.6
Mean Pit Depth (cm)	0.18 ± 0.02	0.27 ± 0.04	-	-	0.0	ND	0.20 ± 0.02
Max. Pit Depth (cm)	1.30	0.60	-	-	0.0	ND	0.50
Mean Grain Relief (cm)	0.19 ± 0.02	0.27 ± 0.05	-	-	0.0	ND	ND
Max. Grain Relief (cm)	0.60	1.20	-	-	0.0	ND	ND
Ignimbrite							
Pitted (%)	48 ± 5	44 ± 8	55 ± 11	69 ± 9	60 ± 7	ND	60 ± 13
Rounded (%)	58 ± 3	63 ± 5	41 ± 5	56 ± 6	83 ± 3	6 ± 5	57 ± 8
Fractured (%)	14 ± 3	22 ± 6	35 ± 11	28 ± 8	16 ± 5	ND	13 ± 9
Lithology (%)	68	51	100	100	98	53	50
Mean Int. Axis (cm)	41.9 ± 1.50	55.2 ± 3.19	87.4 ± 10.70	87.0 ± 6.92	65.9 ± 6.74	52.7 ± 5.73	68.1 ± 6.29
Mean Pit Depth (cm)	0.38 ± 0.03	0.41 ± 0.05	0.54 ± 0.06	0.64 ± 0.06	0.14 ± 0.02	ND	0.28 ± 0.08
Max. Pit Depth (cm)	2.30	2.20	2.40	4.50	0.60	ND	2.20
Mean Grain Relief (cm)	0.51 ± 0.03	0.49 ± 0.04	0.41 ± 0.09	0.85 ± 0.13	0.14 ± 0.03	ND	ND
Max. Grain Relief (cm)	5.00	3.90	1.10	3.00	0.50	ND	ND

Uncertainties expressed as Standard Error. ND: data on parameter not collected from particular deposit.

[a] Techniques for measurement of parameters and descriptions discussed in text

Chapter 3: Cosmogenic Surface Exposure Dating

3.1 Introduction

3.1.1 Terrestrial Cosmogenic Nuclides

The advent of terrestrial cosmogenic nuclide (TCN) surface exposure dating has significantly expanded the range of landforms suitable for establishing their ages and for quantifying rates of a variety of surface processes (Gosse and Phillips, 2001). Radiogenic nuclides are particularly suitable for landforms with projected ages greater than ~50 ka. The interaction of secondary cosmic-ray particles with minerals produces several *in situ* cosmogenic nuclides: ^{26}Al, ^{10}Be, ^{36}Cl, ^{3}He, and ^{21}Ne. The accumulation of cosmogenic nuclides within any given sample is a function of the duration of exposure, erosion, and the coupling of nuclide production and radioactive decay. In theory, measuring the concentration of cosmogenic nuclides along with a regional nuclide production rate in a given sample allows the exposure time at the Earth's surface to be determined. The production rate of cosmogenic nuclides is particularly sensitive to the local variation in the geomagnetic field, and must be scaled with the site-specific latitude and altitude (Lal, 1991; Dunai, 2000; Stone, 2000; Desilets and Zreda, 2003; Lifton et al, 2014).

Inheritance, or the cosmogenic nuclide inventory prior to the exposure in question, is a primary concern when dating exposure surfaces. An inherited signal accumulates as a consequence of one or more previous periods of exposure, and the cosmogenic nuclide inventory has not been reset by surface erosion or radioactive decay. In the case of alluvial fans, an inherited component may occur as a consequence of formative processes active on alluvial surfaces, i.e. reworking of surficial deposits or during initial erosion and transport of the sediment (Frankel et al., 2007; Machette et al., 2008; Owen et al., 2014). An inherited signal can be constrained by sampling along a depth-profile, where the nuclide concentrations from samples at sufficient depths isolate the inherited component from the *in situ* component (Anderson et al., 1996; Gosse and Phillips, 2001).

This study utilizes *in situ* cosmogenic chlorine-36 (^{36}Cl) as the targeted radionuclide to determine surface exposure ages for some of the mapped alluvial fans and debris flow deposits described in Chapter

2. *In situ* cosmogenic ^{36}Cl is produced through several mechanisms in rocks and sediments within the top two meters of the Earth's surface: spallation of ^{40}Ca, ^{39}K, Fe, and Ti; thermal and epithermal neutron capture by ^{35}Cl; and muon capture by ^{40}Ca and ^{39}K (Lal, 1991; Zreda et al., 1991; Gosse and Phillips, 2001; Schimmelpfennig et al., 2009; etc.).Cosmogenic ^{36}Cl is particularly advantageous in regions where the lithologies are not favorable to ^{10}Be exposure dating: e.g. carbonates and mafic volcanics. The volcanic landscape of the Chajnantor Plateau provides a variety of landforms and deposits suitable for ^{36}Cl surface exposure dating. ^{36}Cl can be measured in whole rock samples, as well as mineral separates, including calcite, plagioclase, and orthoclase (Zreda et al., 1991; Stone et al., 1995; Stone et al., 1997; Ivy-Ochs et al., 2007; Licciardi et al., 2008, Schimmelpfennig et al., 2009). TCN dating of an alluvial surface provides minimum ages on fan formation or the timing of surface abandonment (Owen et al., 2014).

3.1.2 Optically Stimulated Luminescence

Optically stimulated luminescence (OSL) is another dating technique that can contribute to our understanding of surface processes. In contrast to determining the timing of surface abandonment and exposure, OSL provides constraints on the timing of sediment deposition. This study utilized OSL dating to support cosmogenic surface exposure ages by determining depositional ages for sedimentary layers within the alluvial fan deposits. The dating technique is based on the measurement of trapped charges within the crystal lattice of buried mineral grains (Rhodes, 2011). Exposure to sunlight for a brief duration (1 to 100 seconds) is sufficient to reset the populations of traps within a crystal lattice, thus resetting the OSL burial clock. Upon burial and removal from sunlight, natural radiation results in the trapping of charges in structural defects in the crystal lattice of mineral grains. Populations of these traps gradually increase due to the natural radiation flux for the duration of burial. The trapped concentration of these charges can then be measured, and with a known environmental dose rate a depositional age for the deposit can be determined (Aitken, 1985; Huntley et al., 1985; Aitken, 1998; Rhodes et al., 2003; Rhodes, 2011).

Luminescence signals can be obtained through two measurement techniques: optically stimulated dating and thermoluminescence dating. In thermoluminescence (Aitken, 1985) the luminescence signal is obtained by heating mineral grains during measurement. In OSL (Huntley et al., 1985; Aitken, 1998) a light source, typically of blue or green wavelength, is used to remove the charges from light-sensitive traps. Quartz and feldspar are the targeted minerals utilized for measuring optical luminescence signals (Smith et al., 1986; Godfrey-Smith et al., 1988). Hütt and others (1988) determined the infrared stimulated luminescence (IRSL) of feldspar could also be utilized in determining depositional ages. This study utilized the OSL dating technique on quartz grains from sedimentary layers within the alluvial fan deposits.

3.2 Locations of Sampling Sites

Alluvial fan sampling sites were chosen on extensive fan surfaces that were interpreted to record a significant period of deposition and subsequent abandonment. Sites were located on broad, flat, elevated fan surfaces and were located away from eroding slopes and ephemeral surface channels. These sites were located on the highest elevation of the fan surface to avoid complications of topographic shielding and to minimize the potential for sediment shielding during the exposure history of the surface. Fan sampling sites were preferentially chosen on surfaces that were representative of the overall deposit and displayed minimal evidence for erosion, anthropogenic effects, or deflation or inflation of the surface. Six surface sites were chosen from across the study area: four from the regional Qs2 surface, one from the regional Qs1 surface, and one consisting of scattered gravels on the scoured ignimbrite shield. Twelve samples were collected from among these surfaces for *in situ* cosmogenic ^{36}Cl exposure dating (Fig. 3-1). An additional six samples were collected as part of a depth profile within one of the fan deposits in order to constrain inheritance and gain insight into depositional processes.

The exposure from which the depth profile was sampled is located in a gravel borrow pit outside the town of Toconao. This ~8 km section consists of medium- to coarse-grained massive gravel packages that are dominated by andesite lithologies, and that contain numerous minor lenses of fine sand (Fig. 3-2).

Slight imbrication is apparent among the gravels, suggesting deposition during sheet-flow events. Gravel packages are separated by two 0.2 to 0.3 m thick subparallel sand layers, though thickness varies along the exposure. The sand layers consist of fine to medium sand with erratic andesite clasts, and are observed on all exposure faces within the borrow pit, which suggests that they are laterally continuous. A characteristic sand layer occurs ~0.5 m below the surface, consisting of ample interspersed ignimbrite clasts. Where other exposures are present throughout the bajada, a similar gravel dominated sedimentology is observed.

Two OSL samples were collected, one from a suitable sand lens in the Toconao depth profile and another from Quaternary gravels perch on the upper elevations of the plateau. Three debris flow boulder fields were selected for sampling. Samples were taken from the uppermost surfaces of large 0.5 - 2 m, stable boulders that stood proud of the surface and showed little evidence of erosion. Separate debris flow deposits were identified by relatively distinct boundaries amid boulder trains, and samples were confined to these discrete deposits where possible. Eight boulders were sampled from among the three boulder fields for surface exposure dating.

3.3 Sampling Methodology

3.3.1 Cosmogenic Sampling Methods

Alluvial fan surface samples were each composed of 25 andesitic pebbles (~1.0 kg) with intermediate axes of ~ 3 cm. These 25 pebbles were amalgamated into a single sample for the surface to average out outliers of anomalously high or low inherited nuclide concentrations. The depth profile was sampled from the gravel pit near the town of Toconao that exposed a ~8 m section of alluvial fan deposits. Six samples were collected from several depths, determined by clast abundance, to a depth of 6 m. At each depth sampled, 25 andesitic pebbles were collected using the same criteria as surface samples. The surface of the gravel pit immediately surrounding the exposure was buried by tailings piles so determining whether the present surfaces is the original (top) depositional surface was unclear. To

determine whether the exposed fan surface represented the original surface, multiple exploratory pits were constructed along the same fan surface. A characteristic sand layer occurs ~0.5 m below the surface, containing abundant interspersed ignimbrite clasts. This unit was observed in all of the exploratory pits along the fan surface, suggesting the unit is laterally continuous. This same unit is exposed in the gravel pit at ~0.55 m, supporting the interpretation that the exposed surface does represent the original surface.

Debris flow samples consisted of ~1.0 kg of material removed from the uppermost horizontal surface of boulders. Material removed was typically ~3 cm thick or less. Outliers resulting from inheritance, erosion, or adjacent debris flow events were controlled for by sampling multiple boulders on discrete debris deposits. Boulders selected for sampling consisted of large 1- 2 m, stable boulders that stood proud of the surface and showed little evidence of erosion. Only boulders that displayed relatively horizontal surfaces, typically less than ~5° of inclination, were chosen. Sampling the tallest boulders minimized the probability that their upper surfaces had been shielded by sediment.

3.3.2 Optically Stimulated Luminescence Methods

OSL samples were collected where suitable sand packages were present. One was collected from a distinct sand layer at ~3.8 m in the depth profile at Toconao, and another was collected at ~2 m from an exposed sand package within a perched gravel deposit on the upper reaches of the plateau. Samples were collected by hammering 20 cm long, 5 cm diameter black PVC tubes into cleaned sediment faces. The tubes were driven horizontally into the surface until completely imbedded and flush with the sediment. Surrounding sediment was excavated and the tubes were extracted from the wall. Once removed, the open ends of the tubes were capped, sealed with duct tape, and placed in brown paper bags for transport. Care was taken to keep tubes horizontal throughout the process to minimize potential sediment mixing.

3.4 Cosmogenic ^{36}Cl Sample Preparation

^{36}Cl sample preparation in this study was performed to sequester the cosmogenic isotope ^{36}Cl from lithic material. Physical and chemical sample preparation, sample dissolution, chlorine extraction, and AMS-holder targeting were performed at the Cosmogenic Chlorine Laboratory of the Department of Geology at the University of Cincinnati and followed the procedures of Stone and others (1996). Procedures were slightly modified to accelerate the dissolution process (Radler, pers. comm.) and are outlined here.

3.4.1 Physical Preparation

Samples were pulverized in an electric jaw crusher to a size of 0.5 to 4 cm. The crushed sample was then fed through a disc mill pulverizer and sieved to 125 - 250μm until 250g of sample was obtained. All surfaces of the jaw crusher and pulverizer were cleaned with wire brushes and wiped with Kimwipes in between samples. Sieves were cleaned with compressed air to remove the majority of grains, followed by rigorous brushing with a wire brush to remove residual grains, and subsequently wiped with Kimwipes. Densities were determined on representative sample pieces of the original boulder or cobble, ~2 cm diameter, using Archimedes principle. Two representative ~10 g aliquots of the 125 – 250 μm sieved whole rock fraction were retained for bulk rock geochemistry, one prior to chemical preparation of the sample and one post-chemical preparation. Major and trace element compositions were analyzed by FUS-ICP and FUS-MS at Activation Laboratories Ltd in Ontario, Canada.

3.4.2 Chemical Preparation

Approximately 80 to 100g of the 125 – 250 μm sample fraction was used for the initial leaching phase of the procedure. Any remaining sample was saved and stored in Ziploc bags. All subsequent data was recorded on sample preparation bench sheets. Two chemical blanks and one direct precipitation blank were included with each processing round to control for reagent contamination.

Samples were transferred into Nalgene plastic bottles and leached overnight (12-16 hr.) in 70% 2.0 M HNO_3. The samples were then rinsed between five and seven times with 18 MΩ H_2O and dried overnight (12-16 hr.) in an oven at 85°C. The HNO_3 leach serves two purposes. First, any secondary carbonates and organics that may be present in the sample are dissolved and removed. Second, terrestrial and meteoric chlorine contamination on grain surfaces is removed. Multiple rinses with 18 MΩ H_2O ensure the removal of all HNO_3 and terrestrial and meteoric chlorine, as well as the removal of the fine fraction of material (<125 μm).

3.4.3 Dissolution and Carrier Spike

Once leached and dried, the samples were ready for dissolution and the addition of a ^{35}Cl carrier spike. Approximately 30 grams of leached sample was transferred into a clean, HNO_3 pre-leached 500 mL Nalgene container. The mass was measured to the nearest 0.0001 g and recorded on the bench sheet To each sample, approximately 1.0g of ^{35}Cl carrier spike was added (~1.0 mg of carrier). The mass was measured to the nearest 0.0001 g and recorded on the bench sheet along with the concentration of the spike solution. Two batches of carrier spike were used for sample preparation, with respective concentrations of 0.9817 mg/g and 1.033317 mg/g. The ^{35}Cl spike serves two purposes. The spike aids in diluting the $^{36}Cl/^{35}Cl$ ratio in samples that are presumed to have an old surface exposure age or those with lithologies or from locations conducive to significant cosmogenic ^{36}Cl production, reducing complications during AMS measurement. Conversely, in samples that are presumed to have a young surface exposure age or with lithologies or from locations that are not favorable to significant cosmogenic ^{36}Cl production, the spike aids in recovering the small quantities of ^{36}Cl present through isotopic equilibrium reactions.

Upon addition of the ^{35}Cl carrier spike, samples were prepared for dissolution. The samples were dissolved in a 40% low chloride, trace metal grade (TMG) HF/70% HNO_3 solution. An amount equivalent to five times the mass of the sample of 18 MΩ H_2O was added to the container. Subsequently, a mass equivalent to five times the mass of the sample of 40% low chloride, TMG HF was added to the container, followed by an amount equivalent to one and a half times the mass of the sample of 70% TMG

HNO_3. The samples were vigorously agitated to expose all grain surfaces to the HF/HNO_3 solution. The containers we loosely capped and allowed to vent for approximately one hour. Once venting ceased, the samples were agitated again, tightly capped, and placed on heated metal rollers at 60°C. The containers remained on the rollers until all sediment was completely dissolved, typically 48 to 120 hours.

Once samples had completely dissolved, they were removed from the rollers and allowed to return to room temperature. The solution was then transferred to 250 mL Nalgene containers and centrifuged at 2600 rpm for 30 minutes in an Allegra X-14 centrifuge, isolating any remaining undissolved solids and fluoride compounds from the supernate solution. This step also removes various oxides that may precipitate during dissolution, depending on the geochemistry and lithology of the samples. The supernate solution is transferred into a 500 mL Nalgene in preparation for preliminary AgCl precipitation.

3.4.4 AgCl Precipitation, Anion Exchange Chromatography, and Targeting

AgCl was precipitated through the addition of 20 drops of 0.15M HNO_3. Once added, the containers were agitated for approximately 10 seconds and then allowed to settle for 60 minutes. After they had settled, the sample containers were transferred to the refrigerator to induce the precipitation and accumulation overnight (12 – 16 hr.). The supernate solution was then decanted into an Ag/HF waste container, and the AgCl precipitate was collected and transferred into a 50 mL HNO_3 pre-leached centrifuge tube. The samples were centrifuged at 3600 rpm for 10 minutes to accumulate the AgCl in the bottom of the tubes. Minor fluoride compounds may still be present, and will amass alongside the AgCl. The samples were transferred to the refrigerator to await anion exchange chromatography.

Removal of interfering anions was accomplished through anion exchange chromatography, where each sample was passed through an anion exchange column. To prepare for the refinement of AgCl, the columns were conditioned through a series of steps. Conditioning the columns with acid of a specific molarity alters the charge of the substrate, which varies based on the pH of the resin, allowing for the

preferential removal of certain anions. Columns were conditioned by passing an 8 mL aliquot of 4.0M HNO_3 through the column. Once the solution had drained to the surface of the resin bed, the column was flushed with 20 mL of 18 MΩ H_2O.

Samples were dissolved with the addition of 20 drops of 30% NH_4OH and 5 mL of 18 MΩ H_2O. The centrifuge tubes were agitated for 20 seconds in a VWR Analog Vortex Mixer to fully dissolve the sample. Solid residues that remain are additional fluoride compounds that are in suspension. Samples that contained solid residue were centrifuged again, and the supernate solution and suspended AgCl was transferred to a new HNO_3 pre-leached centrifuge tube. The solids were stored until the final, refined AgCl was precipitated. $AgNO_3$ waste bottles were placed under the anion columns, and samples were transferred into the columns and allowed to drain to the surface of the resin bed. Respective column numbers for each sample were recorded on the bench sheets. Centrifuge tubes were rinsed with 10 mL of 0.1M NH_4OH, vortexed, centrifuged to isolate any re-suspended solids, and transferred to the columns. Once the solution had drained to the surface of the resin bed, 10 mL of 0.05M HNO_3 was eluted through the columns. Once drained, the column stopcocks were closed. AgNO3 waste containers were replaced with labeled, HNO_3 pre-leached 50 mL centrifuge tubes and 15 drops of 0.15M $AgNO_3$ solution was added. Chloride ions were eluted from the column through the addition of 20 mL of 0.15M HNO_3 solution. The elution of ions was successful when a white turbidity appeared in the centrifuge tube containing the $AgNO_3$ solution. Once the elution of chloride ions ceased and the solution was drained to the surface of the resin bed, 20 drops of TMG 70% HNO_3 was added to the centrifuge tube to facilitate the precipitate of the refined AgCl. Samples were agitated for 20 seconds, and then transferred to the refrigerator to allow for the precipitate to settle overnight (12 – 16 hr.).

Samples were removed from the refrigerator, vortexed for 20 seconds, and centrifuged at 3600 rpm for 10 minutes to facilitate the accumulation of an AgCl pellet The supernate liquid was decanted into an $AgNO_3$ waste container and 5 mL of 18 MΩ H_2O was added to the centrifuge tubes to rinse the AgCl pellets. The samples were vortexed for 10 seconds, centrifuged again for 10 minutes at 3600 rpm,

and the supernate was decanted. 1.5 mL microcentrifuge tubes were labeled, weighed to the nearest 0.0001 g, and triple rinsed with 18 MΩ H_2O. The weight of the tubes was recorded on the sample bench sheets. The AgCl pellets were dislodged and disaggregated with disposable pipettes, and then transferred to the microcentrifuge tubes. The samples were centrifuged at 3600 rpm for 10 minutes in a Microfuge 16 centrifuge to amalgamate the dispersed AgCl pellet A new disposable pipette was used to draw up and dispose of any remaining supernatant water. The samples were then placed in polycarbonate microcentrifuge holders and transferred to the oven. Samples were dried overnight (12-16 hr.) at 70° C in the drying oven. Once dried, the samples were allowed to return to room temperature and the weight of the AgCl and microcentrifuge tube was recorded on the bench sheet Each sample yielded approximately 3-5 mg of AgCl.

Samples are then loaded into copper target holders packed with AgBr for AMS measurement at the Purdue Rare Isotope Measurement (PRIME) Lab, Purdue University, Indiana. The copper target holders are pre-heated to approximately 60°C on a hot plate for 10 minutes. The pre-heating drives off any water that may be present in the AgBr matrix, in addition to making the AgBr malleable. Holder numbers for each sample are recorded onto the respective bench sheet, which are used to enter the sample batches into the online system at PRIME Lab. A 2-mm diameter stainless steel gauge pin is used to make a small depression into the center of the AgBr matrix. The sample pellet is transferred onto the matrix, and guided to the depression with the gauge pin. Once in the center, the AgCl pellet is packed into the AgBr matrix and the surface of the matrix is re-contoured with the gauge pin until relatively smooth. The white sample will turn dark grey or purple once it is sufficiently packed into the matrix. If more force is needed, gentle tapping with a ballpeen hammer can be used. A new pin gauge and placemat was used for each sample, and the workspace was thoroughly cleaned in between samples to minimize contamination. The packed copper holders are then returned to the hot plate and allowed to sit for 20 to 30 minutes at 60°C. This reheating drives off any moisture that accumulated during the packing of the sample. The samples are then placed into polycarbonate holders, capped, and stored until shipment to the Accelerator

Mass Spectrometry (AMS) facility at the Purdue Rare Isotope Measurement (PRIME) Lab for isotopic analysis.

3.5 Optically Stimulated Luminescence Sample Preparation

Optically stimulated luminescence (OSL) samples were processed under safelight conditions at the Luminescence Dating Laboratory in the Department of Geology at the University of Cincinnati. Tubes remained sealed until the time of processing. A 3 cm-thick layer of sediment was removed from each end of the tube to obtain sediment from the center of the tube for processing and to reduce the possibility of exposure to daylight selecting sediment to be analyzed. Approximately 10 g of the dried sub-sample from the sediment sample was ground to a fine powder with SPEX SamplePrep 8000 Mixer/Mill and shipped to Activation Laboratories Limited in Ancaster, Ontario, Canada for Major Elements Fusion ICP/MS/Trace Elements analysis. Using dose-rate conversion factors of Adamiec and Aitken (1998) and β-attenuation factors of Mejdahl (1979) and Adamiec and Aitken (1998), the elemental concentrations were converted into external β and ɣ components, which were attenuated for moisture content. These were summed together with a cosmic ray component using the methods of Prescott and Hutton (1994) to give estimates of the total dose-rate (DR) for each sample.

3.5.1 Physical and Chemical Preparation

The sediment from the center of the tubes was pretreated with 10% HCl and 10% H_2O_2 to remove carbonates and organic matter, respectively. The pretreated samples were rinsed in water, dried, and sieved to collect the 90-250 μm particle size fraction. This fraction was etched using 44% HF acid for 70 minutes to remove the outer, α-irradiated layer from quartz particles in addition to feldspar removal. Any subsequent fluoride precipitates were removed using concentrated HCl. The quartz sample was rinsed in distilled water and acetate, then dried and sieved to obtain a grain size fraction of 90-150 μm in diameter. A low field controlled Frantz isodynamic magnetic separator (LFC Model-2) was used to separate feldspar and magnetic minerals from quartz in the 90-150 μm particle size fraction (Porat, 2006). Forward

and side slopes were set at 10° and 15°, respectively. To obtain clean quartz aliquots, each sample was subjected to three magnetic separations with variable magnetic field intensities.

3.5.2 Luminescence Measurements

Luminescence measurements were undertaken on the 90-150 μm quartz fraction for each sample using a Riso Automated TL/IRSL/Blue DA-20 C/D OSL Dating System. Aliquots, containing approximately one hundred grains of the samples, were mounted as a small central circle ~ 2 mm in diameter onto ~ 9.7 mm diameter stainless steel discs. Aliquots for each sample were first checked for feldspar contamination by means of IRSL at room temperature using infrared stimulation with infrared light emitting diodes (870 nm, 150 mW/cm^2) before the main OSL measurements were undertaken (Jain and Singhvi, 2001). If the aliquots did not pass the IRSL test the samples were etched in 44% HF for an additional 30 minutes to remove any feldspar, followed by a concentrated HCl treatment and sieving again. Samples that passed the IRSL test were used for OSL dating. Aliquots of samples were illuminated with blue LEDs stimulating at a wavelength of 470 nm (blue light stimulated luminescence – BLSL). All OSL signals were detected using a 52 mm diameter EMI 9235 QA photomultiplier tube. Riso Sequence Editor Software was used for hardware control. The detection optics comprised Hoya U-340 and Schott BG-39 color glass filters coupled to photomultiplier tube. The samples were irradiated using a $^{90}Sr/^{90}Y$ β-source.

D_E measurements were determined on multiple aliquots for each sample using the single aliquot regenerative (SAR) method protocol developed by Murray and Wintle (2000) and Jain et al. (2008). In the SAR method, each natural or regenerated OSL signal is corrected for changes in sensitivity using the OSL response to a subsequent test dose. The natural dose (N) was measured in the first cycle, and thereafter five regeneration doses (R1 to R5) were administered. The first two were used to bracket the natural luminescence level (R1 < N ~ R2 < R3). The fourth (R4) was set at zero to monitor recuperation (i.e., R4/N). The fifth dose was made to monitor the reproducibility of sensitivity corrections, where a dose

equal to the first dose was applied (i.e., R1/R5) defined as the recycling ratio. Each measurement cycle comprised a regeneration dose (zero for natural), preheating of 240°C for 10 s, optical stimulation for 100 s (at a sample temperature of 125°C), a constant test-dose, a test-preheat of 160°C for 0 s and a final optical stimulation for 100 s (at 125°C). The net-natural and net-regenerated OSL were derived by taking the initial OSL signal (0-1 s) and subtracting a background from the latter part of the stimulation curve (90-100 s); subtracting the background from the preceding natural and regenerative OSL signals derived the net test-dose response. Growth curves were plotted using the net natural and regenerated data divided by the subsequent response to the net-test dose (Murray and Wintle, 2000). Growth curves were generated by fitting a saturated exponential function. Contamination of quartz by feldspar was checked for each aliquot by applying an infrared light stimulation (IRSL). Any sample that produced a luminescence signal when stimulated by IRSL was not included in the analysis. A preheat of 240 °C for 10s was used and the OSL signal was recorded for 100 s at 125 °C.

3.6 Accelerator Mass Spectrometry Results

TCN samples were analyzed by Accelerator Mass Spectrometry (AMS) at the PRIME Lab. Twenty-six targets were analyzed, in addition to ten process blanks and four direct precipitation blanks, two for each respective carrier solution. One sample yielded negative $^{36}Cl/^{35}Cl$ values, and as such was removed from subsequent age calculations. These negative values are attributed to AMS error or insufficient removal of ^{36}Cl during Anion Exchange Chromatography. $^{36}Cl/^{35}Cl$ values for seven process blanks ranged from 2.28 to 6.20 x 10^{-15} suggesting negligible reagent contamination. Two process blanks had respective values of 24.98 x 10^{-15} and 30.36 x 10^{-15}, both of which suggested negligible reagent contamination. The tenth process blank displayed a considerably elevated $^{36}Cl/^{35}Cl$ value of 144.14 x 10^{-15}, indicating potential contamination. However, because the duplicate process blank for that batch presented an acceptable value (6.13 x 10^{-15}), contamination of the blank was attributed to an external source. Raw AMS results are included in Appendix B.

3.7 TCN and OSL Analysis and Age Calculations

3.7.1 ^{36}Cl Production Systematics

In situ cosmogenic ^{36}Cl is produced through three pathways in rocks and sediments within the top few meters of the Earth's surface (Fig. 3-3). High energy neutron spallation of ^{40}Ca, ^{39}K, Fe, and Ti is the dominant mechanism of production within the top ~1 meter of the surface. This spallogenic production falls of exponentially with depth, and is outpaced by thermal and epithermal neutron capture by ^{35}Cl. Interaction with muons, particularly muon capture by ^{40}Ca and ^{39}K, dominates production at depths below ~3 m. (Lal, 1991; Zreda et al., 1991; Gosse and Phillips, 2001). The concentration of cosmogenic nuclides within the top few meters of the earth's surface can be represented by (Anderson et al., 1996; Jungers et al., 2013):

$$N(z,t) = N_0 e^{-\lambda t} + \frac{P_0 e^{(-\rho z)/\Lambda}}{\lambda + \rho\varepsilon/\Lambda}\left(1 - e^{-\left(\lambda + \left(\rho\varepsilon/\Lambda\right)\right)t}\right)$$

where N, the concentration of cosmogenic nuclides [atoms g^{-1}], is a function of; t, the time [yr], N_0, the inherited concentration of the cosmogenic nuclide [atoms g^{-1}], λ, the decay constant for the cosmogenic nuclide [yr^{-1}], ε, the erosion rate [cm yr^{-1}], P_0, the production rate of the cosmogenic nuclide at the surface [atom g^{-1} yr^{-1}], Λ, the attenuation length of nuclide production [g cm $^{-2}$], ρ, the density of sediment [g cm $^{-3}$], and z, the depth below the surface [cm].

3.7.2 Uncertainties

One of the major sources of error in TCN exposure dating techniques is the rate of cosmogenic nuclide production. ^{36}Cl production rates are constrained by calibration against deposits with independent age constraint (Zreda et al., 1991; Phillips et al., 1996; Stone et al., 1996; Licciardi et al., 2008; Schimmelpfennig et al., 2011; Merchel et al., 2013). Variation in the geomagnetic field intensity, primary radiation flux, and atmospheric density causes the production rate at any given location to fluctuate

(Dunai, 2000; Stone, 2000). Variations in these parameters and the production rate of ^{36}Cl over geologic timescales introduce added complexity.

Additional error is introduced by uncertainties in the local production rate related to shielding by topography, vegetation, snow cover or sediment; rates of postdepositional weathering and erosion; and target material density. These factors generally reduce the concentration of nuclides, thus resulting in an underestimate of the true age. In contrast, previous periods of exposure increase the concentration of nuclides in a sample, resulting in an overestimation of the true exposure age. Additionally, the uneven distribution of geologic processes such as weathering, erosion, and non-uniform local exhumation of boulders, for example, have the potential to result in a large spread of exposure ages on a given surface or landform.

The degree of terrain shielding was determined by using an inclinometer to calculate the inclination of surrounding topography relative to the surface of interest. The inclination of the surrounding topography was below 8° for all sampling locations, which indicated that terrain shielding is not a significant factor in the study area, and is not expected to have varied significantly over the late Pleistocene. Indeed, terrain shielding correction factors were negligible at all sites, and are an order of magnitude below AMS error. As such, only corrections for self-shielding were applied where measured. Sediment shielding is a concern for sampled alluvial fan surfaces, as small dune fields are observed on the local scale along the base of the plateau. Samples were collected from the highest elevation on the fan surface to minimize the likelihood that the surface had been previously buried. Density of the rocks was measured on a representative fraction of each sample and variations within respective lithologies were negligible. Geologic uncertainties are commonly assessed by collecting and analyzing multiple samples on a given surface to examine the spread of ages. In the case of this study, geologic uncertainties are "averaged out" by the amalgamation of multiple surface cobbles into a particular sample. Thus, samples with anomalously high or low nuclide concentrations are buffered by the remaining cobbles. In addition,

multiple samples were collected from certain surfaces to assess the reproducibility of exposure ages. This sampling approach assumes that the reworked clasts are sourced from the same deposit.

3.7.3 Age Calculation

Surface exposure ages were calculated with the Age Calculation Engine (ACE) of Zweck and others (2012; http://ace.hwr.arizona.edu) using a time-varying production rate scaling scheme based on latitude-altitude-pressure factors of Stone (2000). Additional components included the sea level curve of Fairbanks (1989) and Shackleton (2000), the paleolatitude record of Ohno and Hamano (1992) and Yang and others (2000), and the geomagnetic intensity model of Guyodo and Valet (1999). The modeled ages were calculated using ^{36}Cl production rates of 67.57 ± 3.08 at/g Ca/yr (calcium spallation), 158.37 ± 8.42 at/g K/yr (potassium spallation), and 638.59 ± 39.93 at/g/yr (low-energy neutron capture) after Phillips and others (1996). These factors are shown locally to yield ages that are consistent with other, independent cosmogenic measurements (Ward et al., in review).

For optically stimulated luminescence samples, the equivalent dose (D_E) value for each aliquot was examined using the Riso Analyst 3.22b software. Aliquots that displayed poor recuperation (>10%) were not included in age calculations. The D_E of all eligible aliquots were used to determine a weighted mean D_E, which was then divided by the calculated dose rate to determine the weighted mean age for the sample. See Appendix C for individual aliquots.

3.8 Surface Exposure and Depositional Ages

3.8.1 TCN Exposure Ages

Exposure ages on alluvial fan and gravel deposits range from 20.7 ± 1.41 ka to 419.3 ± 39.7 ka and are summarized in Table 3-2 and Figure 3-4. Where multiple samples were collected from the same surface, calculated ages are reasonably consistent. Gravels on the ignimbrite shield from the Qs1 surface display two ages that cluster around ~21 ka and an older one at ~419 ka. Ages on alluvial surfaces from

the Qs2 surface range from 23.4 ± 1.6 ka to 145.1 ± 9.7 ka, with populations around ~33 ka and ~55 ka and a single age at 145 ka. Ages on debris flow boulders from the Qd1 surface range from 9.3 ± 1.1 ka to 202.6 ± 19.7 ka. A population of ages clusters between ~9 ka and ~26 ka, while two outliers at 118.7 ± 21.6 ka and 202.6 ± 19.7 ka are also observed (Table 3-1, 3-2; Fig. 3-4).

Probability density functions (PDFs) (or "camel plots") were constructed for ages calculated on alluvial fan surfaces and debris flow boulders. PDFs describe the frequency of values observed among a data set and PDFs analyze a set of values with Gaussian uncertainties to generate an error-weighted mean for the data (Lowell, 1995). Each individual measurement is assigned a Gaussian with a mean and standard deviation, which are then added to formulate the summary curve.

3.8.2 OSL Ages

The luminescence characteristics for the two samples were typical for quartz derived from volcanic lithologies (Fig. 3-5). However, the slow decay observed in the shine down curves is also typical of feldspar. As such, the samples were checked for IRSL to determine if feldspar was present in the samples. The IRSL values were near background values, indicating the absence of feldspar grains in the sample. Growth curves indicate that the samples are not saturated. A spread among D_E values for all aliquots is observed, which typically indicates a potential mixing of sediment. Nevertheless, the calculated ages are generally in good agreement with geologic, stratigraphic, and geomorphic context (Table 3-3, 3-4).

Sample Toc-Osl1, collected from a sand layer at a depth of 3.8 m in the TCN depth profile, returns an age of 42.86 ± 2.03 ka. This is geologically reasonable, and in good stratigraphic agreement with the corresponding ^{36}Cl exposure ages for the alluvial surface (30.35 ± 2.26 and 35.69 ± 2.17). Sample Chaj-Osl1, collected at a depth of 2 m in an exposed sand package within a gravel deposit perched on the ignimbrite shield, returns an age of 40.51 ± 2.00 ka. The age appears geologically

reasonable; however the age cannot be corroborated by TCN exposure dating because surface cobbles were not collected from the deposit.

3.9 TCN Depth Profile Considerations

As noted above, the cosmogenic inheritance is one of the major complications concerning TCN exposure dating of alluvial surfaces. The additional nuclide signal from these previous periods of exposure results in an overestimation of the true age. Inheritance is particularly an issue with younger alluvial surfaces, as well as units that are composed of reworked sediment from older deposits (Owen et al., 2011; Blisniuk et al., 2012). Previous studies have assessed the nuclide inheritance of sediment (Anderson et al., 1996; Hancock et al., 1999; Jungers et al., 2013), surficial erosion (Hidy et al., 2010), and complexity of depositional history (Matmon et al., 2006; Jungers et al., 2013) through the use of TCN depth profiles. Below a certain depth, typically ~2 m, the cosmogenic nuclide concentration of sediment is recognized as the inherited component derived from previous periods of exposure (Fig. 3-5). Once constrained, this component can then be removed from the total nuclide concentration to calculate a corrected exposure age.

Cosmogenic ^{36}Cl concentrations of the depth profile are geologically reasonable and significantly decrease with depth in the deposit as projected (Fig. 3-7, Table 3-2). Apparent inheritance is minimal, approximately 1.5 x 10^5 atoms g^{-1}, an order of magnitude below total ^{36}Cl concentrations observed in surface samples. As such, ^{36}Cl inherited concentrations can generally be disregarded as they are within the standard error of the calculated ages. The characteristic "hump" in increased TCN concentration at ~ 0.2 m below the surface was not captured in the depth profile, resulting in the concentrations emulating an exponential decay function (Fig. 3-7). Despite this, the concentrations suggest the alluvial surface is relatively stable and has not been subject to significant erosion. The concentration profile generated implies a relatively rapid erosion of upland gravels and subsequent deposition, consistent with the interpretations of Jungers and others (2013) for fan complexes within the Central Depression. Thus, while

the gravels are likely sourced from older perched deposits on the upper plateau, relatively rapid transport and deposition minimizes their inherited ^{36}Cl nuclide signal.

Cosmogenic nuclide decay is an appropriate concern when dealing with depth profiles within mature deposits, particularly when utilizing ^{36}Cl due to its relatively short half-life (308.0 ka ± 3.0 ka) in contrast to ^{10}Be (1.387 Ma ± 0.012 Ma), for example (Gosse and Phillips, 2001; Korschinek et al, 2010). The ACE calculator accounts for the effect of this cosmogenic nuclide decay when determining exposure ages.

Surface erosion can also influence the nuclide concentration of a sample. Erosion removes material from the sample, resulting in a reduced nuclide concentration and thus an underestimated exposure age. Previous studies have shown that erosion rates in the central Atacama are exceptionally slow, ranging from 0.2 to 0.4 m/Ma, comparable to those of other deserts (Placzek et al., 2010). Placzek and others (2014) observed erosion rates of ~1 m/Ma on the flanks of the Andean Cordillera. These slow rates suggest that erosion is not a dominant geologic factor influencing the surface exposure ages in this study.

3.10 Synthesis

Cosmogenic ^{36}Cl exposure dating yields ages for alluvial surfaces and debris flow deposits along the western margin of the Chajnantor Plateau. Generally, the exposure ages should be considered a minimum due to the possibility of surface erosion. Cosmogenic inheritance does not appear to significantly influence the surface exposure ages on the alluvial surfaces. The amount of nuclide inheritance is constrained by the concentration-depth profile, and appears to be negligible. Inheritance may vary between deposits as a consequence of variation in source material, particularly when comparing fan clasts that were eroded from bedrock compared to clasts that were redeposited from older fans. In the case of the alluvial fans sampled and dated, the fans appear to be sourced exclusively from reworked material. While the concentration-depth profile allows for the cosmogenic inheritance to be determined

within one of the alluvial fans, it does not elucidate inherited nuclide signals that may be present in individual debris flow boulders. Bierman and others (2014) observed relatively large variation in nuclide inheritance among boulders deposited in a modern debris flow in Brazil, which suggests the boulders resided for a period of time on stable surfaces or in the shallow subsurface before being transported. We argue that the inheritance issue may be reduced here by several factors. The debris flow boulders may have first formed in fracture-controlled bedrock channels from bedrock erosion, or if produced farther upslope on the shield, were transported and stored in these bedrock channels where they were shielded. The relatively tight clustering of exposure ages and geologic and geomorphic observations suggest that cosmogenic inheritance is minimal for the majority of boulders. While variable, the lithology of boulders among debris flow deposits has a substantial ignimbrite component. Ignimbrite is a poorly resistant lithology, as shown by the prevalence of ~10-15 cm ventifacts. Because ignimbrite is weak, there is a greater likelihood that surfaces of prior exposure were eroded during transport, thus resetting or greatly minimizing the inherited nuclide signal. The ignimbrite boulders may be generated in the fracture controlled bedrock channels, and entrained within these channels until mobilized by a sufficiently large precipitation event.

Interpretation of surface exposure ages requires an understanding of the influence erosion and inheritance exert on the nuclide concentration. Constraining these controls on the nuclide inventory provides confidence that the ages calculated accurately represent the exposure age of the surface. Coupled with geomorphic observations, these exposure ages provide the context for a detailed interpretation of the Chajnantor alluvial system and associated debris flow deposits.

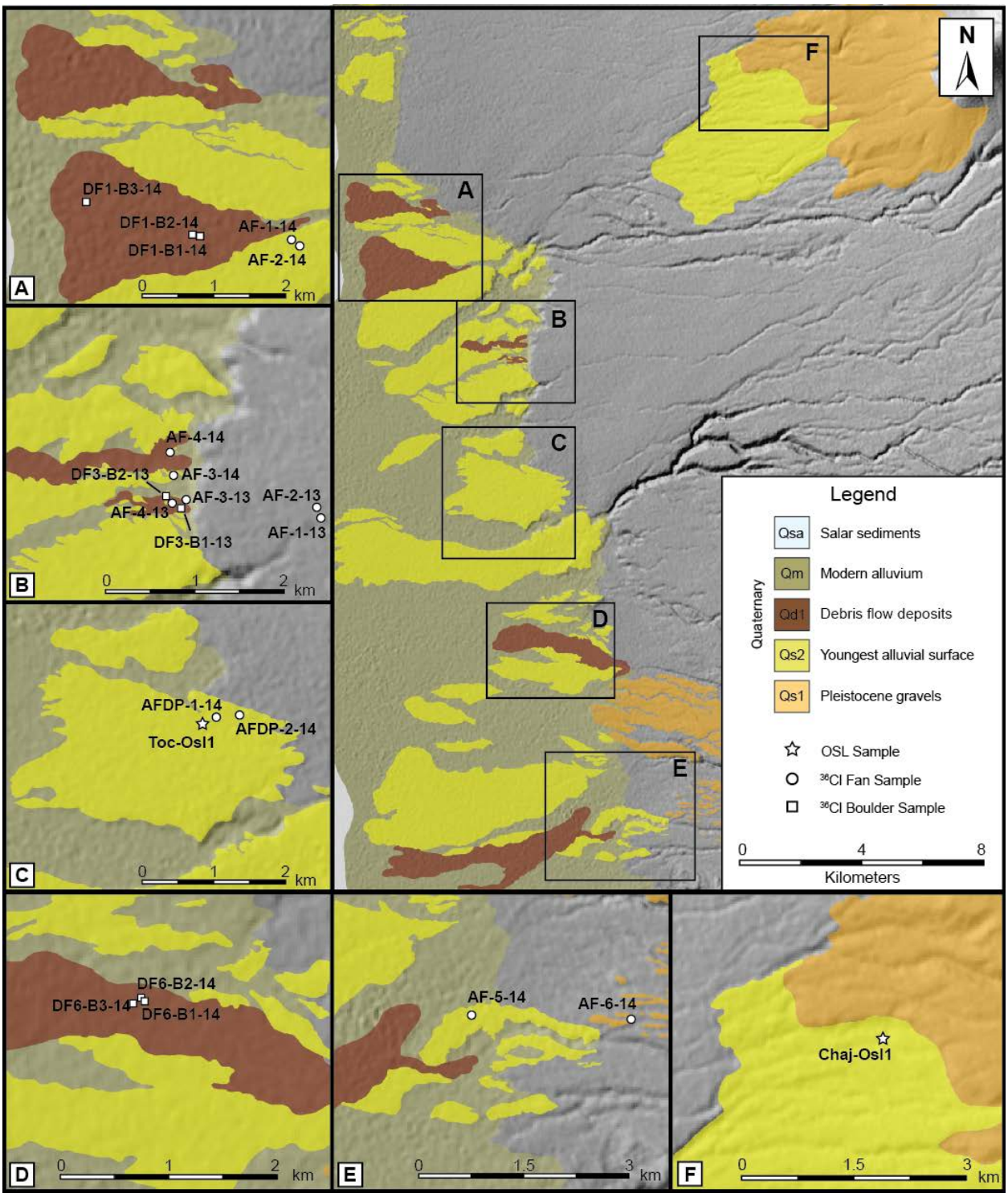

Figure 3-1: Location of TCN and OSL samples.

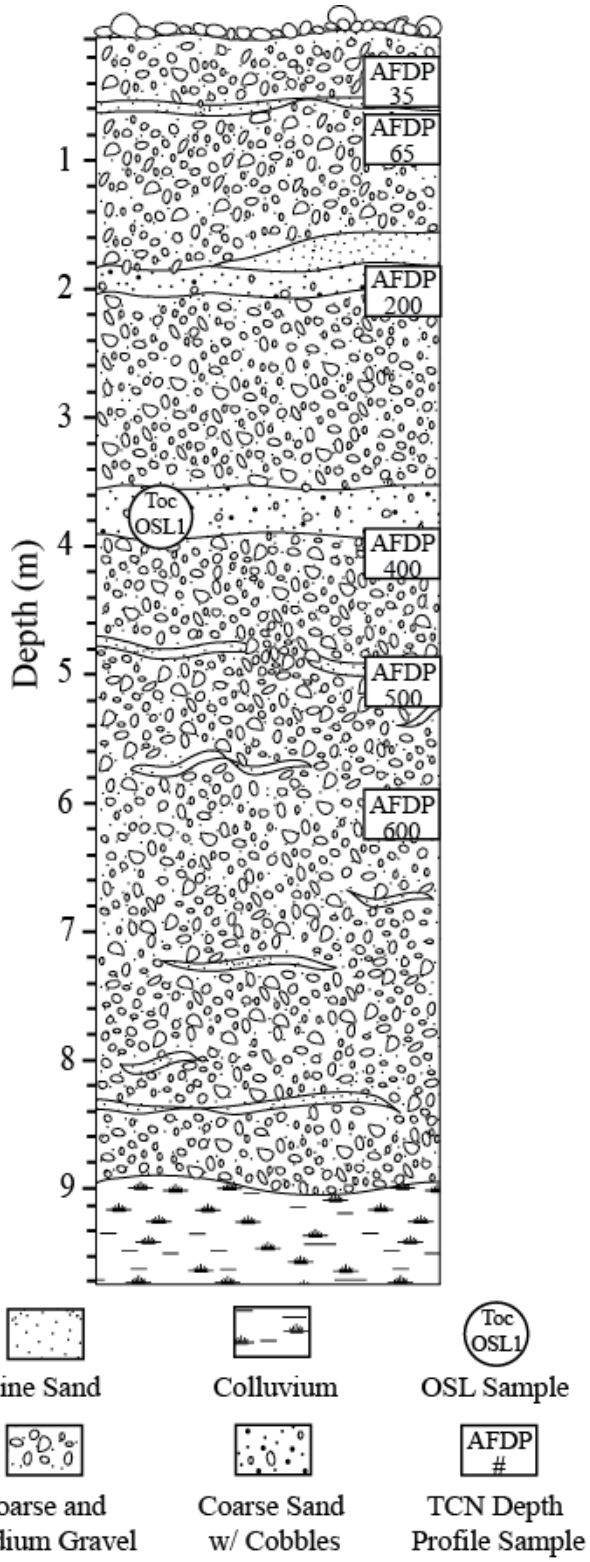

Figure 3-2: Depth profile sketch of the Toconao gravel pit exposure.

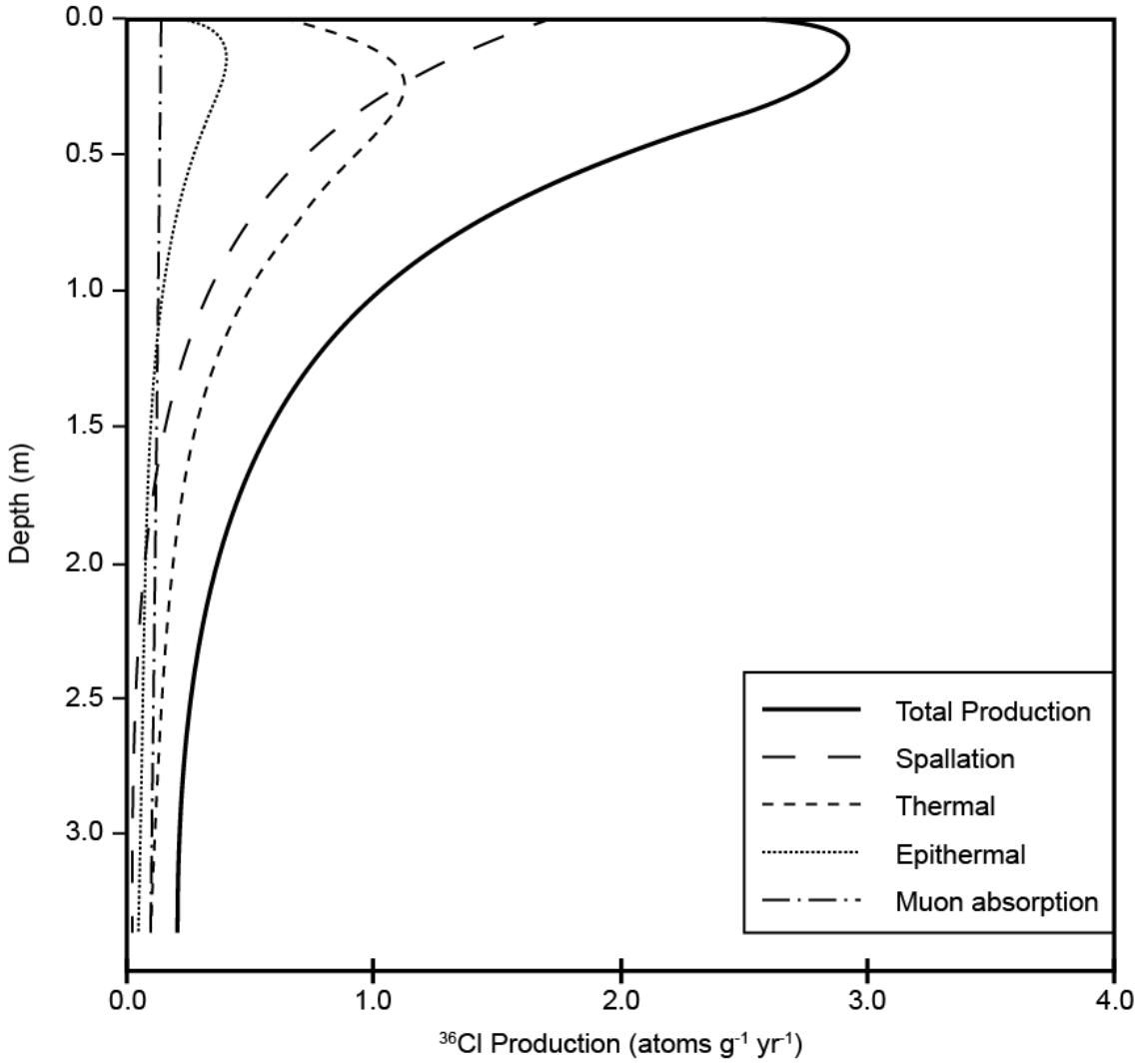

Figure 3-3: Production of ^{36}Cl with depth at high latitude and sea level. Modified from Gosse and Phillips (2001).

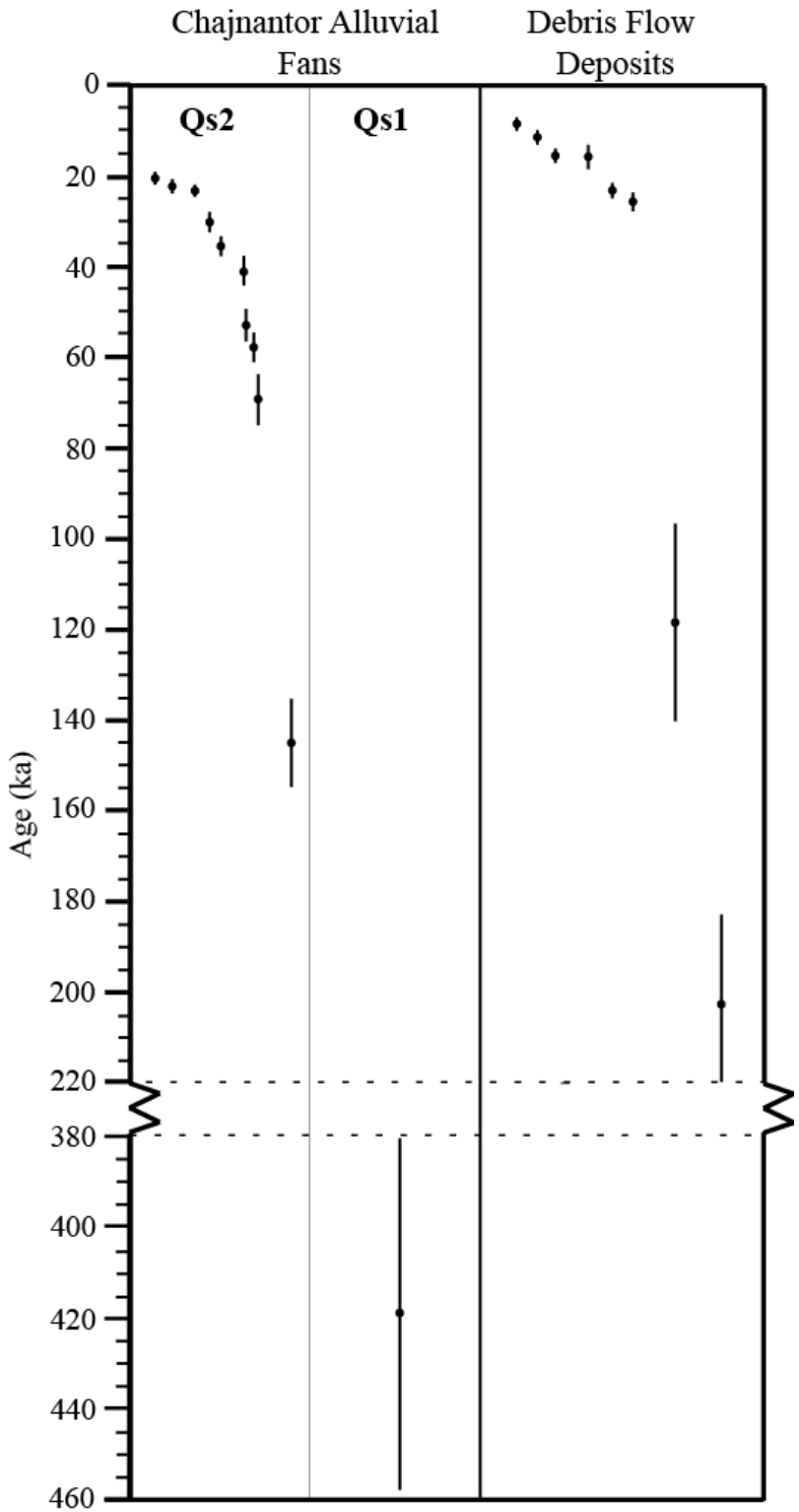

Figure 3-4: Distribution of ^{36}Cl exposure ages for alluvial fan surfaces, plateau gravels, and debris flow deposits. Error bars represent standard error.

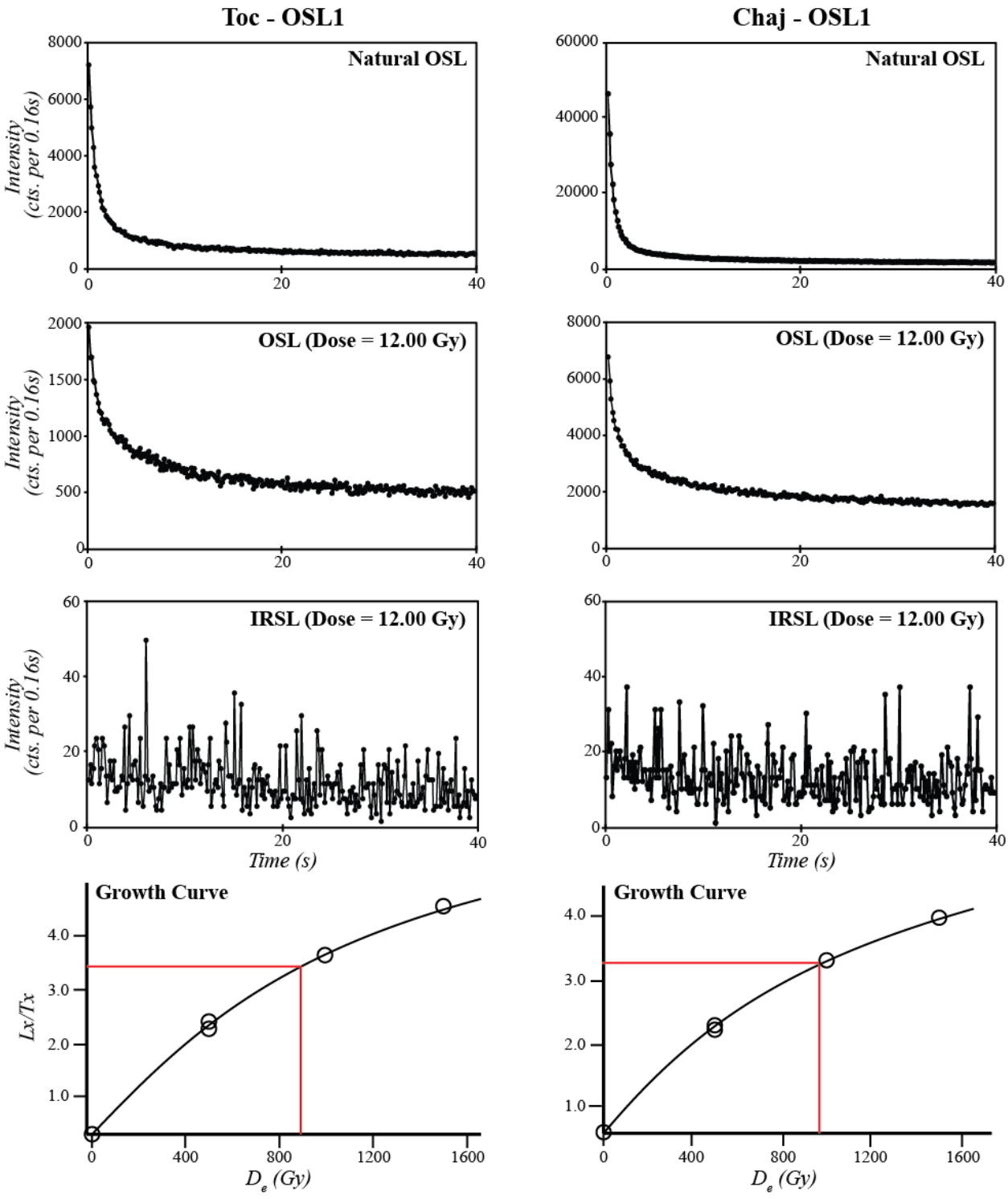

Figure 3-5: Optically stimulated luminescence curves. Top to Bottom: shinedown curve, regenerative curve, IRSL signal, and growth curve.

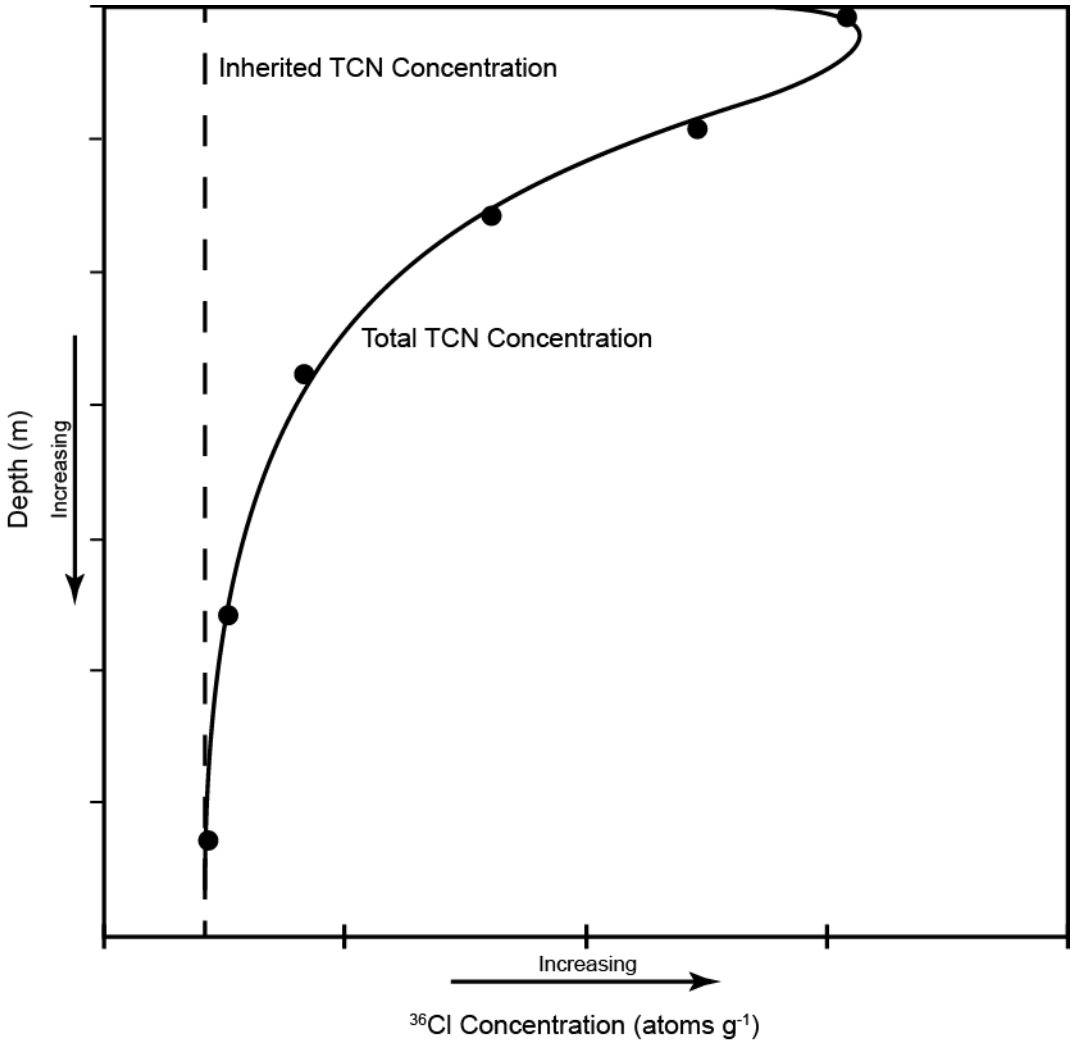

Figure 3-6: Theoretical ^{36}Cl concentration-depth profile. Cosmogenic inheritance constrained by the position of the curve at depth.

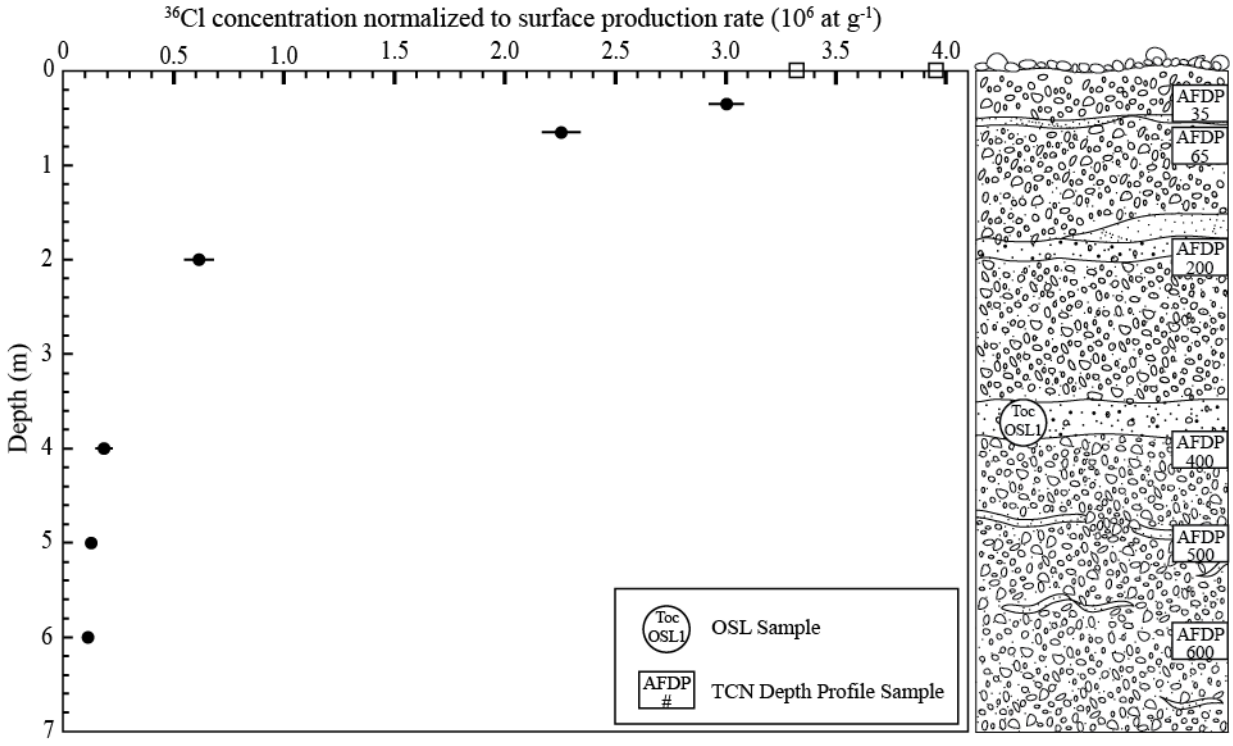

Figure 3-7: ^{36}Cl depth profile for Chajnantor fan complex with corresponding profile sketch, see text for context and description. ^{36}Cl concentrations decay rapidly with depth.

Table 3-1.
Major and trace element concentrations for alluvial fan and debris flow samples.

Sample No.	SiO_2 (wt.%)	TiO_2 (wt.%)	Al_2O (wt.%)	Fe_2O_3 (wt.%)	MnO (wt.%)	MgO (wt.%)	CaO (wt.%)	Na_2O (wt.%)	K_2O (wt.%)	P_2O_5 (wt.%)	CO_2 (wt.%)	B (ppm)	Sm (ppm)	Gd (ppm)	U (ppm)	Th (ppm)	Volumetric H_2O
AF-1-13	63.57	0.68	17.08	5.03	0.07	1.99	5.15	3.73	2.10	0.04	0.36	19.13	3.12	2.23	2.3	7.12	0.009
AF-2-13	63.57	0.68	17.08	5.03	0.07	1.99	5.15	3.73	2.10	0.04	0.36	19.13	3.12	2.23	2.3	7.12	0.009
AF-3-13	64.42	0.641	16.82	4.41	0.067	1.48	4.52	3.93	2.15	0.02	0.335	19.4	2.8	2.1	1.7	6.0	0.008
AF-4-13	64.10	0.666	16.63	4.82	0.073	1.57	4.72	3.68	2.01	0.03	0.315	20.0	2.9	2.0	1.6	5.9	0.008
AF-1-14	63.92	0.677	17.54	4.77	0.070	1.77	5.11	3.95	2.06	0.05	0.385	19.8	2.8	2.0	1.7	5.7	0.010
AF-2-14	62.78	0.729	17.69	5.23	0.072	2.20	5.53	3.85	1.91	0.06	0.395	14.3	3.0	2.0	1.4	4.9	0.010
AF-3-14	63.57	0.68	17.08	5.03	0.07	1.99	5.15	3.73	2.10	0.04	0.36	19.13	3.12	2.23	2.3	7.12	0.009
AF-5-14	63.18	0.673	17.28	5.39	0.077	2.27	5.42	3.51	2.29	0.05	0.375	15.9	3.4	2.7	3.7	10.4	0.009
AF-6-14	63.02	0.691	16.54	5.54	0.079	2.7	5.58	3.43	2.20	0.08	0.365	25.4	3.8	2.6	3.7	9.8	0.009
AFDP-1-14	63.57	0.68	17.08	5.03	0.07	1.99	5.15	3.73	2.10	0.04	0.36	19.13	3.12	2.23	2.3	7.12	0.009
AFDP-2-14	63.57	0.68	17.08	5.03	0.07	1.99	5.15	3.73	2.10	0.04	0.36	19.13	3.12	2.23	2.3	7.12	0.009
DF3-B1-13	60.16	1.069	14.34	8.71	0.124	3.26	5.07	2.64	2.45	0.17	0.550	31.1	6.3	4.9	6.3	12.1	0.013
DF3-B2-13	59.64	1.107	15.43	8.92	0.133	3.27	5.45	3.08	2.50	0.02	0.460	28.5	6.1	5.1	5.5	11.9	0.011
DF1-B1-14	63.62	0.999	13.67	7.87	0.117	3.13	4.13	2.61	3.24	0.04	0.520	25.3	6.0	4.7	7.9	17.0	0.012
DF1-B2-14	62.58	1.043	14.23	8.05	0.113	2.99	4.24	2.69	3.15	0.04	0.420	20.7	5.8	4.5	7.6	17.1	0.010
DF1-B3-14	60.48	0.750	17.47	6.19	0.096	2.83	5.86	3.46	1.85	0.04	0.385	13.2	3.2	2.3	1.4	4.2	0.010
DF6-B1-14	65.98	0.491	17.55	3.49	0.055	0.91	4.32	3.91	2.79	0.01	0.265	17.1	5.1	3.7	4.4	13.9	0.006
DF6-B2-14	67.40	0.555	16.67	3.74	0.054	0.94	4.01	3.86	3.17	0.02	0.170	10.5	5.1	3.7	5.2	15.5	0.004
DF6-B3-14	64.83	0.587	17.37	4.14	0.069	1.49	4.55	3.40	3.27	0.03	0.350	14.3	5.4	3.0	4.4	21.3	0.008
								Depth Profile									
AFDP-14-35	63.57	0.68	17.08	5.03	0.07	1.99	5.15	3.73	2.10	0.04	0.36	19.13	3.12	2.23	2.3	7.12	0.009
AFDP-14-65	63.57	0.68	17.08	5.03	0.07	1.99	5.15	3.73	2.10	0.04	0.36	19.13	3.12	2.23	2.3	7.12	0.009
AFDP-14-200	63.57	0.68	17.08	5.03	0.07	1.99	5.15	3.73	2.10	0.04	0.36	19.13	3.12	2.23	2.3	7.12	0.009
AFDP-14-400	63.57	0.68	17.08	5.03	0.07	1.99	5.15	3.73	2.10	0.04	0.36	19.13	3.12	2.23	2.3	7.12	0.009
AFDP-14-500	63.57	0.68	17.08	5.03	0.07	1.99	5.15	3.73	2.10	0.04	0.36	19.13	3.12	2.23	2.3	7.12	0.009
AFDP-14-600	63.57	0.68	17.08	5.03	0.07	1.99	5.15	3.73	2.10	0.04	0.36	19.13	3.12	2.23	2.3	7.12	0.009

Table 3-2.

Attributes, site information, AMS measured ^{36}Cl concentrations, and exposure ages for alluvial fan and debris flow complex samples.

Sample No.	Latitude (°S)	Longitude (°W)	Elevation (m)	Deposit [1]	Material	Thickness (cm)	Topographic Shielding	Cl_{Rock} (ppm)	$^{36}Cl/Cl$ (10^{-15})	^{36}Cl (10^6 at g^{-1})	Exposure Age [2] (ka)
AF-1-13	23.14525	68.00323	2627	QG	Andesite	3.0	0.999	10.7 ± 0.39	2974.66 ± 86.61	3.088 ± 0.091	20.7 ± 1.4
AF-2-13	23.14688	68.00283	2626	QG	Andesite	3.0	0.999	10.0 ± 0.43	3434.82 ± 72.03	3.298 ± 0.073	22.4 ± 1.4
AF-3-13	23.14417	68.01749	2498	AF	Andesite	3.0	0.999	25.9 ± 0.91	2925.17 ± 84.89	3.313 ± 0.101	53.1 ± 3.6
AF-4-13	23.14431	68.01879	2482	AF	Andesite	3.0	0.999	49.5 ± 2.36	2158.94 ± 78.61	3.177 ± 0.144	69.5 ± 5.5
AF-1-14	23.11884	68.03659	2440	AF	Andesite	3.0	0.999	32.4 ± 0.78	1108.43 ± 17.97	1.262 ± 0.024	23.4 ± 1.6
AF-2-14	23.11917	68.03588	2443	AF	Andesite	3.0	0.999	83.4 ± 0.79	1295.34 ± 20.33	2.595 ± 0.044	58.0 ± 3.3
AF-3-14	23.11884	68.01939	2469	AF	Andesite	3.0	0.999	73.7 ± 3.80	1043.27 ± 25.57	2.282 ± 0.088	41.2 ± 3.2
AF-5-14	23.27193	67.99696	2477	AF	Andesite	3.0	0.999	122.5 ± 4.34	2438.32 ± 35.88	6.524 ± 0.203	145. 1 ± 9.7
AF-6-14	23.27420	67.97386	2644	QG	Andesite	3.0	0.999	133.7 ± 10.18	5325.59 ± 65.16	15.298 ± 0.939	419.3 ± 39.7
AFDP-1-14	23.17648	68.01833	2456	AF	Andesite	3.0	0.999	20.1 ± 0.71	3054.95 ± 64.77	3.317 ± 0.079	30.4 ± 2.3
AFDP-2-14	23.17556	68.01605	2468	AF	Andesite	3.0	0.999	13.4 ± 0.35	4033.35 ± 83.86	3.939 ± 0.085	35.7 ± 2.2
DF3-B1-13	23.14434	68.01790	2481	DF	Ignimbrite	4.0	0.999	344.5 ± 57.30	1124.9 ± 33.43	7.307 ± 1.116	118.7 ± 21.6
DF3-B2-13	23.14347	68.01958	2475	DF	Ignimbrite	5.0	0.999	345.5 ± 43.42	204.62 ± 6.62	1.327 ± 0.157	16.7 ± 2.7
DF1-B1-14	23.11797	68.04921	2409	DF	Ignimbrite	4.0	0.999	234.3 ± 4.88	336.15 ± 8.87	1.537 ± 0.049	24.0 ± 1.7
DF1-B2-14	23.11773	68.05075	2404	DF	Ignimbrite	5.0	0.999	287.2 ± 10.32	348.97 ± 8.56	1.910 ± 0.077	26.5 ± 2.1
DF1-B3-14	23.11505	68.06631	2375	DF	Andesite	2.0	0.999	153.8 ± 11.95	2454.30 ± 45.62	7.897 ± 0.519	202.6 ± 19.7
DF6-B1-14	23.22236	68.01277	2450	DF	Ignimbrite	2.5	0.999	192.4 ± 11.64	276.64 ± 6.14	1.066 ± 0.059	16.4 ± 1.6
DF6-B2-14	22.22234	68.01281	2434	DF	Ignimbrite	5.5	0.995	200.3 ± 13.03	188.32 ± 4.79	0.751 ± 0.046	9.3 ± 1.1
DF6-B3-14	23.22248	68.01318	2439	DF	Ignimbrite	3.5	0.999	276.0 ± 21.00	207.77 ± 4.54	1.095 ± 0.078	12.3 ± 1.6
						Depth Profile					
AFDP-14-35	23.17689	68.01970	2450	AF	Andesite	3.0	-	9.8 ± 0.17	3182.55 ± 68.87	3.003 ± 0.065	-
AFDP-14-65	23.17689	68.01970	2450	AF	Andesite	3.0	-	13.6 ± 0.22	2317.45 ± 39.89	2.256 ± 0.039	-
AFDP-14-200	23.17689	68.01970	2450	AF	Andesite	3.0	-	17.6 ± 0.65	576.52 ± 11.75	0.614 ± 0.014	-
AFDP-14-400	23.17689	68.01970	2450	AF	Andesite	3.0	-	18.2 ± 0.78	174.49 ± 5.36	0.189 ± 0.006	-
AFDP-14-500	23.17689	68.01970	2450	AF	Andesite	3.0	-	13.9 ± 0.56	136.06 ± 4.04	0.132 ± 0.004	-
AFDP-14-600	23.17689	68.01970	2450	AF	Andesite	3.0	-	12.3 ± 0.36	123.64 ± 4.22	0.117 ± 0.004	-

[1] Landform sampled, AF: alluvial fan, DF: debris flow, QG: Quaternary Gravel.

[2] Exposure ages calculated by means of time-varying Lal/Stone scaling using Phillips, 1996 ^{36}Cl calibration set

Table 3-3

Elemental concentrations, water content, and cosmic dose rate for total dose rate estimation.

Sample No.	K (%) [a]	U (ppm) [a]	Th (ppm) [a]	Water Content (%)[b]	Cosmic (μGy/ka) [c]	Total Dose Rate (Gy/ka) [d]
Chaj-OSL1	1.61 ± 0.08	2.50 ± 0.25	9.20 ± 0.17	5 ± 0.5	240 ± 24	2.85 ± 0.14
Toc-OSL1	1.36 ± 0.07	2.80 ± 0.28	8.20 ± 0.37	5 ± 0.5	149 ± 15	2.53 ± 0.13

[a]Elemental concentrations from FUS-ICP of whole sediment measured at Activation Laboratories, Ontario. Uncertainties are taken to be ± 10 %.
[b]Water content taken as 5% to account for the uncertainty over the timescale.
[c]Cosmic dose rate calculated using the methods of Prescott and Hutton (1994).
[d]Methods of Adamiec and Aitken (1998) and Mejdahl (1979) used to combine cosmic dose rate with β and ɣ doses from elemental concentration to calculate the total dose rate.

\

Table 3-4

Sample location, equivalent dose (D_E), dose rate, and calculated ages for OSL samples. Measurements used the single aliquot regenerative dose (SAR) method. Ages calculated by means of software by Grün (2009).

Sample No.	Latitude (°S)	Longitude (°W)	Elevation (m)	Depth (cm)	Disks Used *	Equivalent Dose w/ ±1 σ error (Gy) Weighted Mean	Dose Rate (Gy/ka)	Age w/ ±1 σ error (ka) Weighted Mean
Chaj-OSL1	23.06929	67.92152	3443	200	22(40)	115 ± 1.1	2.85 ± 0.14	40.5 ± 2.0
Toc-OSL1	23.17689	68.01970	2450	380	23(40)	108.2 ± 1.0	2.53 ± 0.13	42.9 ± 2.0

*Total number of aliquots measured listed inside the parentheses, number of aliquots which satisfy recuperation criteria and are considered for age calculation listed outside the parentheses.

Chapter 4: Interpretations

4.1 Introduction

Cosmogenic exposure ages determined as part of this study obtained along the western margin of the Chajnantor Plateau permit the construction of a detailed chronology of the Chajnantor fan complex. These new ages aid in elucidating sedimentary processes active along a previously glaciated plateau in a near-hyperarid environment. Previous cosmogenic studies in the Atacama Desert point toward preserved relict surfaces of Miocene-Pliocene age (Nishiizumi et al., 2005; Dunai et al., 2006, Evenstar et al., 2009). Other previous studies revealed surfaces of latest Pliocene-Pleistocene age, suggesting active Quaternary modification and fluvial activity in the landscape (Gonzales et al., 2006; Placzek et al., 2010; Amundson et al., 2012; Jungers et al., 2013; Placzek et al., 2014). New exposure ages for the Chajnantor fan complex imply a youthful alluvial system, and suggest late Pleistocene – early Holocene landscape modification and fluvial activity. Surface exposure ages among the Chajnantor fans and debris flows can be correlated with regional paleoclimate records and local glacial stages on the Chajnantor Plateau. These correlations have implications for the primary controls on sedimentation, and a comparison to other studies offers insight to regional depositional systems.

4.2 Aggradation and Incision History from TCN Exposure Ages

Alluvial surfaces of the Chajnantor fan complex and associated debris flow deposits are locally extensive and imply episodic deposition throughout the late Pleistocene and early Holocene. Several morphostratigraphically distinct surfaces have been documented through geomorphic mapping coupled with cosmogenic ^{36}Cl exposure ages. Three distinct alluvial fan surfaces, labeled from oldest to youngest as *Qcf1*, *Qcf2*, *Qcf3* (Fig. 4-1), and three distinct plateau gravel surfaces, labeled from oldest to youngest as *Qpg1*, *Qpg2a* and *Qpg2b*, *Qpg3* (Fig. 4-1), were identified in the study area. The alluvial fan surfaces are dissected by active channels and modern alluvium, *Qm*, as well as several debris flow surfaces, *Qd* (Fig. 4-1). The alluvial fans likely represent a flash-flood controlled alluvial system, driven by infrequent

storm events. This interpretation is corroborated by the thick, poorly sorted, coarse andesite cobbles that compose the deposits, requiring a substantial amount of energy to mobilize. The material of these fans is likely sourced from plateau gravels that occupy the upper reaches of the ignimbrite shield. These plateau gravel deposits are diamictic, and contain abundant andesite. They likely include an amalgamation of lahar and debris flow deposits, volcanogenic sediment, and periglacial sediment.

Following the emplacement of the Cajón ignimbrite around ~1.38 Ma, the Chajnantor Plateau channels began to form, with erosion focused along fractures in the ignimbrite sheets. The timing of upper plateau gravel generation is poorly constrained, as are the crystallization ages of the andesitic peaks (Co. Negro, Co. de Macón, etc.) that ornament the plateau (Fig 4-2). Because the gravel deposits include lahar and debris flow deposits, and abundant volcanogenic sediment, their generation may have been concurrent with the development of the andesitic peaks. These diamictic gravel deposits were subsequently cannibalized and their material distributed along the base of the Chajnantor Plateau to form the coalescing alluvial deposits of the Chajnantor fan complex. The alluvial surfaces of this bajada were then reworked and incised with more modern fluvial channels and debris flow events.

4.2.1 Age and Evolution of Plateau Gravels and Debris Flow Deposits

Incised and dissected gravel deposits perched on the upper ignimbrite shield compose the *Qpg1* surface (Fig. 4-1). These remnant gravel deposits are dissected by deep bedrock channels, implying that they have long since been abandoned. Clasts on the *Qpg1* surface exhibit substantial ventifaction and desert varnish on the leeward face. A single ^{36}Cl exposure age from an amalgamation of surface cobbles of 419.3 ± 39.7 ka was obtained for the surface. As these perched gravels are presumably the amalgamations of lahar deposits and various other reworked sediments concentration-depth profiles were not constructed for these surfaces. As such, the surface exposure ages calculated represent a maximum age of the deposit. Typically, inheritance contributes a minor nuclide signal among more mature deposits, as the inherited nuclide concentration is smaller than the large accumulation since the formation of the

deposit, along with nuclide decay which results in a substantial removal of the inherited component. Due to the surface exposure age surpassing one half-life of the ^{36}Cl nuclide, presumably the inherited component has been substantially reduced. The age for the *Qpg1* surface is interpreted to be 419.3 ± 39.7 ka.

The *Qpg2a* and *Qpg2b* surfaces comprise coherent gravels on the upper and lower ignimbrite shield (Fig. 4-1). The morphology of the *Qpg2* surface implies that it is substantially younger than *Qpg1* because the as gravel surface is not dissected. Ramírez and Gardeweg (1982) mapped the southernmost *Qpg2a* surface as a lahar deposit; and the morphology of the surface supports this interpretation. No ^{36}Cl exposure ages were obtained from the *Qpg2a* surface; however the surface is actively being reworked and transported and appears to be a source of material for *Qcf3* and *Qpg3* surfaces. The northernmost *Qpg2a* surface appears to have been cannibalized to form the *Qpg2b* surface. An age from a single OSL sample from the subsurface of this deposit yields an age of 40.5 ± 2.0 ka. Thus, the *Qpg2b* surface must have an exposure age less than ~ 40 ka, and the interpreted age for *Qpg2a* is >40 ka.

The youngest gravel surface on the ignimbrite shield is the *Qpg3* surface (Fig. 4-1). The *Qpg3* surface consists of scattered, isolated andesitic gravel patches that are dispersed across the lower reaches of the ignimbrite shield adjacent to bedrock channels (Fig. 4-1). Surface exposure ages for the *Qpg3* surface of 20.7 ± 1.4 ka and 22.4 ± 1.4 ka. The interpreted age of the *Qpg3* surface is 21.6 ± 0.8 ka, the average of these two ages.

Debris flow deposits entrained among the alluvial surfaces compose the *Qd* surface (Fig 4-1). These deposits are typically confined to channels that have incised the alluvial packages, some of which appear to be active during infrequent storm events. Surface exposure ages for the *Qd* surface range from 9.3 ± 1.1 ka to 202.6 ± 19.7 ka (Table 4-1). The PDF exhibits five peaks at ~10 ka, ~16 ka, ~25 ka, ~118 ka, and ~202 ka (Fig. 4-3). The peaks observed at ~10 ka, ~16 ka, ~118 ka, and ~202 ka consist of single samples. Sample DF1-B3-14 is an andesite boulder that was collected near the distal margin of the debris

surface and yields an age of 202.59 ± 19.66 ka. This notably older age may suggest that the distal margin of the deposit was deposited much earlier than the boulders proximal to the plateau, or it may imply a significant inherited nuclide component. Due to the resistant nature of andesite, it is possible that the boulder was not eroded during transport and retained a substantial inherited nuclide signal. The andesitic lithology implies the sample was also sourced from deposits on the upper reaches of the plateau, rather than generated from bedrock within the fracture-controlled channels. This evidence suggests that this particular boulder has experienced a more complicated exposure history, and likely had significant nuclide inheritance prior to deposition. However, this inheritance does not preclude the interpretation that the distal margin represents an earlier depositional event. Sample DF3-B1-13 also displays an older age of 118.7 ± 21.6 ka. Because this sample is proximal to the plateau front indicating shorter and younger transport, the older age is likely the product of a substantial inherited nuclide signal. Removing these two outliers from the PDF produces four peaks at ~10 ka, ~12 ka, ~16ka, and ~25 ka. Average exposure ages for individual deposits determined by analyzing multiple boulders on the *Qd* surface yield ages of 12.7 ± 2.1 ka, 16.7 ± 2.7, and 25.3 ± 1.3 ka. These average exposure ages suggest that individual deposits of the *Qd* surface have developed during different periods of deposition, but appear to be restricted to the last ~25 ka.

4.2.2 Age and Evolution of the Chajnantor Alluvial Fans

The ^{36}Cl exposure ages obtained in this study are interpreted to reflect abandonment ages, where a shift from aggradation to incision was a consequence of variations between transport capacity and sediment supply. Surface exposure ages calculated for debris flow boulders are treated as maxima, due to the inability to constrain inheritance.

The *Qcf1* surface is confined to a few discontinuous remnant fragments in the southern portion of the study area, adjacent to V. Lascar. Presumably the surface had a greater extent but its area has been diminished by periods of incision (Fig 4-1). The fan unit is defined by a single surface exposure age at

145.1 ± 9.7 ka (Table 4-1). When compared to the younger fan surfaces *Qcf2* and *Qcf3*, the morphology of surface *Qcf1* supports an older exposure age. As only one sample was dated from this surface, 145.1 ± 9.7 ka is the interpreted age for the *Qcf1* fan surface.

The *Qcf2* fan surface displays widely distributed remnants across the alluvial apron; however it has also been subjected to significant dissection and incision (Fig. 4-1). Five ^{36}Cl exposure ages obtained from the *Qcf2* surface exhibit a wide range from 23.4 ± 1.6 ka to 69.5 ± 5.5 ka (Table 4-1). Satellite imagery suggests that sample AF-1-14 appears to have been obtained from a secondary channel on the *Qcf2* surface and has likely been subjected to reworking post-deposition, thus resulting in the anomalously young exposure age of 23.4 ± 1.6 ka. Removing sample AF-1-14 brings the spread of ages to 41.2 ± 3.2 ka to 69.5 ± 5.5 ka. The PDF displays a bimodal distribution of the ages, a consequence of the limited sample size producing artifacts. A primary peak is observed at ~59 ka and consists of two samples, while the secondary peak at ~41 ka results from an individual sample. The primary peak at ~59 ka exhibits a positive skew (Fig. 4-2). Given these samples, the most probable age for the abandonment of the *Qcf2* surface is 55.5 ± 3.6 ka.

The most recent alluvial fan surface is the *Qcf3* surface (Fig. 4-1). Two ^{36}Cl exposure ages were obtained from the surface, 30.4 ± 2.3 ka and 35.7 ± 2.2 ka. These surface ages are corroborated by a concentration-depth profile obtained from the subsurface, and are in stratigraphic agreement with an OSL age of 42.9 ± 2.0 ka obtained \ 3.8 m below the surface. The PDF displays a slight bimodal distribution, again a consequence of the limited sample size. The two samples produce peaks at ~35 ka and ~31 ka (Fig. 4-2). A likely age for the *Qcf3* surface is 33.0 ± 2.7 ka. This young age is also supported by the morphology of the surface when compared to surface *Qcf1* as well as by stratigraphic relationships among deposits, confirming that thee *Qcf3* surface is a more recent aggradational event that overlies the *Qcf2* surface.

4.2.3 Synopsis of Local Sedimentary Processes

Cosmogenic ^{36}Cl exposure ages of Chajnantor fan surfaces and associated debris flows indicate active fluvial processes over the last ~145 ka. Surface exposure ages for diamictic gravel packages on the adjacent plateau imply dynamic sediment production and storage over the last ~419 ka. Three periods of surface abandonment among the Chajnantor fans are recognized at ~33 ka, ~55 ka, and ~145 ka. Over the past ~25 ka, a debris flow surface has developed through multiple episodes of deposition. This set of surface exposure ages suggest that aggradation and remobilization of sediment are dominant processes that operate over long time windows, and are punctuated by shorter periods of incision (Dühnforth et al., 2012). The relatively narrow range of exposure ages on alluvial surfaces suggests that they are abandoned rapidly.

When the sediment supply from the upper reaches of the plateau is exhausted incision becomes a dominant control on the both bedrock and alluvial surfaces. Without substantial material to transport, flood events re-excavate and incise into the bedrock channels on the ignimbrite shield, generating boulders that become entrained in the narrow channels. Eventually, a sufficiently large precipitation event will occur and material from the channel gets "flushed" onto the alluvial surfaces, depositing the boulders. Sediment stored in the gravel packages on the plateau surfaces was likely to have been predominantly generated by lahar and debris flow events, with a minor periglacial component. While historical events elsewhere on the plateau suggest volcanogenic sediments, i.e. large localized lahar deposits, are actively being generated (Sparks et al., 1997), presumably the accumulation of substantial sediment mass over the entire plateau takes time. The minimal inherited nuclide signal expressed in the TCN depth profile implies that the time between "original" fan deposition on the upper elevations of the plateau and subsequent erosion was short. This suggests a rapid erosion and transport time between deposits. This may imply a short residence time on the plateau surface, however, it does not preclude the possibility of a long residence time on the plateau surface with the majority of sediment buried in thick deposits.

4.3 Correlation with Climate Records

The relationship between alluvial fan development and climate has important implications for understanding the dominant controls on alluvial systems. An increase in precipitation, or an increase in the frequency of large storm events, may promote rapid striping of upland sediment and lead to incision. An increase in precipitation coupled with colder temperatures may promote glaciation of adjacent uplands and provide a sediment source, thus resulting in fan aggradation. The influence of glacial – interglacial cyclicity on fan formation is particularly relevant to our study area, as glacial occupation of the adjacent plateau may provide a source of sediment for the alluvial apron. Additionally, the glaciation may suggest an increase in annual precipitation for the region.

Church and Ryder (1972) suggest that a paraglacial cycle of sediment supply can induce fan development during deglaciation followed by fan entrenchment as glacial sediment sources are exhausted. Glaciation of the Chajnantor Plateau, while extensive, was likely not deeply erosive (Ward et. al., in review), and thus did not generate a substantial sediment supply. This precludes deglaciation as the dominant supply of sediment to the alluvial system. However, glaciation of the plateau does suggest a regional increase in precipitation which is observed among the paleoclimate records. Aggradation and development of the alluvial fans coincident with local glaciations, wet phases of the salars, and paleowetland deposits, would suggest that an increase in mean annual precipitation or an increased frequency of storm events likely induces alluvial fan formation on the Chajnantor Plateau (Bull and Schick, 1979; Enzel et al., 2012)

Cosmogenic ^{36}Cl exposure ages recording the abandonment of the alluvial surfaces among the Chajnantor fan complex appear to correlate with negative excursions of the marine oxygen isotope record (Fig. 4-4). This correlation suggests that the fans are associated with global cooling events, and thus glaciations. Ward and others (in review) identify three stages of moraine stabilization on the Chajnantor Plateau, with stage III stabilization around >100 ka, stage II stabilization at ~50 ka and stage I

stabilization at ~25-30 ka. These stages of glacial occupation of the Chajnantor Plateau are synchronous with wet phases of the Salar de Atacama (Bobst et al., 2001) and Salar de Uyuni (Baker et al., 2001). The three phases of alluvial surface abandonment of the Chajnantor fan complex coincide with these moraine stabilizations and wet phases of the salars. Abandonment of surface *Qcf3* coincides with stage I deglaciation and abandonment of surface *Qcf2* coincides with stage II deglaciation. Surface *Qcf1* may correspond to stage III deglaciation; however there are insufficient constraints for the timing of both events. Rodent midden records for the Atacama Desert are typically brief and only cover the last ~22 ka. However, Maldonado and others (2005) describe a 50 ka rodent midden series from the southern Atacama Desert. Pollen records from the middens suggest an increase in winter precipitation around >52 ka, 40-33 ka, and 24-17 ka. The record of increased precipitation coincides with glaciation of the Chajnantor Plateau and the development of the *Qcf2* and *Qcf3* surfaces.

The correlation between abandonment ages of the alluvial surfaces and glacial occupation of the plateau coupled with increased periods of precipitation (recorded in the marine isotope record) suggests that climate is the primary driver of alluvial fan development along the Chajnantor Plateau. It is our interpretation that surface occupation occurs during glacial times and that incision and surface abandonment occurs during interglacial periods (Dühnforth et al., 2012). The present interglacial embodies a period of incision, in which alluvial surface aggradation appears to be negligible. This is supported by the abundance of debris flow deposits that are confined to the active channels and have exposure ages between 24 ka and 9 ka. The abandoned alluvial surfaces and debris flow deposits suggest that the landscape has transitioned from an aggradational to an incisional setting post MIS II. Previous interglacial periods are not observed in the debris flow boulders, which may be the consequence of limited sampling or the deposits may be buried beneath younger alluvium.

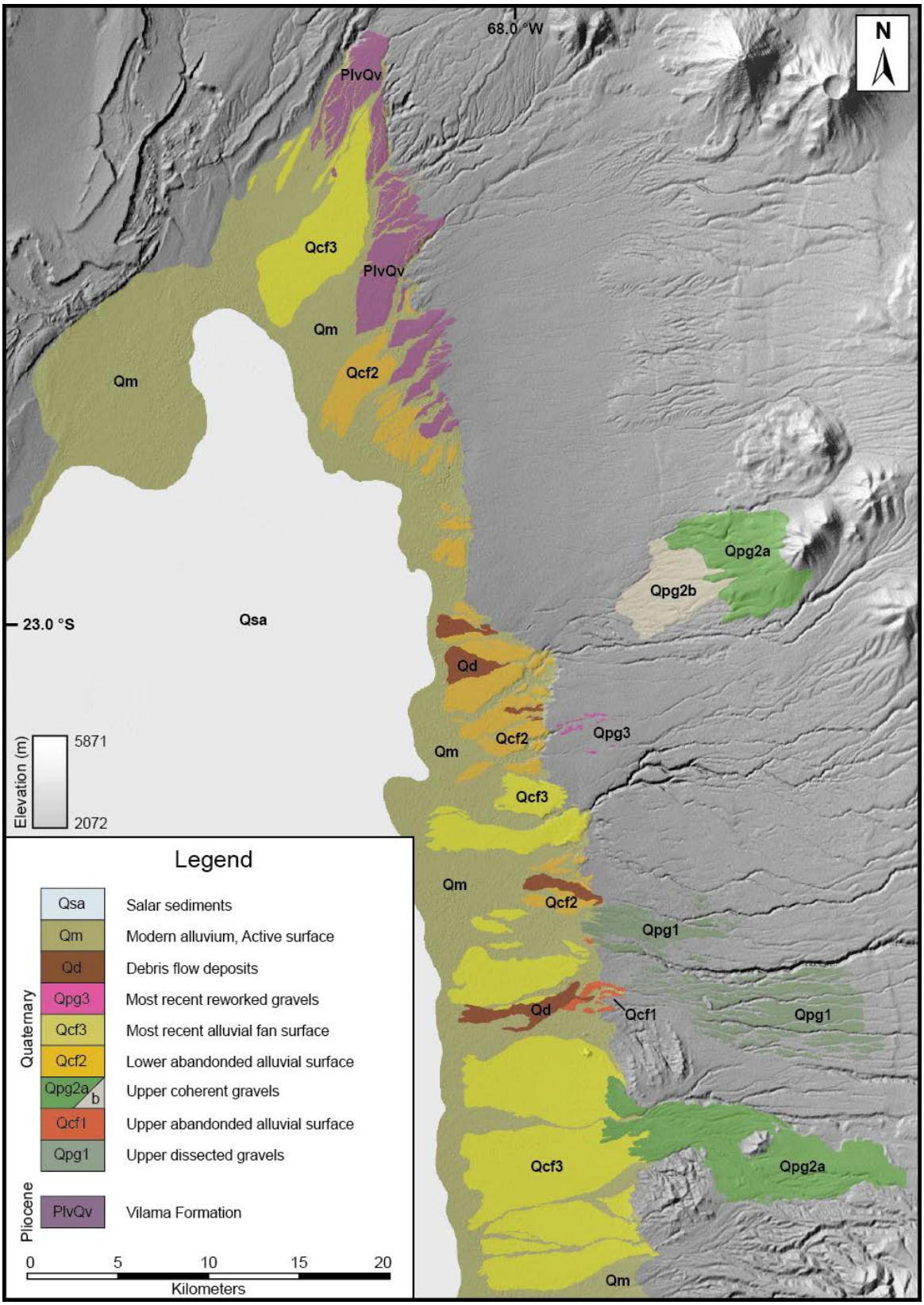

Figure 4-1: Geomorphic map of the Chajnantor fan complex and associated surficial deposits.

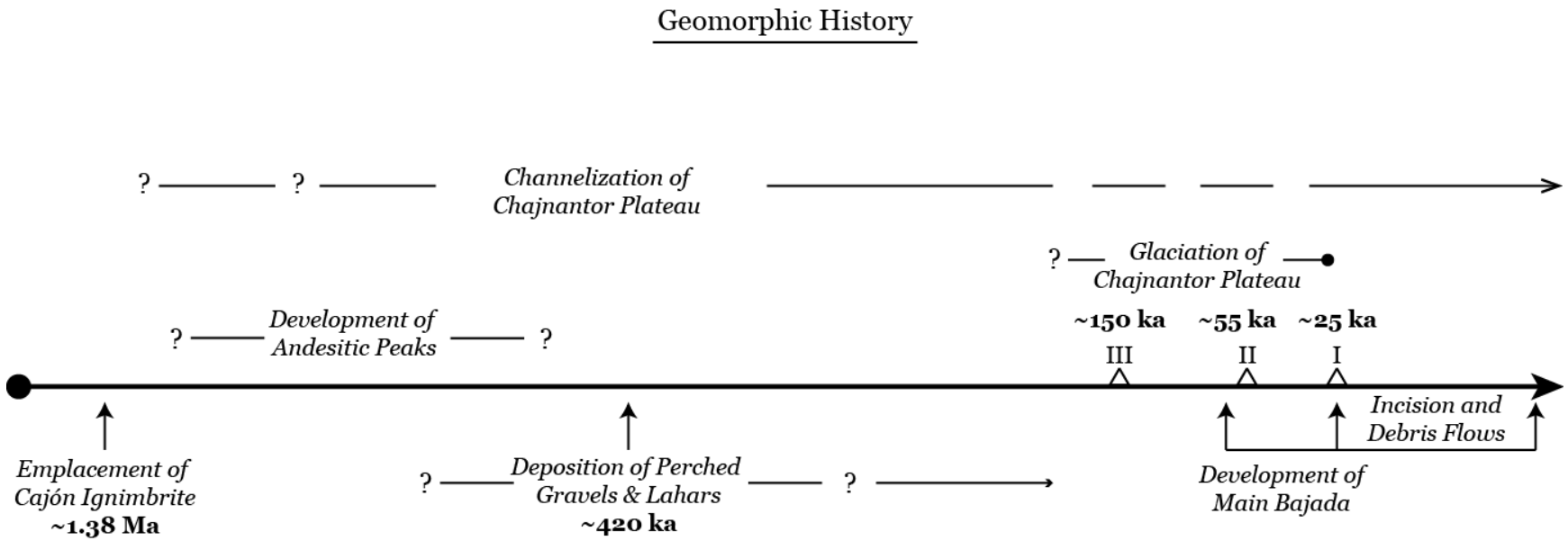

Figure 4-2. Generalized geomorphic history of the Chajnantor Plateau and associated sedimentary deposits with timing and current age constraints as known. Note that timeline is not to scale.

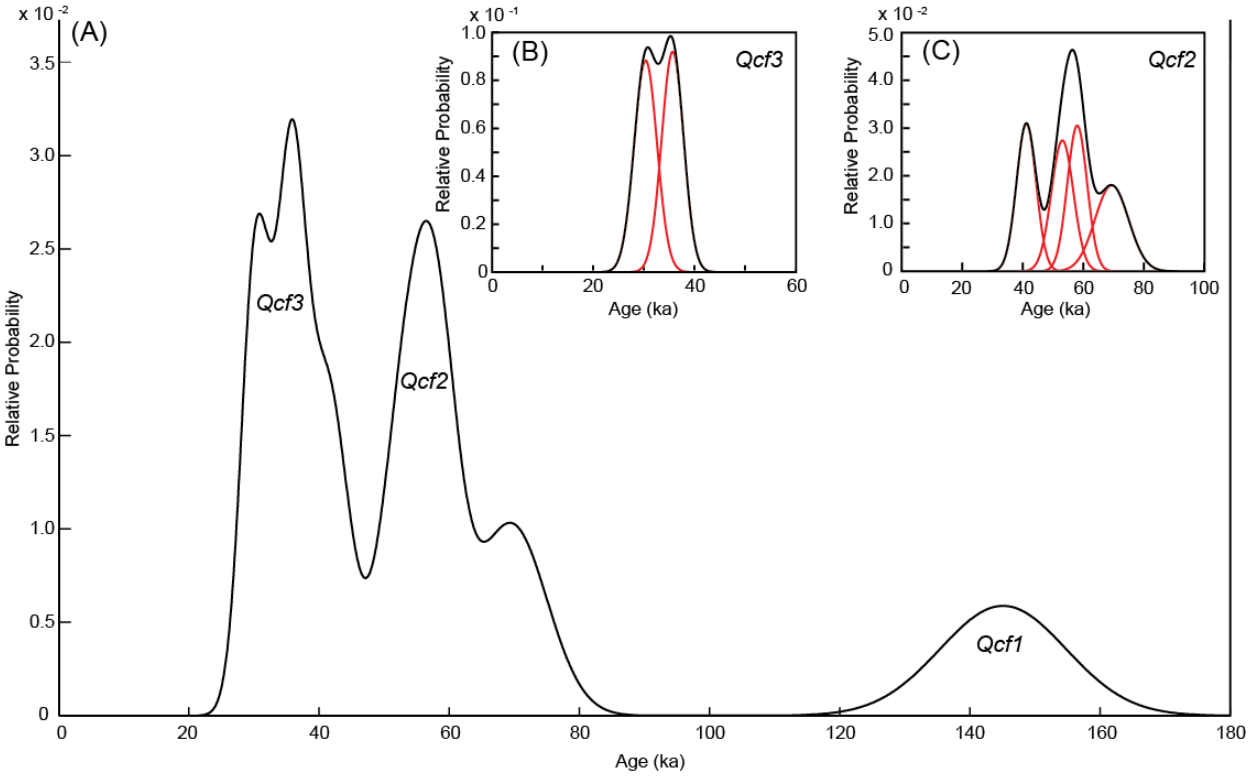

Figure 4-3: A: Probability Density Function (PDF) for ^{36}Cl ages on alluvial surfaces of the Chajnantor alluvial apron. Curve represents the sum of individual distributions. B: PDF plot for surface *Qcf3*. The surface exhibits a most probable peak at ~35 ka. C: PDF plot for surface *Qcf2*. Surface illustrates a most probable peak at ~59 ka, however significant dispersion is observed. Red curves in (B) and (C) represent individual samples that make up the PDF curve.

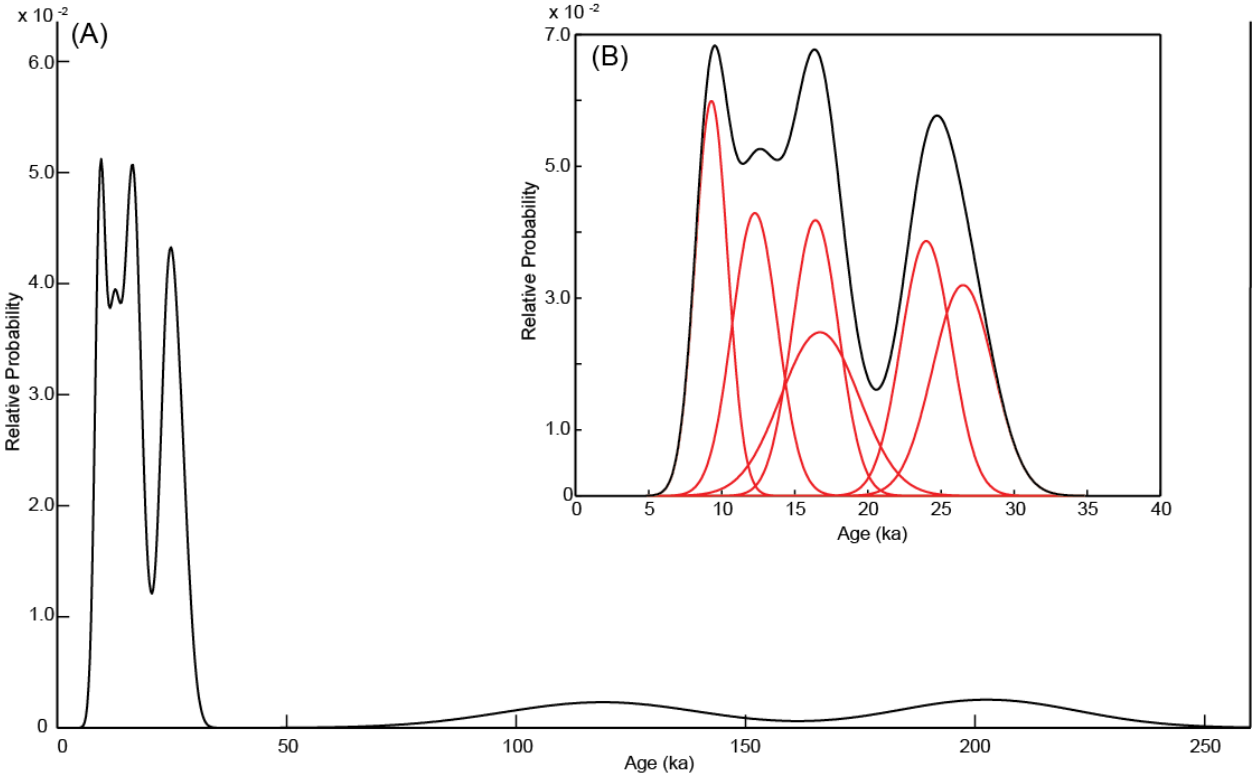

Figure 4-4: A: Probability Density Function (PDF) for ^{36}Cl ages on boulders of surface *Qd* displaying most probable peaks at ~10 ka, ~16 ka, and ~25 ka. B: PDF for surface *Qd* with the removal of samples DF1-B3-14 and DF3-B1-13. Without these two samples, the PDF displays most probable peaks at ~10 ka, ~12 ka, ~16 ka, and ~25 ka for surface *Qd*. Red curves in (B) represent individual samples that make up the PDF curve.

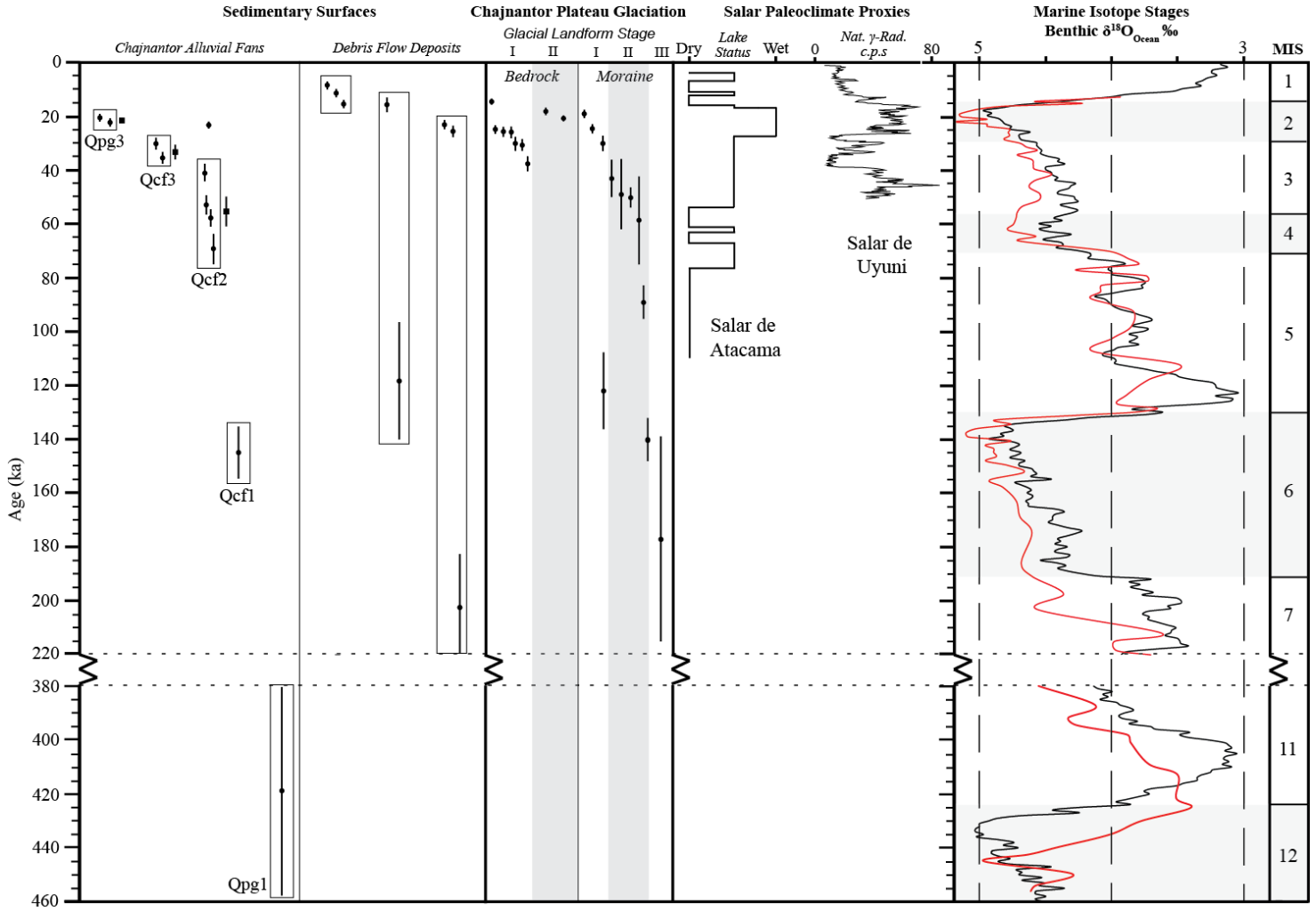

Figure 4-5. Distribution of ^{36}Cl exposure ages for alluvial fan surfaces, plateau gravels, and debris flow deposits, ages of Chajnantor glaciations, and climate proxies. For sedimentary surfaces, black circles within the boxes represent individual ^{36}Cl ages for amalgamated samples on the fan surface, squares represent mean ages with standard error for the respective surface. Chajnantor Plateau glaciated data shows scoured bedrock and moraine boulder ^{10}Be and ^{36}Cl ages from the Chajnantor Plateau from Ward and others in review. Paleoclimate proxies are sedimentary lake level proxies from the Salar de Atacama as described in Bobst and others (2001) and the Salar de Uyuni (Baker et al., 2001a). Marine isotope stage data show globally distributed benthic δ^{18}O records of Lisiecki and Raymo (2005) in black, and regional benthic δ^{18}O from IODP core 677 off the Peruvian coast as described in Raymo and others (1997) in red.

Table 4-1: Summary of ^{36}Cl ages for designated geomorphic surfaces (MIS = marine oxygen isotope stage).

Surface	Sample	^{36}Cl Exposure Age (ka)[a b]	Period
Qm	Not Sampled	Not Dated	Historical/Active
Qd	DF6-B2-14	9.3 ± 1.1	Holocene / MIS I
	DF6-B3-14	12.3 ± 1.6	MIS I
	DF6-B1-14	16.4 ± 1.6	MIS II
	DF3-B2-13	16.7 ± 2.7	MIS II
	DF1-B1-14	24.0 ± 1.7	MIS II
	DF1-B2-14	26.5 ± 2.1	MIS II
	DF3-B1-13	118.7 ± 21.6	MIS V
	DF1-B3-14	202.6 ± 19.7	MIS VI
Qpg3	AF-1-13	20.7 ± 1.4	MIS II
	AF-2-13	22.4 ± 1.4	MIS II
		21.6 ± 0.8	
Qcf3	AFDP-1-14	30.4 ± 2.3	MIS III
	AFDP-2-14	35.7 ± 2.2	MIS III
		33.0 ± 2.7	
Qcf2	~~AF-1-14~~	~~23.4 ± 1.6~~	MIS II
	AF-3-14	41.2 ± 3.2	MIS III
	AF-3-13	53.1 ± 3.6	MIS III
	AF-2-14	58. ± 3.3	MIS IV
	AF-4-13	69.5 ± 5.5	MIS IV
		55.5 ± 3.6	
Qpg2a/b	Not Sampled	Not Dated	≥ MIS III/II
Qcf1	AF-5-14	145. 1 ± 9.7	MIS VI
Qpg1	AF-6-14	419.3 ± 39.7	MIS XI

[a] Uncertainty expressed as 1 σ for individual ages and standard error for mean ages.

[b] Samples with ~~text~~ not included in calculation of mean age for the surface, excluded on geologic context.

Chapter 5: Conclusions

The coalescing gravel fans along the western flank of the Chajnantor Plateau in northern Chile preserve an extensive record of sedimentation in a near hyperarid environment. Remnant alluvial surfaces and terraces imply extended periods of aggradation that are punctuated by periods of incision. The landscape is currently in state of incision, and the packages of alluvial fans along the lower slope of the Chajnantor Plateau are being incised.

Cosmogenic ^{36}Cl exposure ages from a series of alluvial fan surfaces and debris flow deposits reveal late Pleistocene to Holocene landscape modification in the region. One local (*Qcf1*) and two extensive (*Qcf2* and *Qcf3*) abandoned alluvial fan surfaces are observed, in addition to what appear to be three distinct diamictic gravel-and-lahar deposits on the upper and lower reaches of the plateau (*Qpg3*, *Qpg2*, and *Qpg1*). Numerous debris flow deposits represented by boulder fields compose the youngest surface, *Qd*, and are confined to active and ancient channels among the alluvial surfaces.

Protracted periods of aggradation coincide with periods of increased precipitation and glacial occupation of the Chajnantor Plateau. These periods of aggradation are punctuated by periods of incision and surface abandonment that correlate with deglaciation events at ~25-30ka, ~55ka, and ~145ka. The present interglacial represents a period of incision, recorded by several debris flow deposits that yield exposure ages ranging from ~9 ka to ~24 ka. All of these sedimentary landforms record a transition from aggradation to incision during MIS II. Coupled with the alluvial surfaces of the Chajnantor fans, the exposure ages determined as a part of this study support aggradation during glacial periods and incision during interglacial periods. These results suggest that climate, specifically precipitation, is the dominant control on alluvial fan formation along the western margin of the Chajnantor Plateau.

References

Adamiec G, Aitken MJ. 1998. Dose-rate conversion factors: new data: *Ancient TL* v. 16, p. 37–50.

Aitken MJ. 1985. *Thermoluminescence Dating*. London: Academic

Aitken MJ. 1998. *An Introduction to Optical Dating*. Oxford: Oxford University Press

Amundson, R., Dietrich, W., Bellugi, D., Ewing, S., Nishiizumi, K., Chong, G., Owen, J., Finkel, R., Heimsath, A., and Stewart, B., 2012. Geomorphologic evidence for the late Pliocene onset of hyperaridity in the Atacama Desert: *Geol. Soc. Am. Bull.* v. 124, p. 1048–1070.

Anderson, R. S., Repka, J. S., and Dick, G. S., 1996, Explicit treatment of inheritance in dating depositional surfaces using in situ ^{10}Be and ^{26}Al: *Geology* v. 24, p. 47-51.

Arriagada, C., Cobbold, P. R., Mpodozis, C., and Roperch, P., 2002. Cretaceous to Paleogene compressional tectonics during deposition of the Purilactis Group, Salar de Atacama, paper presented at Fifth International Symposium on Andean Geodynamics (ISAG), Inst. de Rech. pour le De´v., Toulouse, France.

Arriagada, C., Cobbold, P.R., and Roperch, P., 2006. Salar de Atacama basin: A record of compressional tectonics in the central Andes since the mid-Cretaceous: *Tectonics*, v. 25, TC1008, doi:10.1029/2004TC001770.

Baker, P.A., Rigsby, C.A., Seltzer, G.O., Fritz, S.C., Lowenstein, T.K., Bacher, N.P., and Veliz, C., 2001. Tropical climate changes at millennial and orbital timescales on the Bolivian Altiplano: *Nature* v. 409, p, 698–701.

Betancourt, J.L., Latorre,C., Rech, J.A., Quade, J., and Rylander, K.A., 2000. A 22,000-yr record of monsoonal precipitation from northern Chile's Atacama Desert: *Science* v. 289, p. 1546-1550.

Bierman, P., Fernandez, N., Sosa-Gonzales, V., Rood, D.H., and Massey, C., 2014. Cosmogenic 10-Be analysis of debris flow boulders and sediment from Brazil indicates long return times [Abstract]. *Geological Society of America Abstracts with Programs*, 46 (6).

Blackwelder, E., 1931. Pleistocene glaciation in the Sierra Nevada and Basin Ranges: *Geo. Soc. Am. Bull.* v. 42, p. 865-922.

Blisniuk, K., Oskin, M., Fletcher, K., Rockwell, T., and Sharp, W., 2012. Assessing the reliability of U-Series and ^{10}Be dating techniques on alluvial fans in the Anza Borrego Desert, California: *Quat. Geochronol.* v. 13, p. 26-41.

Bobst, Andrew L., Lowenstein, T. K., Jordan, T.E., Godfrey, L.V., Ku, T., and Luo, S., 2001, A 106ka paleoclimate record from drill core of the Salar de Atacama, northern Chile: *Paleogeography, Paleoclimatology, Paleoecology*, v. 173, p. 21-42.

Bull, W. B., and Schick, A. P. (1979). Impact of climatic changes in an arid watershed: Nahal Yael, southern Israel: *Quat. Res.*, v. 11, p. 153-171.

Bull, W.B., 1977. The alluvial-fan environment: *Prog. Phys. Geogr.*, v. 1, p. 222-270.

Burke, R.M. and Birkeland, P.W., 1979. Re-evaluation of multiparameter relative dating techniques and their application to the glacial sequence along the eastern escarpment of the Sierra Nevada, California: *Quat. Res.*, v. 11, no. I, p. 21-51.

Caviedes, C., 1973. A climatic profile of the north Chilean desert at latitude 20° south. In: *Coastal Deserts, Their Natural and Human Environments*. Amiran, D. H. K. , and Wilson, A.W. (Eds.),. The University of Arizona Press, Tucson, AZ, pp. 115-121.

Church M., and Ryder J.M., 1972. Paraglacial sedimentation: consideration of fluvial processes conditioned by glaciation. *Geological Society of America Bulletin*, v. 83, p. 3059-3072.

Church M., and Ryder J.M., 1989. Sedimentology and clast fabris analysis of subaerial debris flow facies in a glacially-influenced alluvial fan – a discussion: *Sedimentary Geology*, v. 65, p. 195-196.

Clark, J.D.A., 2005. Antiquity of aridity in the Chilean Atacama Desert: *Geomorphology*, v. 73, p. 101-144.

Colman, S. M., and Pierce, K. L., 1986. Glacial sequence near McCall, Idaho: Weathering rinds, soil development, morphology and other relative age criteria: *Quat. Res.*, v. 25, p. 25-42.

Desilets, D., and Zreda, M., 2003. Spatial and temporal distribution of secondary cosmic-ray nucleon intensities and applications to in situ cosmogenic dating: *Earth and Planetary Science Letters*, v. 206, p, 21–42.

de Silva, S.L., 1989. Geochronology and stratigraphy of the ignimbrites from 21°30'S to 23°30'S portion of the central Andes of northern Chile: *Journal of Volcanology and Geothermal Research*, v. 37, p. 93-131.

Díaz, F.P., Latorre, C., Maldonado, A., Quade, J., and Betancourt, J.L., 2012. Rodent middens reveal episodic, long distance plant colonizations across the hyperarid Atacama Desert over the last 34,000 years: *J. Biogeogr.*, v. 39, p. 510-525.

Dorn, R. I., 2009. The role of climate change in alluvial fan development, in *Geomorphology of Desert Environments*, edited by A. J. Parsons and A. D. Abrahams, pp. 593–615, Springer, Netherlands.

Dühnforth, M., Anderson, R.S., Ward, D.J., and Blum, A., 2012. Unsteady late Pleistocene incision of streams bounding the Colorado Front Range from measurements of meteoric and in situ 10Be: *Journal of Geophysical Research*, v. 117, F01023, doi:10.1029/2011JF002232.

Dunai, T.J., González López, G.A., and Juez-Larré, J., 2005. Oligocene–Miocene age of aridity in the Atacama Desert revealed by dating of erosion-sensitive landforms: *Geology*, v. 33, p. 321–324.

Dunai T. J.. 2000. Scaling factors for production rates of in-situ produced cosmogenic nuclides: a critical reevaluation: *Earth Planet Sci. Lett.*, v. 176, p. 157-169.

Enzel, Y., R. Amit, T. Grodek, A. Ayalon, J. Lekach, N. Porat, P. Bierman, J. D. Blum, and Y. Erel, 2012. Late Quaternary weathering, erosion, and deposition in Nahal Yael, Israel: An "impact of climatic change on an arid watershed"?: *Geol. Soc. Am. Bull.*, v. 124 (5–6), p. 705–722.

Evenstar, L.A., Hartley, A.J., Stuart, F.M., Mather, A.E., Rice, C.M., and Chong, G., 2009. Multiphase development of the Atacama planation surface recorded by cosmogenic ^{3}He ages: implications for uplift and Cenozoic climate change: *Geology* v. 37, p. 27–30.

Fairbanks, R.G., 1989. A 17,000 year glacio-eustatic sea level record: influence of glacial melting rates on the Younger Dryas event and deep ocean circulation: *Nature*, v. 342, p. 637–642.

Flint, S., Turner, P., Jolley, E., and Hartley, A.J., 1993. Extensional tectonics in convergent margin basin: An example from the Salar de Atacama, Chilean Andes: *Geol. Soc. Am. Bull.*, v. 105, p. 603-617.

Francis, P.W., McDonough, W.F., Hammill, M., O'Callaghan, L.J., and Thorpe, R.S., 1984. The Cerro Purico volcanic complex, North Chile: in *R.S. Harmon, B.A. Barriero (Eds.), Andean Magmatism-Chemical and Isotopic constraints*, Shiva Publishing, Orpington, U.K, p. 150–161

Frankel, K.L., Brantley, K.S., Dolan, J.F., Finkel, R.C., Klinger, R.E., Knott, J.R., Machette, M.N., Owen, L.A., Phillips, F.M., Slate, J.L., and Wenicke, B.P., 2007a. Cosmogenic ^{10}Be and ^{36}Cl geochronology of offset alluvial fans along the northern Death Valley fault zone: Implications for transient strain in the eastern California shear zone: *J. Geophys. Res. Solid Earth*, v. 112, B06407, doi:10.1029/2006JB004350

Gardeweg, P.M. and Ramirez C.F., 1987. The La Pacana Caldera and the Atana ignimbrite: A major ash-flow and resurgent caldera complex in the Andes of northern Chile: *Bull. Volcanol*., v. 49, p. 547-566.

Garreaud, R.D., and Aceituno, P., 2001. Interannual rainfall variability over the South American Altiplano: *J. of Climate*, v. 14, p. 2779-2789

Geyh, M.A., Grosjean, M., Nunez, L.A., and Schotterer, U., 1999. Radiocarbon reservoir effect and the timing of the late-Glacial/Early Holocene humid phase in the Atacama Desert (northern Chile): *Quat. Res.*, v. 52, p. 143-153.

Godfrey-Smith D.I, Huntley D.J, and Chen W.H., 1988. Optical dating studies of quartz and feldspar sediment extracts: *Quat. Sci. Rev.*, v. 7, p. 373–80.

González, G.L., Dunai, T., Carrizo, D., and Allmendinger, R., 2006. Young displacements on the Atacama Fault System, Northern Chile from field observations and cosmogenic ^{21}Ne concentrations: *Tectonics*, v. 25, TC3006, doi:10.1029/2005TC001846.

Gosse, John C., and Phillips, Fred M. 2001, Terrestrial in situ cosmogenic nuclides: theory and application: *Quat. Sci. Rev.*, v. 20, p. 1475-1560.

Grosjean, M., van Leeuwen, J.F.N., van der Knaap, W.O., Geuh, M.A., Amman, B., Tanner, W., Messerli, B., Nunez, L.A., Valero-Garcés, B.L., and Viet, H., 2001. A 22,000 14C year BP sediment and pollen record of climate change from Laguna Miscanti (23 °S), northern Chile: *Global and Planetary Change*, v. 28, p. 35–51.

Grosjean, M., Nunez, L., Cartajena, I., and Messerli, B., 1996. Mid-Holocene climate and cultural change in the Atacama Desert, northern Chile: *Quat. Res.*, v. 48, p. 239-246.

Guest, J. E., 1969. Upper Tertiary ignimbrites in the Andean Cordillera, a part of the Antofagasta province northern Chile: *Geo. Soc. Am. Bull.*, v. 80, p. 337-372.

Gunster, N. and Skowronek, A., 2001. Sediment–soil sequences in the Granada Basin as evidence for long- and short-term climatic changes during the Pliocene and Quaternary in the Western Mediterranean: *Quaternary International*, v.78, p. 17-32.

Guyodo, Y., Valet, J.-P., 1999. Global changes in intensity of the earth's magnetic field during the past 800 kyr: *Nature*, v. 399 (6733), p. 249–252.

Hall, S.R., Farber, D.L., Audin, L., Finkel, R.C., and Mériaux, A.-S., 2008. Geochronology of pediment surfaces in southern Peru: Implications for Quaternary deformation of the Andean forearc: *Tectonophysics*, v. 450, p. 186-205.

Hancock, G.S., Anderson, R.S., Chadwick, O.A., and Finkel, R.C., 1999. Dating fluvial terraces with ^{10}Be and ^{26}Al profiles: application of the Wind River, Wyoming: *Geomorphology*, v. 27, p. 41-60.

Hartley AJ, and Chong. G., 2002. Late Pliocene age for the Atacama Desert: implications for the desertification of western South America. *Geology*, v. 30, p. 43–46.

Hartley, A., Flint, S., Turner, P., and Jolley, E.J., 1992. Tectonic controls on the development of a semi-arid, alluvial basin as reflected in the stratigraphy of the Purilactis Group (Upper Cretaceous-Eocene), northern Chile: *Journal of South American Earth Sciences*, v. 5, No. 3-4, p. 275-296.

Hartley, AJ. & Mather, AE., Jolley, E., and Turner, P., 2005. 'Climatic controls on alluvial-fan activity, Coastal Cordillera, northern Chile' in *Geological Society, London, Special Publication, Harvey, A., Mather, AE. & Stokes, M. (eds.). Alluvial Fans: Geomorphology, Sedimentology, Dynamics.* Geological Society, London, Special Publication, v. 251, p. 95-115.

Harvey, A.M., Wigand, P.E., and Wells, S.G., 1999b. Response of alluvial fan systems to the late Pleistocene to Holocene climatic transition: contrasts between the margins of pluvial Lakes Lahontan and Mojave, Nevada and California, USA: *Catena*, v. 36, p. 255-281.

Haug, E.W., Kraal, E.R., Sewall, J.O., Dijk, M.V., and Chong Diaz, G., 2010. Climatic and geomorphic interactions on alluvial fans in the Atacama Desert, Chile: *Geomorphology*, v. 121, p. 184-196.

Hedrick, K., Owen, L.A., Rockwell, T.K., Meigs, A., Costa, C., Caffee, M.W., Masana, E., and Ahumada, E., 2013. Timing and nature of alluvial fan and strath terrace formation in the Eastern Precordillera of Argentina: *Quat. Sci. Rev.*, v. 80, p. 143-168.

Hoke, G.D., Isacks, B.L., Jordan, T.E., and Yu, J.S., 2004, Groundwater-sapping origin for the giant quebradas of northern Chile: *Geology*, v. 32, p. 605.

Houston, John, and Hartley, Adrian J. 2003, The Central Andean West-slope Rainshadow and its Potential contribution to the Origin of Hyper-aridity in the Atacama Desert: *Int. J. Climatol.*, v. 23, p. 1453-1464.

Houston, John. 2006, The great Atacama flood of 2001 and its implications for Andean hydrology: *Hydrol. Process.*, v. 20, p. 591-610.

Huntley D.J, Godfrey-Smith D.I, and Thewalt, M.L.W., 1985. Optical dating of sediments: *Nature*, v. 313, p. 105–107.

Hütt, G., Jaek, I., Tchonka, J., 1988. Optical dating: K-feldspars optical response stimulation spectra: *Quat. Res. Rev.*, v. 7, p. 381–385.

Irwin, R.P., Tooth, S., Craddock, R.A., Howard, A.D., and Baptista de Latour, A., 2014. Origin and development of theater-headed valleys in the Atacama Desert, northern Chile: Morphological analogs to martian valley networks: *Icarus*, v. 243, p. 296-310.

Ivy-Ochs, S, Kober, F, Alfimov, V, Kubik, P.W, and Synal, HA., 2007. Cosmogenic ^{10}Be, ^{21}Ne, and ^{36}Cl in sanidine and quartz from Chilean ignimbrites: *Nuclear Instruments and Methods in Physics Research*, v. B259, p. 588–594.

Jain, M. and Singhvi, A.K., 2001. Limits to depletion of blue-green light stimulated luminescence in feldspars: Implications for quartz dating: *Radiation Measurements*, v. 33, p. 883-892.

Jain, M., Choi, J.H., Thomas, P.J., 2008. The ultrafast OSL component in quartz: Origins and implications: *Radiation Measurements*, v. 43, p. 709-714.

Jolley, E.J., Turner, P., Williams, G.D., Hartley, A.J., and Flint, S., 1990. Sedimentological response of an alluvial system to Neogene thrust tectonics, Atacama Desert, northern Chile: *J. Geol. Soc. London*, v. 147, p. 769-784.

Jordan, T.E., Mpodozis, C., Munoz, N., Blanco, N., Pananont, P., and Gardeweg, M., 2007. Cenozoic subsurface stratigraphy and structure of the Salar de Atacama Basin, northern Chile: *Journal of South American Earth Sciences*, v. 23, p. 122-146.

Jungers M.C, Heimsath, A.M., Amundson, R., Balco, G., Shuster, D., and Chong, G., 2013. Active erosion-deposition cycles in the hyperarid Atacama Desert of Northern Chile: *Earth Planet Sci. Lett.*, v. 371-372, p. 125-133.

Korschinek, G., Bergmaier, A., Faestermann, T., Gerstmann, U.C., Knie, K., Rugel, G., Wallner, A., Dillmann, I., Dollinger, G., Liese von Gostomski, Ch., Kossert, K., Maiti, M., Poutivtsev, M. and Remmert. A., 2010. A new value for the half-life of ^{10}Be by heavy-ion elastic recoil detection and liquid scintillation counting. *Nuclear Instruments and Methods in Physics Research B*, v. 268, p. 187-191.

Lal, D., 1991. Cosmic ray labeling of erosion surfaces: in situ nuclide production rates and erosion models: *Earth and Planetary Science Letters*, v. 104, p, 424–439.

Latorre, C., Betancourt, J.L., Rech, J.A., Quade, J., Holmgren, C., Placzek, C., Maldonado, A.J.C., Vuiile, M., and Rylander, K., 2005. Late Quaternary history of the Atacama Desert. In: *Smith, M., Hesse, P. (Eds.), 23°S: the Archeology and Environmental History of the Southern Deserts*. National Museum of Australia Press, Canberra, Australia, pp. 73–90.

Latorre, C., Betancourt, J.L., Rylander, K.A., and Quade, J., 2002.Vegetation invasions into Absolute Desert: A 45,000-yr rodent midden record from the Calama-Salar de Atacama Basins, northern Chile (22-24°S): *Geol. Soc. Am. Bull.*, v. 114, p. 349-366.

Latorre, C., Betancourt, J.L., Rylander, K.A., Quade, J., and Matthei, O., 2003. A 13.5-kyr vegetation history from the arid prepuna of northern Chile (22–23°S): *Palaeogeography, Palaeoclimatology, Palaeoecology*, v. 194, p. 223–246.

Lenters, J.D., and Cook, K.H., 1997. On the origin of the Bolivian High and related circulation features of the South American climate: *Journal of the Atmospheric Sciences*, v. 54, p. 656-677.

Licciardi, J.M., Denoncourt, C.L., and Finkel, R.C., 2008. Cosmogenic ^{36}Cl production rates from Ca spallation in Iceland: *Earth Planet Sci. Lett.*, v. 267, p. 365-377.

Lifton, N., Sato, T., and Dunai, T.J., 2014. Scaling *in situ* cosmogenic nuclide production rates using analytical approximations to atmospheric cosmic-ray fluxes: *Earth Planet Sci. Lett.*, v. 386, p. 149-160.

Lindsay, J.M., de Silva, S., Trumbull, R., Emmermann, R., and Wemmer, K., 2000. La Pacana caldera, N. Chile: A re-evaluation of the stratigraphy and volcanology of one of the world's largest resurgent calderas: *Journal of Volcanology and Geothermal Research*, v. 106, p. 145-173.

Lisiecki, L. E., and Raymo, M. E., 2005, A Pliocene-Pleistocene stack of 57 globally distributed benthic δ^{18}O records: *Paleoceanography*, v. 20, PA1003, doi:10.1029/2004PA001071.

Lowell, T. V., 1995, The application of radiocarbon age estimates to the dating of glacial sequences: An example from the Miami sublobe, Ohio, U.S.A: *Quat. Sci. Rev.*, v. 14, p. 85-99.

Lowenstein, T.K., Hein, M.C., Bobst, A.L., Jordan, T.E., Ku, T.L., and Luo, S., 2003. An assessment of stratigraphic completeness in climate-sensitive closed-basin lake sediments: Salar de Atacama, Chile: *Journal of Sedimentary Research*, v. 73, p. 91-104.

Machette, M.N., Slate, J.L., and Phillips, F.M., 2008. Terrestrial Cosmogenic-nuclide Dating of Alluvial Fans in Death Valley, California. In: *USGS Professional Paper* 1755.

Maldonado, A., Betancourt, J.L., Latorre, C., and Villagran, C., 2005. Pollen analyses from a 50,000-yr rodent midden series in the southern Atacama Desert (25°30′S): *Journal of Quaternary Science*, v. 20, p. 493–507.

Marinovic,N., and Lahsen, A.,1984. Geología de la Hoja Calama, Regíon de Antofagasta. Carta Geologíca de Chile, Escala 1:250.000,58. Servicio Nacional de Geología y Minería, Santiago de Chile, p. 140.

Mather, AE., and Hartley, AJ., 2005. 'Flow events on a hyper-arid alluvial fan: Quebrada Tambores, Salar de Atacama, northern Chile'. in *Geological Society, London, Special Publication, Harvey, A., Mather, AE. & Stokes, M. (eds.). Alluvial Fans: Geomorphology, Sedimentology, Dynamics.* Geological Society, London, Special Publication, v. 251, p. 9-29.

Matmon, A., Nichols, K., and Finkel, R., 2006. Isotopic insights into smoothening of abandoned fan surfaces, Southern California: *Quat. Res.*, v. 66, p. 109-118.

McFadden, L.D., Ritter, J.B., and Wells, S.G., 1989. Use of multiparameter relative-age methods for age estimation and correlation of alluvial fan surfaces on a desert piedmont, Eastern Mojave Desert, California: *Quat. Res.*, v. 32, p. 276-290.

McPhillips, D., Bierman, P.R., Crocker, T., and Rood, D.H., 2013. Landscape response to Pleistocene-Holocene precipitation change in the Western Cordillera, Peru: ^{10}Be concentrations in modern sediments and terrace fills: *Journal of Geophysical Research: Earth Surface*, v. 118, p. 2488-2499.

Mejdahl V. 1979. Thermoluminescence dating: beta-dose attenuation in quartz grains: *Archaeometry*, v. 21, p. 61–72.

Merchel, S., Braucher, R., Alfimov, V., Bichler, M., Bourlés, D.L., and Reitner, J.M., 2013. The potential of historic rock avalanche and man-made structures as chlorine-36 production rate calibration sites: *Quat. Geol.,* v. 18, p. 54-62.

Mpodozis, C., Arriagada, C., Basso, M., Roperch, P., Cobbold, P., and Reich, M., 2005. Late Mesozoic to Paleogene stratigraphy of the Salar de Atacama basin, Antofagasta, northern Chile: Implications for the tectonic evolution of the central Andes: *Tectonophysics*, v. 399, p. 125 – 154.

Mpodozis, C., Arriagada, C., Basso, M., Roperch, P., Cobbold, P., and Reich, M., Late Mesozoic to Paleogene stratigraphy of the Salar de Atacama Basin, Antofagasta, Northern Chile: Implications for the tectonic evolution of the Central Andes: *Tectonophysics*, v. 399, p. 125-154.

Muñoz, N., Charrier, R., and Reutter, K., 1997. Evolución de la cuenca Salar de Atacama: Inversión tectónica y relleno de una cuenca de antepaís de retroarco: *In Congreso Geológico Chileno, No. 8, Actas,* v. 1, p. 195-199. Antofagasta.

Murray A.S, and Wintle A.G., 2000. Luminescence dating of quartz using an improved single-aliquot regenerative-dose protocol: *Radiat. Meas.*, v. 32, p. 57–73.

Nalpas, T., Dabard, M.-P., Ruffet, G., Vernon, A., Mpodozis, C., Loi, A., and Hérail, G., 2008. Sedimentation and preservation of the Miocene Atacama Gravels in the Perdernales-Chañaral Area, Northern Chile: Climatic or tectonic control?: *Tectonophysics*, v. 459, p. 161-173.

National Research Council, 2010. Landscapes on the Edge: New Horizons for Research on Earth's Surface, pp. 180, The National Academies Press, Washington, D.C.

Nishiizumi, K., Caffee, M.W., Finkel, R.C., Brimhall, G., and Mote, T. 2005, Remnants of a fossil alluvial fan landscape of Miocene age in the Atacama Desert of northern Chile using cosmogenic nuclide exposure age dating: *Earth Planet Sci. Lett.*, v. 237, p. 499-507.

Ohno, M., and Hamano, Y., 1992. Geomagnetic poles over the past 10,000 years: *Geophysical Research Letters*, v. 19 (16), p. 1715–1718.

Owen, L.A., Frankel, K.L., Knott, J.R., Reynhout, S., Finkel, R.C., Dolan, J.F., and Lee, J., 2011. Beryllium-10 terrestrial cosmogenic nuclide surface exposure dating of Quaternary landforms in Death Valley: *Geomorphology*, v. 125, p. 541-557.

Owen, L.A., Clemmens, S.J., Finkel, R.C., Gray, H., 2014. Late Quaternary alluvial fans at the eastern end of the San Bernardino Mountains, Southern California: *Quat. Res. Rev.*, v. 87, p. 114-134.

Pananont, P., Mpodozis, C., Blanco, N., Jordan, T. E., and Brown, L. D., 2004. Cenozoic evolution of the northwestern Salar de Atacama Basin, northern Chile: *Tectonics*, v. 23, TC6007, doi:10.1029/2003TC001595.

Phillips, F.M., Zreda, M.G., Flinsch, M.R., Elmore, D., and Sharma, P., 1996. A reevaluation of cosmogenic ^{36}Cl production rates in terrestrial rocks: *Geophysical Research Letters*, v. 23 (9), p. 949–952.

Placzek, C.J., Granger, D.E., Matmon, A., Quade, J., and Ryb, U., .2014. Geomorphic process rates in the central Atacama Desert, Chile: insights from cosmogenic nuclides and implications for the onset of hyperaridity: *American Journal of Science*, v. 314, p. 1462-1512.

Placzek, C., Quade, J., and Patchett, P.J., 2006. Geochronology and stratigraphy of Late Pleistocene lake cycles on the Southern Bolivian Altiplano: implications for causes of tropical climate change. In: *Geol. Soc. Am. Bull.*, v. 118 (5), p. 515–532.

Placzek, C.J., Quade, J., and Patchett P.J., 2013. A 130 ka reconstruction of rainfall from the Bolivian Altiplano: *Earth Planet Sci. Lett.*, v. 363, p. 97-108

Placzek C.J., Quade, J., Betancourt, J.L., Patchett, P.J., Rech, J.A., Latorre, C., Matmon, A., Holmgren, C. and English, N.B., 2009. Climate in the dry central Andes over geologic, millennial, and interannual timescales: *Annals of the Missouri Botanical Garden*, v. 96 (3), p. 386-397.

Placzek, C.J., Matmon, A., Granger, D.E., Quade, J., and Niedermann, S., 2010. Evidence for active landscape evolution in the hyperarid Atacama from multiple terrestrial cosmogenic nuclides: *Earth Planet Sci. Lett.*, v. 295, p. 12–20.

Perkins, J.P., Finnegan, N.J., and de Silva, S.L., 2015. Amplification of bedrock canyon incision by wind: *Nature Geoscience*, v. 8, p. 305-310.

Porat, N., 2006. Use of magnetic separation for purifying quartz for luminescence dating: *Ancient TL*, v. 24, p. 33-36.

Prescott J.R, and Hutton, J.T. 1994. Cosmic ray contributions to dose rates for luminescence and ESR dating: large depths and long-term time variations: *Radiat. Meas.*, v. 23, p. 497–500.

Quade, J., Rech, J.A., Betancourt, J.L., Latorre, C., Quade, B., Rylander, K.A., and Fisher, T., 2008. Paleowetlands and regional climate change in the central Atacama Desert, northern Chile: *Quat. Res.*, v. 69, p. 343–360.

Ramírez, C.F., and Gardeweg, M., 1982, Hoja Toconau, Región de Antofagasta: Carta Geológica de Chile, 1:250,000: Servicio Nacional de Geología y Minería de Chile, Boletin v. 54

Raymo, M. E., Oppo, D.W., and Curry, W., 1997. The mid Pleistocene climate transition: A deep sea carbon isotopic perspective: *Paleoceanography*, v. 12(4), p. 546-559.

Rech, J.A., Currie, B.S., Michalski, G., and Cowan, A.M., 2006. Neogene climate change and uplift in the Atacama Desert, Chile: *Geology*, v. 34, p. 761–764.

Rech, J.A., Quade, J., and Betancourt, J.L., 2002, Late Quaternary paleohydrology of the central Atacama Desert (lat. 22-24° S), Chile: *Geo. Soc. Am. Bull.*, v. 114, p, 334.

Rech, J.A., Pigati, J.S., Quade, J., and Betancourt, J.L., 2003. Re-evaluation of mid-Holocene deposits at Quebrada Purica, northern Chile: *Palaeogeography, Palaeoclimatology, Palaeoecology*, v. 194, p. 207-222.

Rhodes, E.J, Bronk-Ramsey, C., Outram, Z., Batt, C., Willis, L., et al. 2003. Bayesian methods applied to the interpretation of multiple OSL dates: high precision sediment age estimates from Old Scatness Broch excavations, Shetland Isles: *Quat. Sci. Rev.*, v. 22, p.1231–1244

Rhodes, E.J. 2011. Optically Stimulated Luminescence Dating of Sediments over the Past 200,000 Years: *Annu. Rev. Earth Planet Sci.*, v. 39, p. 461-288.

Ritter, J.B., Miller, J.R., Enzel, Y., and Wells, S.G., 1995. Reconciling the roles of tectonism and climate in Quaternary alluvial fan evolution: *Geology*, v. 23, p. 245-248.

Ritter, J.R., Miller, J.R., and Husek-Wulforst, J., 2000. Environmental controls on alluvial fan evolution in Buena Vista Valley, North Central Nevada: *Geomorphology*, v. 36, p. 63-87.

Salisbury, M.J., Jicha, B.R., de Silva, S.L., Singer, B.L., Jiménez, N.C., and Ort, M.H., 2010. $^{40}Ar/^{39}Ar$ chronostratigraphy of Altiplano-Puna volcanic complex ignimbrites reveals the development of a major magmatic province: *Geol. Soc. Am. Bull.*, v. 123, p. 821-840.

Sarıkaya, M.A., Yıldırım, C., and Çiner, A., 2015. Late Quaternary alluvial fans of Emli Valley in the Ecemiş Fault Zone, south central Turkey: Insights from cosmogenic nuclides: *Geomorphology*, v. 228, p. 512-525.

Schimmelpfennig, I., Benedetti, L., Finkel, R., Pik, R., Blard, P.H., Bourlés, D., Burnard, P., and Williams, A., 2009. Sources of *in situ* ^{36}Cl in Basaltic rocks. Implications for calibration of production rates: *Quat. Geol.*, v. 4, p. 441-461.

Schimmelpfennig, I., Benedetti, L., Garreta, V., Pik, R., Blard, P.H., Burnard, P., Bourlés, D., Finkel, R., Ammon, K., and Dunai, T., 2011. Calibration of cosmogenic ^{36}Cl production rates from Ca and K spallation in lava flows from Mt. Etna (38N, Italy) and Payun Matru (36S, Argentina): *Geochimica et Cosmochimica Acta.*, v. 75, p. 2611-2632.

Schmitt, A.K., de Silva, S.L., Trumbull, R.B., and Emmermann, R. 2001, Magma evolution in the Purico ignimbrite complex, northern Chile: evidence for zoning of a dacitic magma by injection of rhyolitic melts following mafic recharge: *Contrib Mineral Petrol*, v. 140, p. 680-700.

Shackleton, N.J., 2000. The 100,000-year ice-age cycle identified and found to lag temperature, carbon dioxide, and orbital eccentricity: *Science*, v. 289 (5486), p. 1897–1902.

Sharp, R.P., and Birman, J.H., 1963. Additions to classical sequence stratigraphy of Pleistocene glaciations, Sierra Nevada, California: *Geol. Soc. Am. Bull.*, v. 74, p. 1079-1086.

Smith, B.W., Aitken, M.J., Rhodes, E.J., Robinson, P.D. and Geldard, D.M., 1986. Optical Dating: Methodological Aspects: *Radiation Protection Dosimetry*, v. 17, p. 229-233.

Sparks, R.S.J., Gardeweg, M.C., Calder, E.S., and Matthews, S.J., 1997. Erosion by pyroclastic flows on Lascar Volcano, Chile: *Bull. Volcanol.*, v. 58, p. 557-565.

Stone, J.O., 2000, Air pressure and cosmogenic isotope production: *Journal of Geophysical Research*, v. 105, p. 23753-23759.

Stone, J.O., Fifield, L.K., Allan, G.L., and Cresswell, R.G., 1996. Cosmogenic chlorine-36 production from calcium spallation: *Geochimica et Cosmochimica Acta.*, v. 60, p. 679-692.

Stone, J.O., Evans, J.M., Fifield, L.K., Allan, G.L., and Cresswell, R.G., 1997. Cosmogenic chlorine-36 production in calcite by muons: *Geochimica et Cosmochimica Acta.*, v. 62, p. 433-454.

Ventra, D. and Nichols, G.J., 2014. Autogenic dynamics of alluvial fans in endoheric basins: Outcrop examples and stratigraphic significance: *Sedimentology*, v. 61, p. 767-791.

Viseras, C., Calvache, M.L., Soma, J.M. & Fernandez, J. 2003. Differential Features of Alluvial Fans Controlled by Tectonic or Eustatic Accommodation Space. Examples From The Betic Cordillera, Spain: *Geomorphology*, v. 50, p. 181-202.

Vuille, M., 1999. Atmospheric circulation anomalies over the Bolivian Altiplano during dry and wet periods and extreme phases of the Southern Oscillation: *Int. J. Climatol.*, v.19, p. 1579-1600.

Ward, D.J., Cesta, J.M., Galewsky, J., and Sagredo, E., (in Review). Late Pleistocene glaciations of the arid subtropical Andes and new results from the Chajnantor Plateau, northern Chile: *Quat. Sci. Rev*.

Wells, S. G. 1977. Geomorphic controls of alluvial fan deposition in the Sonoran Desert, southwestern Arizona. In "*Geomorphology of Arid Regions*" (D. O. Doehring, Ed.). Proceedings Volume of the Eighth Annual Geomorphology Symposium at State University of New York at Binghamton, pp. 27-50.

Yang, S., Odah, H., and Shaw, J., 2000. Variations in the geomagnetic dipole moment over the last 12000 years: *Geophysical Journal International*, v. 140 (1), p. 158–162.

Zreda, M.G., Phillips, F.M., Elmore, D., Kubik, P.W., Sharma, P., and Dorn, R.I., 1991. Cosmogenic chlorine-36 production rates in terrestrial rocks: *Earth Planet Sci. Lett.*, v. 105, p. 94-109.

Zweck, C., Zreda, M., Anderson, K., and Bradley, E., 2012. The theoretical basis of ACE, an Age Calculation Engine for cosmogenic nuclides: *Chemical Geology*, v. 291, p. 199-205.

APPENDIX A: Relative-age Weathering Parameters

Alluvial Fan Surface ID#: Qs2A1				Date: 7/15/2014	
Comments: Includes Cobbles w/ Intermediate Axis ≥ 1.5 cm. Declination: 5°2' W.					
Cobble ID#	**Inter. Axis (cm)**	**Angularity**	**Lithology**	**Ventifaction**	**Pitted**
1	4.5	SR	A	Y	N
2	2.6	SR	A	Y	Y
3	3.3	SR	A	Y	N
4	5.6	SR	A	Y	Y
5	3.5	SR	A	Y	Y
6	4.8	SR	A	Y	Y
7	4.4	SA	A	Y	N
8	2.1	SR	A	N	Y
9	4.5	SA	A	Y	N
10	6.0	SA	A	Y	N
11	6.1	SR	A	N	N
12	2.5	R	A	Y	N
13	4.5	R	A	Y	Y
14	4.0	R	A	Y	Y
15	5.2	SR	A	Y	N
16	3.8	SR	A	Y	Y
17	4.4	SA	A	Y	Y
18	6.4	R	A	Y	Y
19	6.7	SR	A	Y	N
20	3.9	SR	A	Y	Y
21	2.5	SA	A	Y	N
22	3.9	SA	A	Y	Y
23	4.0	SA	A	Y	N
24	8.4	SR	A	Y	N
25	2.8	R	A	Y	Y
26	3.3	SR	A	N	N
27	3.0	SA	A	N	Y
28	2.7	R	A	Y	Y
29	4.5	SR	A	Y	N
30	3.2	SA	A	Y	N
31	2.4	A	A	N	N
32	5.8	SR	A	Y	Y
33	4.4	SR	A	Y	Y
34	2.2	A	A	Y	N
35	7.6	SA	A	Y	Y
36	6.9	SR	A	N	Y
37	2.0	SR	A	Y	Y
38	3.5	SA	A	Y	N
39	8.0	SR	A	Y	Y
40	2.4	SR	A	N	Y
41	2.9	A	I	Y	N
42	2.6	SR	A	Y	Y
43	2.5	SR	A	Y	Y
44	2.6	SR	A	Y	Y
45	2.4	SA	A	N	N
46	2.5	R	A	Y	N
47	4.4	SA	A	N	N
48	2.5	R	A	Y	Y
49	4.5	SR	A	Y	Y
50	3.5	SR	A	Y	Y
51	3.2	A	I	Y	N
52	3.2	SA	A	Y	Y
53	3.1	SA	A	N	N
54	3.8	SR	A	Y	N
55	5.4	SR	A	Y	Y
56	7.9	SR	A	Y	Y
57	3.2	SR	I	Y	N
58	3.8	SR	A	Y	Y
59	3.5	SR	A	Y	Y
60	3.3	SA	A	N	N
61	3.4	SA	A	Y	Y
62	5.4	SR	A	Y	N
63	6.1	SA	A	Y	Y
64	4.4	A	I	Y	Y
65	2.8	SR	A	Y	Y
66	8.0	SA	A	Y	N
67	3.4	SA	A	N	N
68	3.8	SA	A	Y	Y
69	4.3	SR	A	Y	Y
70	3.0	SR	A	N	Y
71	3.2	SR	A	Y	Y
72	2.7	SR	A	Y	N
73	2.5	SA	A	N	Y
74	3.7	SA	A	Y	Y
75	7.7	SR	A	Y	Y
76	2.2	SR	A	N	Y
77	7.3	SR	A	Y	Y
78	3.8	SA	A	N	N
79	3.6	SA	A	Y	Y
80	2.9	SA	I	Y	N
81	5.2	A	I	Y	N
82	3.5	SA	A	Y	Y
83	2.7	SR	A	N	Y
84	3.0	R	A	Y	Y
85	2.8	SR	A	Y	Y
86	3.7	SA	A	Y	Y
87	2.9	SR	A	N	Y
88	2.7	SR	A	Y	Y
89	2.0	SA	A	N	N
90	6.7	R	A	Y	Y
91	4.6	SA	A	N	N
92	4.5	SA	A	Y	Y
93	3.0	SA	A	N	N
94	3.4	SR	A	Y	Y
95	5.4	R	A	Y	Y
96	7.4	SR	A	N	Y
97	2.3	R	A	Y	Y
98	8.2	SA	A	N	N
99	3.0	SR	A	Y	Y
100	3.8	SR	A	Y	Y

Angularity- R: Rounded, SR: Subrounded, SA: Subangular, A: Angular.
Lithology- A: Andesite, I: Ignimbrite.
Ventifaction/Pitting- Y: Yes, N: No.

Alluvial Fan Surface ID#: Qs2A2				Date: 7/09/2014	
Comments: Includes Cobbles w/ Intermediate Axis ≥ 1.5 cm. Declination: 5°2' W.					
Cobble ID#	**Inter. Axis (cm)**	**Angularity**	**Lithology**	**Ventifaction**	**Pitted**
1	1.5	SA	A	N	N
2	1.8	R	A	N	N
3	1.5	A	A	N	N
4	2.7	SA	A	N	N
5	2.0	A	A	N	N
6	2.5	A	A	N	N
7	6.5	R	A	N	N
8	4.4	SR	A	N	N
9	3.7	A	A	Y	N
10	1.8	A	A	N	N
11	2.2	SA	A	N	N
12	1.5	A	A	N	N
13	1.6	SA	A	N	N
14	4.0	SA	A	N	N
15	3.8	A	A	N	Y
16	2.4	A	A	N	N
17	5.0	SR	A	N	N
18	1.7	A	A	N	N
19	6.0	R	A	Y	N
20	3.5	SA	A	N	N
21	4.0	SR	A	N	N
22	3.9	SR	A	N	N
23	2.0	SR	A	N	N
24	1.6	SR	A	N	N
25	1.5	SR	A	N	N
26	3.2	SA	A	N	N
27	2.0	SR	A	N	N
28	2.5	SR	A	N	N
29	3.5	SR	A	N	N
30	2.2	SR	A	N	N
31	3.5	SR	A	N	N
32	2.8	A	A	N	N
33	1.7	SA	A	N	N
34	2.0	SA	A	Y	N
35	5.0	SR	A	N	N
36	1.7	A	A	N	N
37	1.5	SR	A	N	N
38	3.5	A	A	N	N
39	1.5	SR	A	N	N
40	1.6	SR	A	N	N
41	1.5	SR	A	N	N
42	8.6	R	A	Y	N
43	1.5	SR	A	N	N
44	4.5	R	A	N	N
45	2.5	SR	A	N	N
46	3.3	SR	A	N	N
47	1.5	SR	A	N	N
48	3.8	SR	A	N	N
49	1.5	SA	A	N	N
50	3.0	SA	A	N	N
51	1.5	SR	A	N	N
52	3.4	A	A	N	N
53	2.6	R	A	N	N
54	2.0	A	A	N	Y
55	2.3	SR	A	N	N
56	3.2	SR	A	N	N
57	4.0	SR	A	N	Y
58	1.4	SA	A	N	N
59	2.1	SA	A	N	N
60	1.9	SA	A	N	N
61	4.0	SA	A	N	N
62	5.1	SR	A	Y	N
63	3.6	SA	A	N	N
64	1.7	SA	A	N	N
65	2.3	SR	A	N	N
66	2.1	SR	A	N	N
67	3.4	SR	A	N	N
68	4.9	SR	A	N	N
69	2.7	R	A	N	Y
70	1.9	SR	A	N	N
71	2.0	SA	A	N	N
72	2.4	SR	A	N	Y
73	2.0	SA	A	N	Y
74	2.0	SA	A	N	Y
75	2.0	SA	A	N	N
76	2.8	A	A	N	N
77	5.0	R	A	N	Y
78	2.9	SA	A	N	N
79	3.5	SR	A	N	Y
80	4.1	A	A	N	N
81	3.0	SR	A	N	N
82	1.7	SR	A	N	N
83	1.5	SA	A	N	N
84	3.4	SA	A	N	N
85	1.5	SR	A	N	N
86	2.3	SR	A	N	N
87	3.0	R	A	Y	N
88	3.4	SR	A	N	N
89	3.5	SR	A	N	N
90	3.0	A	A	Y	N
91	1.5	SR	A	N	N
92	4.5	SR	A	N	Y
93	3.6	A	A	N	N
94	1.5	SA	A	N	N
95	2.0	SA	A	N	N
96	2.0	SR	A	N	N
97	1.7	SA	A	N	N
98	2.5	SA	A	N	N
99	3.0	SR	A	N	N
100	1.5	SA	A	N	Y

Angularity- R: Rounded, SR: Subrounded, SA: Subangular, A: Angular.
Lithology- A: Andesite, I: Ignimbrite.
Ventifaction/Pitting- Y: Yes, N: No.

Alluvial Fan Surface ID#: Qs2A3				Date: 7/15/2014	
Comments: Includes Cobbles w/ Intermediate Axis ≥ 1.5 cm. Declination: 5°2' W.					
Cobble ID#	**Inter. Axis (cm)**	**Angularity**	**Lithology**	**Ventifaction**	**Pitted**
1	3.4	R	I	N	Y
2	2.7	SA	A	N	Y
3	7.3	SR	A	N	Y
4	5.0	SA	A	Y	Y
5	6.3	SA	A	Y	Y
6	9.0	R	A	Y	Y
7	5.2	SR	A	N	Y
8	3.1	SA	A	N	N
9	5.1	SR	I	N	N
10	3.0	SR	A	N	N
11	2.3	A	A	Y	Y
12	4.5	R	I	Y	Y
13	6.3	R	A	N	Y
14	2.6	SA	A	N	Y
15	5.8	SA	A	N	N
16	10.2	A	I	N	N
17	6.5	R	A	Y	Y
18	4.6	SR	A	Y	Y
19	5.8	R	I	Y	Y
20	10.9	SR	A	Y	N
21	8.0	SR	A	Y	N
22	9.8	R	A	N	Y
23	4.4	SR	A	N	N
24	5.4	SR	A	N	Y
25	4.9	A	A	N	N
26	9.7	SA	A	Y	N
27	12.8	A	A	N	N
28	4.9	SA	A	N	Y
29	11.4	R	A	Y	N
30	8.7	R	A	N	Y
31	11.3	A	I	Y	N
32	4.0	SR	A	N	Y
33	4.2	SR	I	Y	N
34	8.8	SA	A	Y	N
35	10.4	R	A	Y	Y
36	7.2	SA	A	Y	N
37	6.6	SA	A	N	N
38	12.3	SA	A	Y	N
39	15.6	SR	A	N	N
40	6.4	SA	A	Y	Y
41	7.3	R	A	N	Y
42	9.0	SA	A	Y	N
43	3.9	SA	A	N	N
44	4.5	SR	A	Y	Y
45	10.0	SR	A	N	N
46	4.1	SA	A	N	N
47	4.2	SA	A	Y	Y
48	6.8	SA	A	N	N
49	9.2	SA	A	Y	Y
50	4.0	SA	A	N	N
51	4.1	SR	A	Y	N
52	9.2	SR	A	N	Y
53	5.9	R	A	N	Y
54	3.1	SR	A	N	N
55	6.8	SA	A	N	N
56	4.6	R	I	Y	N
57	1.9	SA	A	Y	Y
58	6.7	R	I	Y	N
59	4.6	SA	A	N	N
60	6.3	SA	A	Y	N
61	13.5	SR	A	N	Y
62	7.3	A	A	Y	N
63	10.0	SR	A	N	Y
64	4.5	SA	A	N	N
65	5.3	A	A	N	N
66	5.4	SR	A	N	Y
67	6.9	SR	I	Y	N
68	15.3	SA	A	N	N
69	8.0	R	A	N	Y
70	6.4	R	A	N	N
71	6.2	SR	A	N	Y
72	7.7	SA	A	N	N
73	7.5	R	A	N	N
74	15.1	SR	A	Y	N
75	4.7	SA	A	N	N
76	4.5	SR	A	N	Y
77	2.8	R	A	N	N
78	2.6	SR	A	N	Y
79	4.7	A	A	Y	N
80	3.5	SR	A	N	Y
81	3.5	A	A	N	N
82	4.0	A	A	N	Y
83	2.7	A	A	N	N
84	6.4	SA	A	N	Y
85	2.4	SA	A	Y	N
86	5.0	SR	A	N	Y
87	5.3	R	A	N	Y
88	3.0	SA	A	N	Y
89	3.3	SA	A	Y	Y
90	2.9	SR	A	N	Y
91	103.0	R	A	Y	N
92	2.3	R	I	Y	N
93	3.9	A	A	Y	Y
94	3.9	SA	A	N	Y
95	8.5	SR	A	N	Y
96	5.1	SA	A	N	Y
97	10.5	SR	A	N	Y
98	4.6	SR	A	Y	Y
99	7.5	R	A	N	Y
100	6.9	SR	A	N	Y

Angularity- R: Rounded, SR: Subrounded, SA: Subangular, A: Angular.
Lithology- A: Andesite, I: Ignimbrite.
Ventifaction/Pitting- Y: Yes, N: No.

Alluvial Fan Surface ID#: Qs2A4				Date: 7/15/2014	
Comments: Includes Cobbles w/ Intermediate Axis ≥ 1.5 cm. Declination: 5°2' W.					
Cobble ID#	**Inter. Axis (cm)**	**Angularity**	**Lithology**	**Ventifaction**	**Pitted**
1	3.5	SA	A	N	Y
2	3.1	SR	I	N	Y
3	4.9	SA	A	N	N
4	6.1	SA	A	N	N
5	6.4	SA	A	N	Y
6	3.4	R	A	N	Y
7	4.5	SR	A	N	Y
8	7.0	SR	A	N	Y
9	6.3	R	I	Y	N
10	4.3	R	A	Y	N
11	5.2	SR	A	N	Y
12	4.2	R	A	Y	Y
13	3.8	SR	I	Y	N
14	2.6	R	A	N	Y
15	6.6	SR	A	N	Y
16	3.8	SA	A	N	Y
17	3.3	SR	A	Y	N
18	3.4	SR	A	N	Y
19	4.1	SR	A	N	Y
20	4.2	R	A	N	Y
21	2.7	R	A	N	Y
22	12.9	R	I	Y	N
23	3.6	SA	A	N	Y
24	7.2	R	A	N	Y
25	4.4	SR	A	N	Y
26	4.9	R	A	Y	Y
27	4.7	R	A	N	Y
28	2.9	SA	A	N	N
29	4.1	SR	A	N	Y
30	4.2	SR	I	N	N
31	4.1	SR	A	N	Y
32	4.3	SA	A	N	N
33	2.6	SR	A	N	Y
34	2.9	SR	A	N	Y
35	4.3	SA	A	Y	Y
36	3.4	SR	A	N	Y
37	3.5	SA	A	Y	N
38	2.4	A	A	Y	N
39	6.1	SA	A	N	Y
40	4.6	R	I	Y	N
41	3.9	R	A	N	Y
42	4.6	SR	A	N	Y
43	5.1	R	A	N	Y
44	6.1	R	A	N	Y
45	2.3	SR	A	N	Y
46	5.5	SR	A	Y	Y
47	4.3	R	A	N	Y
48	3.4	SR	A	N	Y
49	5.5	SA	A	Y	N
50	2.5	SR	A	N	N
51	5.2	SA	A	N	Y
52	4.1	SA	A	N	Y
53	4.9	R	A	N	Y
54	3.9	SR	A	N	N
55	4.3	SR	A	N	Y
56	3.7	SA	A	N	N
57	4.7	SR	A	Y	Y
58	3.0	SA	A	N	Y
59	3.9	SA	A	N	Y
60	3.6	SR	A	N	N
61	6.9	SR	A	Y	N
62	9.1	SA	A	N	N
63	5.6	A	A	Y	N
64	6.3	SR	A	Y	Y
65	4.9	SA	A	Y	N
66	2.9	SR	A	N	Y
67	4.8	SR	A	Y	Y
68	4.9	R	A	N	Y
69	5.1	SR	A	N	Y
70	6.5	R	A	N	Y
71	4.9	R	A	N	Y
72	5.0	A	A	N	N
73	3.6	A	A	N	N
74	9.7	A	A	N	N
75	3.6	R	A	Y	N
76	3.7	SA	A	N	Y
77	3.9	SA	A	N	N
78	4.6	SA	A	Y	Y
79	4.5	SR	I	N	N
80	4.7	SA	A	Y	N
81	6.6	SR	A	Y	N
82	3.8	SA	A	Y	Y
83	6.5	SR	A	Y	N
84	3.4	SA	A	N	Y
85	4.6	R	I	N	N
86	4.7	SA	A	N	Y
87	3.6	SR	A	N	Y
88	7.6	R	A	Y	Y
89	3.1	A	A	N	Y
90	3.7	SR	A	N	Y
91	5.1	SR	A	N	N
92	3.5	R	A	Y	N
93	4.6	SR	A	N	Y
94	6.1	R	A	N	Y
95	5.0	R	A	N	Y
96	3.8	SA	A	N	Y
97	3.5	R	A	Y	Y
98	3.7	SR	A	N	Y
99	5.9	SR	A	N	Y
100	3.0	A	A	N	N

Angularity- R: Rounded, SR: Subrounded, SA: Subangular, A: Angular.
Lithology- A: Andesite, I: Ignimbrite.
Ventifaction/Pitting- Y: Yes, N: No.

Alluvial Fan Surface ID#: Qs2A5				Date: 7/15/2014	
Comments: Includes Cobbles w/ Intermediate Axis ≥ 1.5 cm. Declination: 5°2' W.					
Cobble ID#	**Inter. Axis (cm)**	**Angularity**	**Lithology**	**Ventifaction**	**Pitted**
1	6.8	SR	A	Y	N
2	3.2	R	A	N	Y
3	4.1	SA	A	N	N
4	6.6	SA	A	N	Y
5	5.6	A	A	Y	N
6	5.2	SA	A	N	Y
7	6.7	SA	A	N	Y
8	2.7	A	A	N	Y
9	2.7	SA	A	N	N
10	3.4	SR	A	N	Y
11	3.2	SA	A	N	Y
12	2.9	SA	A	N	N
13	3.9	SR	A	Y	Y
14	3.6	R	A	N	N
15	3.8	SR	A	N	Y
16	3.1	R	A	N	Y
17	4.7	SR	A	Y	Y
18	3.1	R	A	N	Y
19	3.6	SA	A	N	N
20	3.8	SR	A	N	Y
21	3.6	SA	A	Y	Y
22	4.0	SR	A	N	Y
23	5.9	SA	A	N	N
24	2.6	SR	A	N	Y
25	3.0	SA	A	N	N
26	3.1	SA	A	Y	N
27	4.6	SR	A	N	Y
28	4.0	SR	A	N	N
29	3.7	R	A	Y	Y
30	4.6	SR	A	N	N
31	4.2	SA	A	Y	Y
32	4.2	R	A	N	Y
33	2.2	R	A	N	Y
34	2.5	A	A	Y	N
35	2.9	SA	A	N	Y
36	2.5	SR	A	N	N
37	4.1	SA	A	N	Y
38	6.2	SR	A	N	Y
39	5.1	SA	A	N	N
40	3.9	SA	A	Y	N
41	3.4	SR	A	N	Y
42	5.8	R	A	Y	Y
43	3.6	SA	A	N	Y
44	4.0	SA	A	N	Y
45	4.2	SA	A	N	Y
46	5.1	SR	A	N	N
47	3.5	R	A	N	Y
48	2.9	SR	A	N	Y
49	2.1	SR	A	Y	Y
50	2.9	R	A	Y	N
51	3.2	SA	A	Y	N
52	6.9	SA	A	N	Y
53	3.9	SR	A	N	Y
54	4.5	SR	A	Y	Y
55	3.2	SR	A	N	N
56	4.2	SA	A	N	Y
57	5.1	A	A	N	N
58	6.2	SR	I	Y	Y
59	2.5	A	A	Y	N
60	7.4	SR	I	Y	N
61	3.1	SR	A	Y	Y
62	5.0	A	A	Y	Y
63	5.2	R	A	Y	Y
64	4.4	SR	A	Y	Y
65	6.1	SA	A	N	Y
66	3.6	SA	A	Y	N
67	4.9	SR	A	Y	Y
68	4.6	SR	A	N	N
69	3.5	SA	A	Y	N
70	3.6	SA	A	N	Y
71	4.7	SR	A	N	Y
72	3.9	SR	A	N	N
73	2.6	SA	A	N	Y
74	3.2	SR	A	Y	N
75	5.2	R	A	Y	Y
76	4.8	SA	A	Y	N
77	6.1	R	A	Y	Y
78	4.6	SR	A	N	Y
79	3.9	SA	A	N	N
80	4.0	R	A	N	Y
81	3.0	SA	A	N	N
82	3.5	SA	A	Y	Y
83	4.6	SR	A	N	Y
84	2.7	SR	A	Y	Y
85	3.6	R	A	Y	N
86	2.1	SR	A	N	Y
87	3.4	R	A	Y	Y
88	4.1	SA	A	N	N
89	3.4	R	A	N	Y
90	8.0	SR	A	Y	N
91	3.2	SR	A	Y	N
92	3.0	A	A	N	N
93	4.5	R	A	N	Y
94	3.3	SA	A	N	Y
95	8.1	SA	A	Y	Y
96	5.6	R	A	N	N
97	4.9	R	A	Y	Y
98	4.1	SA	A	N	Y
99	5.9	SR	A	Y	N
100	5.2	SR	A	N	N

Angularity- R: Rounded, SR: Subrounded, SA: Subangular, A: Angular.
Lithology- A: Andesite, I: Ignimbrite.
Ventifaction/Pitting- Y: Yes, N: No.

Alluvial Fan Surface ID#: Qs2B1				Date: 7/25/2014	
Comments: Includes Cobbles w/ Intermediate Axis ≥ 1.5 cm. Declination: 5°2' W.					
Cobble ID#	**Inter. Axis (cm)**	**Angularity**	**Lithology**	**Ventifaction**	**Pitted**
1	5.5.	SA	A	Y	N
2	6.2	SR	A	Y	Y
3	1.8	SA	A	N	N
4	2.0	SA	A	N	Y
5	3.1	SA	A	Y	N
6	3.8	SR	A	Y	Y
7	2.5	SA	A	Y	N
8	6.6	SR	A	Y	Y
9	4.2	SA	A	Y	Y
10	3.8	R	A	N	N
11	3.5	SR	A	Y	Y
12	3.6	SR	A	N	N
13	1.9	SA	A	Y	N
14	4.5	SR	A	Y	Y
15	4.2	SR	A	Y	Y
16	2.7	SA	A	Y	Y
17	1.8	SR	A	N	N
18	4.9	SR	A	Y	N
19	3.1	SA	A	N	N
20	2.7	R	A	Y	Y
21	2.2	SA	A	Y	Y
22	3.4	SA	A	Y	N
23	4.0	SR	A	Y	Y
24	4.0	SA	A	Y	Y
25	2.2	SR	A	N	Y
26	3.1	SA	A	Y	N
27	3.3	SR	A	Y	Y
28	2.5	R	A	N	N
29	4.6	SR	A	Y	N
30	3.7	SR	A	Y	Y
31	2.1	R	A	N	Y
32	3.5	SA	A	Y	N
33	5.1	R	A	Y	N
34	2.9	SA	A	Y	Y
35	2.7	SR	A	Y	Y
36	3.0	SA	A	N	N
37	4.3	R	A	Y	Y
38	4.1	SR	A	Y	Y
39	3.9	R	A	N	Y
40	4.2	SA	A	Y	Y
41	4.7	R	A	N	N
42	3.6	R	A	N	N
43	3.2	SA	A	Y	Y
44	3.0	SR	A	Y	Y
45	1.8	SA	A	N	Y
46	2.1	SA	A	N	N
47	2.6	SR	A	Y	Y
48	3.4	SA	A	Y	N
49	2.2	R	A	N	N
50	2.1	SR	A	Y	Y
51	3.9	SR	A	Y	Y
52	5.7	SR	A	Y	Y
53	2.6	SR	A	Y	N
54	5.4	SR	A	Y	Y
55	1.7	SA	A	N	Y
56	3.5	SR	A	Y	Y
57	4.0	A	A	Y	Y
58	3.5	SR	A	Y	Y
59	2.7	SR	A	Y	Y
60	2.0	SR	A	Y	Y
61	3.9	SR	A	Y	Y
62	2.4	SA	A	Y	Y
63	4.8	SA	A	Y	N
64	2.7	SR	A	Y	N
65	2.7	SA	A	N	Y
66	3.5	SR	A	Y	Y
67	2.5	SA	A	N	N
68	3.6	SR	A	Y	Y
69	1.8	SR	A	N	N
70	3.3	SA	A	Y	N
71	3.4	R	A	N	Y
72	2.0	SR	A	Y	Y
73	2.2	SA	A	Y	Y
74	2.8	SA	A	N	Y
75	2.4	R	A	N	Y
76	2.4	A	A	Y	Y
77	2.9	SR	A	Y	Y
78	3.0	SR	A	Y	Y
79	3.3	SR	A	Y	Y
80	3.8	SR	A	Y	Y
81	2.7	SA	A	N	Y
82	2.0	SR	A	Y	Y
83	3.2	R	A	N	Y
84	2.6	SR	A	Y	Y
85	2.7	SR	A	Y	Y
86	2.8	SR	A	Y	N
87	3.7	R	A	N	N
88	3.5	SR	A	Y	Y
89	3.5	SR	A	N	N
90	3.6	SR	A	Y	Y
91	2.0	SA	A	Y	Y
92	3.6	R	A	N	Y
93	2.2	R	A	Y	Y
94	3.4	SR	A	N	Y
95	1.9	SR	A	Y	Y
96	2.5	R	A	N	N
97	4.0	SR	A	Y	Y
98	4.9	R	A	Y	Y
99	3.3	SR	A	Y	N
100	4.9	R	A	N	N

Angularity- R: Rounded, SR: Subrounded, SA: Subangular, A: Angular.
Lithology- A: Andesite, I: Ignimbrite.
Ventifaction/Pitting- Y: Yes, N: No.

Alluvial Fan Surface ID#: Qs2B2				Date: 7/25/2014	
Comments: Includes Cobbles w/ Intermediate Axis ≥ 1.5 cm. Declination: 5°2' W.					
Cobble ID#	**Inter. Axis (cm)**	**Angularity**	**Lithology**	**Ventifaction**	**Pitted**
1	6.8	R	A	Y	Y
2	6.9	SR	A	Y	Y
3	9.4	SR	A	Y	Y
4	10.9	SR	A	Y	Y
5	15.1	R	A	Y	Y
6	14.5	SR	A	Y	N
7	6.0	R	A	Y	Y
8	8.0	SR	A	Y	Y
9	4.4	SR	A	Y	Y
10	6.9	A	A	N	N
11	10.4	R	A	Y	Y
12	11.5	R	A	Y	Y
13	6.7	R	A	Y	Y
14	7.9	R	A	Y	Y
15	7.2	SR	A	Y	Y
16	9.6	R	A	Y	Y
17	6.9	R	A	N	N
18	5.5	SR	A	Y	Y
19	8.2	R	A	N	N
20	8.4	R	A	Y	N
21	8.7	R	A	Y	Y
22	5.0	R	A	Y	Y
23	4.7	R	A	Y	Y
24	3.2	SA	A	N	N
25	7.5	SR	A	Y	Y
26	12.4	R	A	Y	Y
27	9.3	R	A	Y	Y
28	14.9	SR	A	Y	Y
29	5.5	SR	A	Y	Y
30	13.1	R	A	N	Y
31	8.9	SR	A	Y	Y
32	9.0	SA	A	Y	Y
33	11.4	SR	A	Y	Y
34	6.4	SR	A	Y	Y
35	7.7	SR	A	Y	Y
36	4.8	SR	A	Y	Y
37	7.4	SR	I	Y	N
38	7.7	R	A	Y	Y
39	6.2	SR	A	Y	Y
40	6.5	R	A	Y	Y
41	15.0	R	A	Y	Y
42	11.4	SR	A	N	Y
43	7.0	SR	A	Y	Y
44	10.3	R	A	Y	Y
45	10.9	SR	A	Y	Y
46	9.9	SR	A	Y	Y
47	7.3	R	A	Y	Y
48	7.2	R	A	Y	Y
49	5.0	SA	A	N	N
50	9.0	SR	A	Y	N
51	9.1	R	A	Y	Y
52	6.1	SR	A	Y	Y
53	10.5	R	A	Y	Y
54	6.2	R	A	Y	Y
55	10.1	SR	A	Y	Y
56	8.5	SR	A	Y	Y
57	4.0	R	A	Y	Y
58	7.2	R	A	Y	Y
59	8.5	R	A	Y	Y
60	11.4	R	A	Y	Y
61	8.8	R	A	Y	Y
62	6.5	SR	A	Y	N
63	5.5	SA	A	Y	N
64	7.5	SR	A	Y	Y
65	7.2	SR	A	Y	Y
66	6.7	SR	A	Y	Y
67	5.5	SR	A	Y	Y
68	13.5	R	A	N	Y
69	6.9	SR	A	Y	Y
70	12.4	SR	A	Y	N
71	6.6	R	A	Y	Y
72	13.5	R	A	Y	Y
73	6.3	R	A	Y	Y
74	12.0	R	A	Y	Y
75	15.2	SR	A	Y	Y
76	5.5	R	A	Y	Y
77	7.1	SA	A	N	N
78	13.3	R	A	Y	Y
79	6.0	R	A	Y	Y
80	11.4	SR	A	Y	Y
81	10.4	SR	A	N	N
82	10.5	SR	A	N	Y
83	8.4	R	A	N	Y
84	7.6	SR	A	Y	Y
85	10.0	R	A	N	N
86	8.9	SR	A	Y	Y
87	6.7	SA	A	N	N
88	11.0	R	A	Y	Y
89	8.8	R	A	Y	Y
90	12.9	R	A	N	Y
91	6.7	SR	A	Y	Y
92	23.5	SR	I	Y	N
93	5.0	R	A	N	Y
94	14.8	R	A	Y	Y
95	8.8	R	A	Y	Y
96	6.5	R	A	Y	Y
97	7.2	SR	A	Y	Y
98	10.9	SR	A	Y	Y
99	5.4	SR	A	Y	Y
100	12.7	R	A	Y	Y

Angularity- R: Rounded, SR: Subrounded, SA: Subangular, A: Angular.
Lithology- A: Andesite, I: Ignimbrite.
Ventifaction/Pitting- Y: Yes, N: No.

Debris Flow ID#: Qd1B, Debris Flow #1, Distal								Date: 7/10/2014											
Comments: 30m x 30m Quadrant, Includes Boulders w/ Intermediate Axis ≥ 30 cm. Declination: 5°2' W																			
Boulder ID#	Pitted	Mx. Pit Dpth (cm)	Avg. Pit Dpth (cm)	Split	Ht. Resist. Grains (Mx) (cm)	Exfoliation ± Spalling	Boulder Relief (cm)	Intermediate Axis (cm)	Long Axis (cm)	Short Axis (cm)	Angularity	Ventifaction	Ventifaction Orientation (°)	Mx. Ventifaction (cm)	Avg. Ventifaction (cm)	Fracture	Composition	GPS ID#	Comments
1	N	-	-	N	-	N	50.6	74.2	99.4	50.6	SA	Y	321	0.5	0.28	Y	A	df1-bc1	
2	N	-	-	N	1.1	N	7.1	35.2	47.1	7.1	SR	Y	309	3	1.6	N	I	df1-bc2	
3	N	-	-	N	0.6	N	13.4	33.2	44.3	13.4	SR	Y	333	1.5	0.69	N	I	df1-bc3	
4	Y	0.4	0.3	N	-	N	30.2	41.3	55.1	30.2	SR	Y	335	1.7	0.83	N	A	df1-bc4	
5	Y	0.6	0.36	Y	0.7	N	17.5	30.1	34	17.5	R	Y	307	0.3	0.15	N	A	df1-bc5	
6	Y	0.6	0.21	N	-	N	21.5	32.1	43.2	21.5	R	Y	315	0.8	0.54	Y	A	df1-bc6	
7	N	-	-	N	0.9	N	13.5	32.6	38.2	13.5	SR	Y	319	3.2	1.77	N	I	df1-bc7	
8	Y	0.4	0.2	N	-	N	42.3	44.5	48.2	42.3	SR	Y	339	1.3	0.44	N	A	df1-bc8	
9	Y	2.2	0.85	Y	0.6	N	23.4	32.7	41.2	23.4	SA	Y	309	9.7	2.63	N	I	df1-bc9	
10	Y	0.6	0.33	N	0.2	N	43.8	49.2	57.2	43.8	R	Y	327	0.6	0.21	Y	A	df1-bc10	
11	N	-	-	N	0.1	Y	36.8	44.6	52	36.8	SR	N	-	-	-	N	A	df1-bc11	
12	N	-	-	N	0.1	N	44.2	44.2	48	41.2	SR	Y	319	-	-	N	A	df1-bc12	
13	N	-	-	N	0.3	N	21.8	38.8	43.2	21.8	SA	Y	321	3.6	1.91	N	I	df1-bc13	
14	N	-	-	N	0.4	N	27.8	38.2	57.4	27.8	SA	Y	327	5.2	2.61	N	I	df1-bc14	
15	N	-	-	N	0.2	N	31.2	31.2	44.4	31.2	SA	Y	320	0.3	0.18	N	A	df1-bc15	
16	Y	0.1	0.1	N	0.2	N	46.4	52	52.8	46.4	SR	Y	-	-	-	Y	A	df1-bc16	
17	N	-	-	N	0.4	Y	25	63.2	91.4	25	R	Y	315	1.3	0.7	N	I	df1-bc17	
18	Y	0.4	0.41	N	-	N	29.8	29.8	42.8	29.8	SA	Y	324	1.3	0.63	N	A	df1-bc18	
19	N	-	-	N	0.4	N	25.8	37	62.2	25.8	A	Y	329	2.5	1.91	N	I	df1-bc19	
20	Y	0.2	0.125	Y	-	N	14.5	31	43	14.5	R	Y	328	-	-	N	A	df1-bc20	
21	Y	0.2	0.12	N	-	N	22.4	39.8	49.2	22.4	SA	Y	331	-	-	N	A	df1-bc21	
22	N	-	-	N	0.4	N	9.6	56.2	61.4	9.6	SA	Y	323	2.3	1.43	N	I	df1-bc22	
23	N	-	-	N	0.2	N	15.7	37.2	40.4	15.7	SA	Y	315	1.5	0.86	N	I	df1-bc23	
24	Y	0.3	0.21	N	-	Y	9.3	33.2	51	9.3	R	Y	322	0.8	0.3	N	A	df1-bc24	
25	N	-	-	N	0.4	N	12.3	41.2	49.8	12.3	SR	Y	310	2.1	1.58	N	I	df1-bc25	
26	N	-	-	N	-	N	17.2	42.5	50.8	17.2	R	Y	322	0.3	0.18	N	A	df1-bc26	
27	N	-	-	N	-	N	20.8	33.2	36.7	20.8	R	Y	305	0.5	0.22	N	A	df1-bc27	
28	Y	0.2	0.11	N	0.3	N	26.8	31.2	34.6	26.8	SR	Y	329	-	-	N	A	df1-bc28	
29	Y	0.2	0.09	N	-	N	27.6	33.2	43	27.6	R	Y	311	0.5	0.37	Y	A	df1-bc29	
30	Y	0.7	0.21	N	-	N	29.8	31	43.5	29.8	R	Y	315	3.5	1.7	N	I	df1-bc30	
31	Y	0.3	0.14	N	0.2	N	23.8	48.2	51	23.8	SR	Y	305	0.4	0.23	Y	A	df1-bc31	
32	Y	0.4	0.26	N	0.1	N	28.6	39	57.2	28.6	SA	Y	312	-	-	Y	A	df1-bc32	
33	N	-	-	N	0.1	N	31.2	46	52.2	31.2	SR	Y	330	1.9	0.97	N	A	df1-bc33	
34	Y	0.2	0.12	Y	0.3	N	24.5	44.2	46.4	24.5	R	Y	326	1.6	0.66	N	I	df1-bc34	
35	N	-	-	N	0.1	N	29.8	30.1	34	29.8	R	Y	327	-	-	N	A	df1-bc35	

Angularity- R: Rounded, SR: Subrounded, SA: Subangular, A: Angular. *Lithology*- A: Andesite, I: Ignimbrite. *Ventifaction/Split/Pitting/Exfoliation/Fractu*re- Y: Yes, N: No.

Debris Flow ID#: Qd1B, Debris Flow #1, Middle								Date: 7/10/2014										
Comments: 30m x 30m Quadrant, Includes Boulders w/ Intermediate Axis ≥ 30 cm. Declination: 5°2' W																		
Boulder ID#	Pitted	Mx. Pit Dpth (cm)	Avg. Pit Dpth (cm)	Split	Ht. Resist. Grains (Mx) (cm)	Exfoliation ± Spalling	Boulder Relief (cm)	Intermediate Axis (cm)	Long Axis (cm)	Short Axis (cm)	Angularity	Ventifaction	Ventifaction Orientation (°)	Mx. Ventifaction (cm)	Avg. Ventifaction (cm)	Fracture	Composition	GPS ID#	Comments
1	Y	0.6	0.33	N	0.1	N	42.2	97.6	100.2	42.2	R	Y	309	0.9	0.35	Y	A	df1-bc1	
2	Y	1	0.55	N	1.1	N	76.8	76.8	140.2	76.8	R	Y	314	8.2	5.13	Y	I	df1-bc2	
3	N	-	-	N	-	N	14.1	45.4	50.8	14.1	R	Y	299	0.6	0.33	N	A	df1-bc3	
4	Y	0.3	0.18	N	0.2	N	35.2	82.8	86	35.2	R	Y	-	-	-	N	A	df1-bc4	
5	N	-	-	N	0.3	N	48	46.3	48	48	SA	Y	322	8.5	3.52	N	I	df1-bc5	
6	N	-	-	N	-	N	28.2	34	41	28.2	SR	Y	-	-	-	N	A	df1-bc6	
7	N	-	-	N	0.5	N	11.9	34.5	73.2	11.9	SA	N	-	-	-	N	A	df1-bc7	
8	N	-	-	N	0.8	N	9.2	46	70.2	9.2	R	Y	319	-	-	N	I	df1-bc8	
9	N	-	-	N	-	Y	23.8	36.2	54.4	23.8	SR	Y	326	0.3	0.14	N	A	df1-bc9	
10	N	-	-	N	-	Y	19.6	34.8	54.5	19.6	SR	Y	299	-	-	N	A	df1-bc10	
11	Y	0.9	0.44	N	0.6	N	25.2	48.4	51.2	25.2	R	Y	306	4.9	1.74	Y	I	df1-bc11	
12	Y	1.7	0.7	N	0.8	N	28.2	53.5	55	28.2	R	Y	329	11.2	3.09	N	I	df1-bc12	
13	Y	0.9	0.71	N	0.3	N	55.2	80.8	83.2	55.2	R	Y	316	0.8	0.73	Y	A	df1-bc13	
14	Y	1	0.58	N	0.5	Y	44.8	70	104.2	44.8	SR	Y	314	4	2.78	Y	I	df1-bc14	
15	Y	0.7	0.45	N	0.5	N	28.6	43.8	54.8	28.6	SR	Y	295	4.4	2.1	Y	I	df1-bc15	
16	N	-	-	N	0.6	N	30	50	70.2	30	SA	Y	307	5.5	2.52	N	I	df1-bc16	
17	Y	2.1	1.02	N	-	N	34.4	54.2	67.5	34.4	SR	Y	302	2.5	0.74	N	A	df1-bc17	
18	Y	1.1	0.58	N	0.2	N	30.6	97.4	124.9	30.6	R	Y	314	6.4	3.5	N	I	df1-bc18	
19	Y	1.3	0.72	N	0.4	N	57.8	91.2	94.6	57.8	SA	Y	310	9.5	3.9	Y	I	df1-bc19	
20	Y	0.3	0.15	N	0.2	N	18.2	34.2	48	18.2	R	Y	317	-	-	N	A	df1-bc20	
21	Y	0.6	0.45	N	0.4	N	30.4	39.8	71	30.4	SR	Y	317	1.6	0.95	N	A	df1-bc21	
22	N	-	-	N	0.8	N	5.9	45	45	5.9	R	Y	304	0.9	0.6	N	I	df1-bc22	
23	N	-	-	N	0.3	N	20.6	56.5	64.2	20.6	SR	Y	314	7.2	3.32	N	I	df1-bc23	
24	Y	0.3	0.15	N	0.3	N	19.8	47	56.8	19.8	SR	Y	301	0.5	0.24	Y	A	df1-bc24	
25	Y	0.9	0.44	N	0.7	N	22.8	49.2	88.1	22.8	SR	Y	304	5.1	2.75	N	I	df1-bc25	
26	N	-	-	N	0.5	N	29	49.4	67	29	R	Y	303	7.9	4.46	N	I	df1-bc26	
27	Y	0.4	0.21	N	0.1	N	27	36.8	45.2	27	R	Y	315	0.9	0.35	N	A	df1-bc27	
28	Y	0.8	0.32	N	0.1	N	25.4	36.2	42.4	25.4	R	Y	323	0.3	0.17	N	A	df1-bc28	
29	Y	0.5	0.23	N	0.2	N	22.2	34.4	52	22.2	SA	Y	321	-	-	N	A	df1-bc29	
30	Y	0.7	0.33	N	0.4	N	20.6	42	49.8	20.6	R	Y	311	3.8	1.62	Y	I	df1-bc30	
31	Y	0.2	0.13	N	-	N	25	34.6	50.6	25	R	Y	308	0.6	0.23	N	A	df1-bc31	
32	Y	1.3	0.45	N	0.7	N	30.6	54.2	60.8	30.6	SA	Y	327	6.6	2.92	N	I	df1-bc32	
33	Y	0.4	0.21	N	0.1	N	26.8	30.2	41.8	26.8	R	Y	301	6.1	2.9	N	I	df1-bc33	
34	Y	0.8	0.36	N	0.2	N	23	37	59.6	23	SR	Y	302	3.8	2	Y	I	df1-bc34	
35	Y	0.5	0.32	N	1.2	N	29.2	61	70.6	29.2	SR	Y	297	-	-	N	A	df1-bc35	
36	Y	0.5	0.31	N	0.3	N	26.4	38.2	46.4	26.4	R	Y	305	0.4	0.25	N	A	df1-bc36	

Angularity- R: Rounded, SR: Subrounded, SA: Subangular, A: Angular. *Lithology*- A: Andesite, I: Ignimbrite. *Ventifaction/Split/Pitting/Exfoliation/Fractu*re- Y: Yes, N: No.

Debris Flow ID#: Qd1B, Debris Flow #1, Proximal Flow								Date: 7/11/2014										
Comments: 30m x 30m Quadrant, Includes Boulders w/ Intermediate Axis ≥ 30 cm. Declination: 5°2' W																		
Boulder ID#	Pitted	Mx. Pit Dpth (cm)	Avg. Pit Dpth (cm)	Split	Ht. Resist. Grains (Mx) (cm)	Exfoliation ± Spalling	Boulder Relief (cm)	Intermediate Axis (cm)	Long Axis (cm)	Short Axis (cm)	Angularity	Ventifaction	Ventifaction Orientation (°)	Mx. Ventifaction (cm)	Avg. Ventifaction (cm)	Fracture	Composition	GPS ID#	Comments
1	N	-	-	N	0.4	N	18.8	59.8	71.2	18.8	R	Y	305	2.3	1.63	N	I	df1-bc1	
2	N	-	-	N	0.5	N	15.2	85.3	110.2	15.2	R	Y	318	5.2	3.16	N	I	df1-bc2	
3	Y	0.3	0.18	N	0.7	N	22.2	50.6	72.2	22.2	SR	Y	312	2.4	1.66	N	I	df1-bc3	
4	Y	0.4	0.22	N	0.4	N	55.4	67.2	105.5	55.4	SR	Y	308	3	1.98	N	I	df1-bc4	
5	N	-	-	N	0.5	N	18.4	52.2	79.6	18.4	SR	N	-	-	-	N	A	df1-bc5	
6	N	-	-	N	0.5	N	43.6	76	90.2	43.6	SA	Y	309	1.6	0.97	N	I	df1-bc6	
7	N	-	-	N	0.4	N	37.5	67.8	89.2	37.5	SA	Y	311	-	-	N	I	df1-bc7	
8	Y	0.6	0.26	N	0.3	Y	37.8	48.4	77.2	37.8	SA	Y	297	-	-	Y	I	df1-bc8	
9	Y	0.5	0.35	N	0.3	N	78.8	84.2	117.4	78.8	SA	Y	334	4.3	1.58	N	I	df1-bc9	
10	Y	0.5	0.28	N	-	N	11.4	57.2	68.4	11.4	R	Y	329	0.4	0.32	N	A	df1-bc10	
11	N	-	-	N	0.3	N	27.2	51.2	88.6	27.2	SA	Y	304	3	1.24	Y	I	df1-bc11	
12	N	-	-	N	0.1	N	18.8	40.8	60	18.8	SR	N	-	-	-	N	A	df1-bc12	
13	N	-	-	N	0.1	N	15.8	44.4	47	15.8	SA	Y	324	0.3	0.22	N	I	df1-bc13	
14	N	-	-	N	-	N	11.1	43.4	51.6	11.1	SR	Y	321	0.7	0.4	N	I	df1-bc14	
15	Y	0.4	0.21	N	0.1	N	27.9	60.8	65.4	27.9	R	Y	323	0.5	0.32	N	A	df1-bc15	
16	N	-	-	N	0.5	Y	85.8	134.2	132.4	85.8	R	Y	305	5.9	2.51	N	I	df1-bc16	
17	N	-	-	N	0.3	N	38.2	77.8	85.2	38.2	SA	Y	301	1.9	1.04	N	I	df1-bc17	
18	Y	0.4	0.22	N	0.7	N	62.4	87.8	90.6	62.4	SA	Y	307	2.9	1.51	Y	I	df1-bc18	

Angularity- R: Rounded, SR: Subrounded, SA: Subangular, A: Angular. *Lithology*- A: Andesite, I: Ignimbrite. *Ventifaction/Split/Pitting/Exfoliation/Fractu*re- Y: Yes, N: No.

Debris Flow ID#: Qd1C, Debris Flow #2, Middle								Date: 7/14/2014										
Comments: 30m x 30m Quadrant, Includes Boulders w/ Intermediate Axis ≥ 30 cm. Declination: 5°2' W.																		
Boulder ID#	Pitted	Mx. Pit Dpth (cm)	Avg. Pit Dpth (cm)	Split	Ht. Resist. Grains (Mx) (cm)	Exfoliation ± Spalling	Boulder Relief (cm)	Intermediate Axis (cm)	Long Axis (cm)	Short Axis (cm)	Angularity	Ventifaction	Ventifaction Orientation (°)	Mx. Ventifaction (cm)	Avg. Ventifaction (cm)	Fracture	Composition	GPS ID#	Comments
1	Y	0.4	0.25	N	1	N	11.6	73.4	74.2	11.6	A	Y	302	6.2	3.625	N	I	df2-bc1	Planed
2	Y	1.7	0.85	N	0.1	N	31.8	82.2	93	31.8	A	Y	305	10.9	5.23	N	I	df2-bc2	
3	N	-	-	N	-	N	6.1	123	156.2	6.1	SA	Y	306	-	-	Y	I	df2-bc3	Planed
4	N	0.6	0.42	N	1.2	N	12.5	63.5	64.4	12.5	SA	Y	314	10.7	8.25	Y	I	df2-bc4	Planed
5	Y	0.7	0.38	N	0.9	N	41.2	86.2	89.8	41.2	SA	Y	316	6.8	4.68	N	I	df2-bc5	
6	Y	1.1	0.65	N	0.8	N	32.2	88.2	89.3	32.2	SA	Y	311	5.8	3.8	Y	I	df2-bc6	
7	Y	0.9	0.56	N	0.2	N	55.2	111.8	125.6	55.2	SR	Y	308	9	5.37	Y	I	df2-bc7	

Angularity- R: Rounded, SR: Subrounded, SA: Subangular, A: Angular. *Lithology*- A: Andesite, I: Ignimbrite. *Ventifaction/Split/Pitting/Exfoliation/Fractu*re- Y: Yes, N: No.

Debris Flow ID#: Qd1C, Debris Flow #2, Proximal								Date: 7/14/2014										
Comments: 30m x 30m Quadrant, Includes Boulders w/ Intermediate Axis ≥ 30 cm. Declination: 5°2' W																		
Boulder ID#	Pitted	Mx. Pit Dpth (cm)	Avg. Pit Dpth (cm)	Split	Ht. Resist. Grains (Mx) (cm)	Exfoliation ± Spalling	Boulder Relief (cm)	Intermediate Axis (cm)	Long Axis (cm)	Short Axis (cm)	Angularity	Ventifaction	Ventifaction Orientation (°)	Mx. Ventifaction (cm)	Avg. Ventifaction (cm)	Fracture	Composition	GPS ID#	Comments
1	N	-	-	N	0.3	Y	63.6	145	220.8	63.6	SR	Y	309	17.3	8.58	Y	I	df2-bc1	
2	Y	2	0.55	N	0.5	N	105.2	141.6	188.8	105.2	SA	Y	300	13	6.3	Y	I	df2-bc2	
3	Y	0.5	0.36	N	0.1	N	99.6	132.2	144.8	99.6	SA	Y	310	24.3	8.2	Y	I	df2-bc3	
4	Y	0.7	0.33	N	0.5	N	70.2	92.8	192	70.2	SR	Y	300	12	6.4	N	I	df2-bc4	Shielded
5	Y	0.7	0.42	N	0.4	N	25.4	86.8	111.6	25.4	SA	Y	304	12.1	7.23	N	I	df2-bc5	
6	Y	1.2	0.56	N	0.1	N	28.6	82.4	84.2	28.6	SA	Y	302	5.2	3.4	Y	I	df2-bc6	
7	Y	0.7	0.45	N	0.2	N	44	62.4	75.2	44	SA	Y	304	10.1	6.49	N	I	df2-bc7	
8	Y	1	0.95	N	0.2	N	35.1	61.2	123.8	35.1	A	Y	315	12.1	5.29	N	I	df2-bc8	
9	Y	2.4	0.82	N	1.2	N	121	236.2	239.6	121	SA	Y	300	13.5	6.96	Y	I	df2-bc9	
10	N	-	-	N	0.3	N	15.3	66.4	71.8	15.3	SR	Y	301	14.2	7.9	N	I	df2-bc10	Planed
11	N	-	-	N	0.1	N	9.7	46	94.3	9.7	SR	Y	300	8.1	7.8	N	I	df2-bc11	Planed
12	N	-	-	N	-	N	9.7	42.2	55	9.7	SR	Y	306	3.8	3.3	N	I	df2-bc12	Planed
13	N	-	-	N	0.4	N	12.7	46.8	53	12.7	SR	Y	307	3.5	2.6	N	I	df2-bc13	Planed
14	Y	0.7	0.46	N	0.3	N	24	36	43.8	24	SA	Y	303	7.5	4.57	N	I	df2-bc14	
15	N	-	-	N	0.3	N	16.8	58	62.2	16.8	SR	Y	309	7.6	3.975	N	I	df2-bc15	Planed
16	N	-	-	N	0.1	N	7.2	70.8	94	7.2	SR	Y	311	10.1	5.54	N	I	df2-bc16	Planed

Angularity- R: Rounded, SR: Subrounded, SA: Subangular, A: Angular. *Lithology*- A: Andesite, I: Ignimbrite. *Ventifaction/Split/Pitting/Exfoliation/Fractu*re- Y: Yes, N: No.

Debris Flow ID#: Qd1D, Debris Flow #3, Middle								Date: 7/15/2014										
Comments: 30m x 30m Quadrant, Includes Boulders w/ Intermediate Axis ≥ 30 cm. Declination: 5°2' W																		
Boulder ID#	Pitted	Mx. Pit Dpth (cm)	Avg. Pit Dpth (cm)	Split	Ht. Resist. Grains (Mx) (cm)	Exfoliation ± Spalling	Boulder Relief (cm)	Intermediate Axis (cm)	Long Axis (cm)	Short Axis (cm)	Angularity	Ventifaction	Ventifaction Orientation (°)	Mx. Ventifaction (cm)	Avg. Ventifaction (cm)	Fracture	Composition	GPS ID#	Comments
1	Y	0.3	0.17	N	0.4	N	9.6	49.1	55	9.6	A	Y	313	6.9	2.7	N	I	df3-bc1	Planed
2	Y	1.1	0.52	N	1.6	N	27.8	102.8	125	27.8	R	Y	311	11.9	6.75	N	I	df3-bc2	Planed
3	Y	0.8	0.31	Y	0.7	N	29.9	132.8	146	29.9	R	Y	314	16.9	7.14	N	I	df3-bc3	Planed
4	N	-	-	N	-	N	7.3	82.8	103	7.3	SR	Y	301	8	5.5	N	I	df3-bc4	Planed
5	Y	1.8	1.11	N	2.1	N	64.8	115.4	142.5	64.8	R	Y	315	13.5	6.55	N	I	df3-bc5	
6	N	-	-	N	1.5	N	4.1	65.2	104.8	4.1	SA	Y	301	9.8	3.95	Y	I	df3-bc6	Planed
7	N	-	-	N	-	N	5.1	130.1	181.2	5.1	SA	Y	318	12.8	12.8	Y	I	df3-bc7	Planed
8	Y	0.7	0.53	N	0.3	N	14.6	108	130	14.6	SR	Y	320	10.7	8.46	N	I	df3-bc8	Planed
9	Y	1.1	0.52	N	0.5	N	56.6	105	111.2	56.6	SA	Y	316	12.3	6.9	N	I	df3-bc9	
10	Y	1.2	0.75	N	0.6	N	71.2	186.4	193.2	71.2	SR	Y	304	9.7	5.14	Y	I	df3-bc10	
11	N	-	-	N	1.2	N	11.7	154.5	201.4	11.7	R	Y	300	-	-	N	I	df3-bc11	Planed
12	Y	1.1	0.62	N	1.3	N	73.6	110.8	153.4	73.6	R	Y	304	16.2	8.61	Y	I	df3-bc12	
13	Y	4.5	0.91	N	0.2	N	69.9	119.8	144.5	69.9	SA	Y	315	9	5	N	I	df3-bc13	
14	Y	1.4	0.74	N	0.4	N	38.2	62.5	64.2	38.2	SA	Y	316	8.9	3.61	N	I	df3-bc14	
15	N	-	-	N	1.3	N	24	40.8	52.5	24	SR	Y	315	7	4.03	N	I	df3-bc15	
16	N	-	-	N	0.5	Y	7.5	44.2	61.7	7.5	R	Y	-	-	-	N	I	df3-bc16	Planed

Angularity- R: Rounded, SR: Subrounded, SA: Subangular, A: Angular. *Lithology*- A: Andesite, I: Ignimbrite. *Ventifaction/Split/Pitting/Exfoliation/Fractu*re- Y: Yes, N: No.

Debris Flow ID#: Qd1D, Debris Flow #3, Proximal								Date: 7/15/2014											
Comments: 30m x 30m Quadrant, Includes Boulders w/ Intermediate Axis ≥ 30 cm. Declination: 5°2' W																			
Boulder ID#	Pitted	Mx. Pit Dpth (cm)	Avg. Pit Dpth (cm)	Split	Ht. Resist. Grains (Mx) (cm)	Exfoliation ± Spalling	Boulder Relief (cm)	Intermediate Axis (cm)	Long Axis (cm)	Short Axis (cm)	Angularity	Ventifaction	Ventifaction Orientation (°)	Mx. Ventifaction (cm)	Avg. Ventifaction (cm)	Fracture	Composition	GPS ID#	Comments
1	Y	0.4	0.21	Y	0.5	N	37	47.4	78.2	37	SR	Y	315	13.2	5.5	Y	I	df3-bc1	
2	N	-	-	N	0.6	Y	64	64	78.2	60	SA	Y	311	14.8	5.78	N	I	df3-bc2	
3	Y	1.3	0.67	N	0.5	N	42.8	58	66	42.8	SA	Y	313	9	4.06	N	I	df3-bc3	
4	Y	1.7	0.67	N	1	N	39.2	73.8	82	39.2	SR	Y	325	15.2	7.54	N	I	df3-bc4	
5	Y	1	0.95	N	0.4	N	35.2	82.4	83	35.2	SA	Y	326	12	6.25	N	I	df3-bc5	Planed
6	Y	1	0.69	N	1.1	N	102.2	123.8	177.4	102.2	A	Y	315	9.2	6.38	Y	I	df3-bc6	
7	Y	0.9	0.56	N	0.9	Y	34.6	50.8	141.2	34.6	SR	Y	324	14.3	7.15	N	I	df3-bc7	
8	N	-	-	Y	0.1	Y	24.8	35	46	24.8	SR	Y	323	4.7	3.5	N	I	df3-bc8	
9	Y	0.6	0.39	N	0.7	N	55.2	89.8	152	55.2	SA	Y	304	6.4	5.47	Y	I	df3-bc9	
10	Y	2.1	0.73	Y	0.2	N	31	88.4	126.2	31	SR	Y	319	6.1	3.625	N	I	df3-bc10	
11	N	-	-	N	0.5	N	18.1	76.4	101.2	18.1	R	Y	303	8.9	2.91	N	I	df3-bc11	Planed
12	Y	2.7	1.25	N	3	Y	39	80.3	107.8	39	SA	Y	319	10	5.35	Y	I	df3-bc12	
13	Y	1.3	0.55	N	-	N	43.2	43.2	63.1	40	A	Y	329	5.9	4.17	N	I	df3-bc13	

Angularity- R: Rounded, SR: Subrounded, SA: Subangular, A: Angular. *Lithology*- A: Andesite, I: Ignimbrite. *Ventifaction/Split/Pitting/Exfoliation/Fractu*re- Y: Yes, N: No.

Debris Flow ID#: Qd1A, Debris Flow #4, Distal								Date: 7/26/2014										
Comments: 30m x 30m Quadrant, Includes Boulders w/ Intermediate Axis ≥ 30 cm. Declination: 5°2' W																		
Boulder ID#	Pitted	Mx. Pit Dpth (cm)	Avg. Pit Dpth (cm)	Split	Ht. Resist. Grains (Mx) (cm)	Exfoliation ± Spalling	Boulder Relief (cm)	Intermediate Axis (cm)	Long Axis (cm)	Short Axis (cm)	Angularity	Ventifaction	Ventifaction Orientation (°)	Mx. Ventifaction (cm)	Avg. Ventifaction (cm)	Fracture	Composition	GPS ID#	Comments
1	Y	0.5	0.39	Y	1.9	N	34	146	182.6	34	R	Y	316	-	-	Y	I	df4-bc1	
2	N	-	-	N	-	N	19.2	34.2	39.6	19.2	R	Y	328	-	-	N	A	df4-bc2	
3	Y	0.6	0.42	N	0.2	N	22	30	38.4	22	R	Y	314	1.1	0.65	N	I	df4-bc3	
4	Y	0.6	0.33	N	0.2	N	27	32.2	45.4	27	R	Y	325	0.5	0.3	N	I	df4-bc4	
5	Y	1.3	0.7	N	0.5	N	19.2	35.8	48	19.2	SA	Y	329	-	-	N	I	df4-bc5	
6	Y	0.4	0.15	N	-	N	16	32	56.8	16	SR	Y	322	-	-	N	A	df4-bc6	
7	N	-	-	N	0.5	N	13	33	48.8	13	SA	Y	319	4.9	2.44	N	I	df4-bc7	
8	N	-	-	N	0.5	N	12.2	34.2	51.4	12.2	R	Y	325	-	-	N	I	df4-bc8	
9	Y	2	0.55	N	0.2	N	28	30	33.2	28	SR	Y	330	-	-	N	I	df4-bc9	
10	Y	0.5	0.33	N	0.2	N	17.8	36.8	55.2	17.8	SR	Y	305	-	-	N	I	df4-bc10	
11	N	-	-	N	0.5	N	8.2	34.8	41.8	8.2	R	Y	324	-	-	N	I	df4-bc11	
12	N	-	-	N	-	N	19.6	31.2	31.6	19.6	SA	N	-	-	-	N	A	df4-bc12	
13	Y	0.4	0.32	N	-	N	19.8	30.2	36.4	19.8	SR	Y	331	-	-	N	A	df4-bc13	
14	N	-	-	N	-	N	24	31	32.2	24	R	Y	326	-	-	N	A	df4-bc14	
15	Y	0.5	0.34	N	0.2	N	48.2	45.8	50	48.2	R	Y	320	-	-	N	A	df4-bc15	
16	N	-	-	N	-	N	31.8	31.2	31.2	20	SA	N	-	-	-	N	A	df4-bc16	Shielded
17	Y	0.1	0.1	N	-	N	15.2	30.1	36	15.2	R	Y	335	-	-	N	A	df4-bc17	
18	Y	0.1	0.1	N	-	N	30.8	54.2	75.6	30.8	SA	Y	310	-	-	N	A	df4-bc18	
19	Y	0.7	0.29	N	-	N	9.7	32.8	34	9.7	R	Y	334	-	-	N	A	df4-bc19	
20	N	-	-	N	-	N	18	44.8	51	18	SR	Y	329	-	-	N	A	df4-bc20	
21	N	0.2	0.11	N	0.2	N	28.9	37.9	47	28.9	SR	Y	327	-	-	N	A	df4-bc21	
22	Y	0.6	0.33	N	0.1	N	51	63.2	71.6	51	SA	Y	315	-	-	N	A	df4-bc22	
23	Y	0.5	0.25	N	0.3	N	12.5	41.2	46.4	12.5	R	Y	327	-	-	N	A	df4-bc23	
24	Y	0.4	0.28	Y	0.2	N	19.2	36	75.8	19.2	R	Y	335	-	-	N	A	df4-bc24	
25	N	-	-	Y	0.5	N	10.8	52.2	54.2	10.8	A	Y	325	3.5	1.54	N	I	df4-bc25	
26	N	-	-	N	-	N	25	41.6	58.4	25	SA	Y	320	-	-	N	A	df4-bc26	
27	Y	0.3	0.21	N	0.5	N	17.2	57	63	17.2	R	Y	311	-	-	N	I	df4-bc27	
28	N	-	-	N	0.1	N	16.2	56.8	73.5	16.2	SA	Y	327	-	-	N	I	df4-bc28	
29	N	-	-	N	-	N	18	31.2	53	18	R	Y	322	-	-	Y	A	df4-bc29	
30	Y	1.1	0.56	N	0.3	N	15.5	42.8	43.4	15.5	R	Y	327	-	-	N	I	df4-bc30	
31	Y	0.4	0.23	Y	0.5	N	20.8	30.1	41.2	20.8	R	Y	336	-	-	N	A	df4-bc31	
32	Y	0.1	0.1	N	0.2	N	15.5	31	34.8	15.5	R	Y	324	-	-	N	I	df4-bc32	
33	Y	0.7	0.35	N	0.6	Y	43	47.6	62	43	SA	Y	315	2.7	1.47	N	I	df4-bc33	
34	Y	0.3	0.22	N	0.1	N	20.4	30	42.5	20.4	R	Y	329	-	-	N	I	df4-bc34	
35	N	-	-	Y	0.5	Y	78.2	107.5	115	78.2	R	Y	334	4.7	2.85	N	I	df4-bc35	
36	N	-	-	Y	0.4	N	27.8	30.1	43.4	27.8	R	Y	311	-	-	N	I	df4-bc36	
37	Y	0.4	0.17	Y	0.1	N	33	37.2	42.1	33	SR	Y	-	-	-	Y	A	df4-bc37	
38	Y	0.4	0.17	N	0.3	N	22.4	50.2	68	22.4	R	Y	304	-	-	Y	A	df4-bc38	
39	Y	1.2	0.48	N	0.3	N	12.8	32	50	12.8	R	Y	319	2.7	1.38	N	I	df4-bc39	
40	Y	0.3	0.19	N	0.2	N	17.1	32.7	42.3	17.1	SA	Y	321	-	-	N	I	df4-bc40	
41	Y	0.5	0.28	Y	1.1	N	31.4	73.6	101	31.4	R	Y	313	3.1	1.92	N	I	df4-bc41	
42	Y	0.7	0.32	N	0.2	N	17	50	52	17	SA	Y	348	-	-	N	I	df4-bc42	
43	Y	0.1	0.1	N	-	N	7.2	31	45.2	7.2	R	Y	330	-	-	N	A	df4-bc43	
44	N	-	-	N	0.3	N	11.3	51.5	58	11.3	R	Y	303	-	-	N	I	df4-bc44	Planed
45	Y	0.5	0.18	N	0.1	N	18.6	42.4	48.2	18.6	R	Y	325	-	-	N	I	df4-bc45	
46	Y	0.5	0.32	N	0.3	N	17.6	42.4	49.2	17.6	SR	Y	324	2.1	1.26	N	I	df4-bc46	
47	Y	2.3	0.75	N	0.4	N	38.6	52.6	82.6	38.6	R	Y	306	-	-	N	I	df4-bc47	
48	N	0.1	0.1	N	-	N	25.4	31.8	39	25.4	R	Y	-	-	-	N	A	df4-bc48	
49	Y	0.1	0.1	N	-	N	22.4	30	35.2	22.4	SR	Y	321	-	-	N	A	df4-bc49	
50	Y	0.4	0.17	N	0.4	N	23.6	41.4	46.3	23.6	R	Y	323	4.3	2.37	N	I	df4-bc50	

Debris Flow ID#: Qd1A, Debris Flow #4, Distal CONT.								Date: 7/26/2014											
Comments: 30m x 30m Quadrant, Includes Boulders w/ Intermediate Axis ≥ 30 cm. Declination: 5°2' W																			
Boulder ID#	Pitted	Mx. Pit Dpth (cm)	Avg. Pit Dpth (cm)	Split	Ht. Resist. Grains (Mx) (cm)	Exfoliation ± Spalling	Boulder Relief (cm)	Intermediate Axis (cm)	Long Axis (cm)	Short Axis (cm)	Angularity	Ventifaction	Ventifaction Orientation (°)	Mx. Ventifaction (cm)	Avg. Ventifaction (cm)	Fracture	Composition	GPS ID#	Comments
51	Y	0.1	0.1	N	0.1	N	23	31.5	51.7	23	SR	Y	333	-	-	N	A	df4-bc51	
52	N	-	-	N	-	N	12	35.1	50.7	12	SA	Y	321	2.3	0.73	N	I	df4-bc52	
53	N	-	-	N	0.3	N	23.9	44	46.4	23.9	SA	Y	330	-	-	N	I	df4-bc53	
54	Y	0.1	0.1	N	0.1	N	33.2	40.9	56.1	33.2	R	Y	312	-	-	Y	A	df4-bc54	
55	Y	0.7	0.24	N	0.5	N	15.6	51.7	74.9	15.6	R	Y	333	-	-	N	I	df4-bc55	
56	Y	0.1	0.1	N	0.1	N	28	38	43.5	28	R	Y	320	-	-	N	A	df4-bc56	
57	N	-	-	N	-	N	3.9	41.1	57.8	3.9	SA	Y	313	-	-	N	I	df4-bc57	Planed
58	N	-	-	N	-	N	26.5	40.4	45.8	26.5	R	Y	304	-	-	N	A	df4-bc58	
59	Y	0.5	0.33	N	0.3	N	28.5	39.8	43	28.5	SR	Y	327	4	2.12	N	I	df4-bc59	
60	Y	0.1	0.1	N	-	N	10.9	33.3	42.4	10.9	R	Y	309	-	-	N	A	df4-bc60	
61	N	-	-	N	-	N	24.3	41.2	40.3	24.3	SA	Y	318	-	-	N	A	df4-bc61	
62	Y	0.6	0.26	N	0.3	N	25.7	29.5	37	25.7	R	Y	330	-	-	N	A	df4-bc62	
63	N	-	-	N	-	N	13.8	38	51.5	13.8	SR	Y	339	4.4	2.89	N	I	df4-bc63	Planed
64	Y	0.2	0.15	Y	0.3	N	28.1	41	64.9	28.1	SR	Y	310	-	-	Y	A	df4-bc64	
65	Y	0.2	0.11	N	-	N	25.8	35.3	41	25.8	R	Y	300	-	-	N	A	df4-bc65	
66	Y	0.4	0.19	N	0.3	N	17.7	34	37.9	17.7	SA	Y	306	4.4	2.07	N	I	df4-bc66	
67	N	-	-	N	-	N	4.9	39.7	53.6	4.9	SR	Y	313	3.5	1.6	N	I	df4-bc67	
68	N	-	-	N	0.1	N	16.9	43.3	59.5	16.9	SA	Y	-	-	-	N	A	df4-bc68	
69	N	-	-	N	0.6	N	14.2	38.1	41.6	14.2	A	Y	301	2.9	1.63	N	I	df4-bc69	
70	Y	0.4	0.21	N	-	N	31.2	31.2	38.3	31.2	R	Y	300	-	-	N	A	df4-bc70	
71	N	-	-	N	-	N	18.1	30	45.3	18.1	SR	Y	344	1.6	0.7	N	A	df4-bc71	
72	Y	0.4	0.2	N	0.1	Y	17.6	44.3	49	17.6	R	Y	304	-	-	N	A	df4-bc72	
73	Y	0.3	0.2	N	0.2	N	20	29.9	56.7	20	SA	Y	296	2.1	1.38	Y	I	df4-bc73	
74	N	-	-	N	1	N	16.5	38	43.9	16.5	R	Y	320	5.6	2.68	N	I	df4-bc74	
75	Y	1.5	0.78	N	0.4	N	23.8	32.9	38	23.8	R	Y	300	-	-	N	I	df4-bc75	

Angularity- R: Rounded, SR: Subrounded, SA: Subangular, A: Angular. *Lithology*- A: Andesite, I: Ignimbrite. *Ventifaction/Split/Pitting/Exfoliation/Fractu*re- Y: Yes, N: No.

Debris Flow ID#: Qd1A, Debris Flow #4, Middle								Date: 7/27/2014											
Comments: 20m x 20m Quadrant, Includes Boulders w/ Intermediate Axis ≥ 30 cm. Declination: 5°2' W																			
Boulder ID#	Pitted	Mx. Pit Dpth (cm)	Avg. Pit Dpth (cm)	Split	Ht. Resist. Grains (Mx) (cm)	Exfoliation ± Spalling	Boulder Relief (cm)	Intermediate Axis (cm)	Long Axis (cm)	Short Axis (cm)	Angularity	Ventifaction	Ventifaction Orientation (°)	Mx. Ventifaction (cm)	Avg. Ventifaction (cm)	Fracture	Composition	GPS ID#	Comments
1	Y	0.2	0.12	N	0.2	N	22.2	49.8	56	22.2	SR	Y	326	-	-	N	A	df4-bc1	
2	N	-	-	Y	0.4	N	15.2	32.5	55	15.2	SR	Y	307	-	-	Y	I	df4-bc2	
3	Y	0.1	0.1	N	-	N	32	32	37	26.4	R	Y	290	-	-	N	A	df4-bc3	
4	N	-	-	N	-	Y	22	30.8	37	22	R	Y	324	-	-	N	A	df4-bc4	
5	Y	0.2	0.13	N	-	N	25.2	33.2	41.8	25.2	R	Y	304	-	-	N	A	df4-bc5	
6	Y	0.2	0.16	N	-	Y	23.2	25	38	23.2	R	Y	327	-	-	N	A	df4-bc6	
7	N	-	-	N	0.1	N	27	36	38.2	27	A	Y	328	0.6	0.25	N	A	df4-bc7	
8	Y	0.4	0.19	N	0.1	N	21.8	32	38	21.8	SR	Y	-	-	-	N	A	df4-bc8	
9	Y	0.4	0.15	N	0.4	N	16	40	42	16	SA	Y	317	3.2	2.25	N	I	df4-bc9	
10	N	-	-	N	0.1	N	19	31.2	41.5	19	R	Y	311	-	-	N	A	df4-bc10	
11	N	-	-	N	0.1	Y	19.4	30.2	45	19.4	R	Y	-	-	-	N	A	df4-bc11	
12	Y	0.3	0.19	N	0.2	N	18	53	55.5	18	SR	Y	312	0.4	0.27	N	A	df4-bc12	
13	Y	0.6	0.37	N	0.2	N	16.4	38	50.2	16.4	R	Y	301	0.3	0.21	N	A	df4-bc13	
14	Y	0.3	0.15	N	-	N	23.6	43.2	47	23.6	SR	Y	329	-	-	N	A	df4-bc14	
15	N	-	-	N	0.3	N	37.8	36	52	37.8	SA	N	-	-	-	N	I	df4-bc15	Shielded
16	Y	0.9	0.72	N	5	N	30.8	45	52	30.8	SR	Y	312	0.9	0.557	N	I	df4-bc16	
17	N	-	-	N	0.2	N	27.4	57.2	81	27.4	R	Y	315	1	0.7	N	I	df4-bc17	
18	N	-	-	N	0.1	N	14	35.2	43	14	SR	Y	210	1.1	0.74	N	I	df4-bc18	
19	Y	0.7	0.38	N	0.9	N	45.7	57	73.2	45.7	SA	Y	327	-	-	Y	I	df4-bc19	
20	N	-	-	N	0.5	N	21.4	42	48.3	21.4	SA	Y	330	0.7	0.483	N	I	df4-bc20	
21	N	-	-	N	0.5	N	16	34.5	39.9	16	SA	N	-	-	-	N	I	df4-bc21	
22	N	-	-	N	0.7	N	30.6	43.4	50.2	30.6	SA	Y	315	3.9	1.8	N	I	df4-bc22	
23	N	-	-	N	0.8	N	18.9	35.2	54	18.9	SR	Y	331	0.5	0.366	N	I	df4-bc23	
24	N	-	-	N	-	N	8	55	64.6	8	SR	Y	300	-	-	N	I	df4-bc24	
25	N	-	-	N	0.5	N	28	43	52.8	28	SA	Y	330	2.3	1.26	Y	I	df4-bc25	
26	N	-	-	N	0.7	N	13.2	36	45	13.2	SA	Y	321	-	-	N	I	df4-bc26	
27	Y	0.5	0.29	N	0.5	N	17.2	48	69	17.2	SR	Y	300	3.1	1.5	N	I	df4-bc27	
28	N	-	-	N	0.5	N	13.3	37	45	13.3	SA	Y	328	-	-	Y	I	df4-bc28	
29	Y	0.1	0.1	N	0.4	N	26.2	43.6	46	26.2	SR	Y	310	1.3	0.82	N	I	df4-bc29	
30	Y	0.3	0.15	N	0.1	N	18.4	35	45.2	18.4	SR	Y	340	-	-	N	I	df4-bc30	
31	Y	0.6	0.3	N	0.9	N	15.6	39.8	44.2	15.6	SR	Y	312	1.8	0.885	N	I	df4-bc31	Planed
32	Y	0.4	0.27	N	0.1	N	15.4	30.6	43.4	15.4	R	Y	-	-	-	N	I	df4-bc32	
33	N	-	-	N	0.6	N	15.9	37.4	45.2	15.9	SR	Y	328	1.7	0.81	N	I	df4-bc33	
34	N	-	-	N	0.3	Y	19.4	30.1	51.2	19.4	A	Y	306	2.2	1.11	N	I	df4-bc34	
35	Y	0.4	0.23	N	0.2	N	14.9	34	46.1	14.9	SA	Y	321	1	0.65	N	I	df4-bc35	
36	Y	1.3	0.6	N	0.6	Y	16.2	46.3	63.1	16.2	SR	Y	315	-	-	Y	I	df4-bc36	
37	N	-	-	N	0.5	N	22.6	38.2	40.6	22.6	SA	Y	316	1	0.75	N	I	df4-bc37	
38	N	-	-	N	0.1	N	4.9	31.5	39.6	4.9	SR	Y	310	-	-	N	I	df4-bc38	
39	Y	0.2	0.11	N	0.4	N	37.1	38.9	49.2	37.1	SR	Y	305	1.1	0.85	Y	I	df4-bc39	
40	Y	0.1	0.1	N	-	N	18.5	34.8	35.6	18.5	R	Y	315	-	-	N	A	df4-bc40	
41	N	-	-	N	0.3	N	20.2	32.4	33.8	20.2	SA	Y	306	-	-	N	I	df4-bc41	
42	N	-	-	N	0.1	N	12.1	44	58.2	12.1	SA	Y	307	-	-	N	I	df4-bc42	
43	N	-	-	N	0.5	N	25.5	32	65.8	25.5	SA	Y	313	3.5	2.05	N	I	df4-bc43	
44	Y	1.2	0.31	N	0.1	N	33.4	59.2	86.5	33.4	SA	Y	324	-	-	Y	I	df4-bc44	
45	N	-	-	N	0.1	N	20.9	48	54.9	20.9	SR	Y	285	-	-	N	I	df4-bc45	Shielded
46	Y	1.5	0.66	N	0.3	N	21.6	44.8	69.4	21.6	R	Y	332	-	-	N	I	df4-bc46	
47	Y	0.9	0.56	N	0.8	Y	29.9	46	53.5	29.9	R	Y	-	-	-	N	I	df4-bc47	
48	Y	0.6	0.29	N	0.3	N	41.9	41	61.8	41.9	SR	Y	324	-	-	N	I	df4-bc48	
49	N	-	-	N	1.4	N	36.4	49.3	62	36.4	SA	Y	307	3.7	2.44	N	I	df4-bc49	
50	N	-	-	N	0.2	N	14.4	33	47.4	14.4	SA	Y	331	-	-	N	I	df4-bc50	

Debris Flow ID#: Qd1A, Debris Flow #4, Middle CONT.									Date: 7/27/2014									
Comments: 20m x 20m Quadrant, Includes Boulders w/ Intermediate Axis ≥ 30 cm. Declination: 5°2' W																		
Boulder ID#	Pitted	Mx. Pit Dpth (cm)	Avg. Pit Dpth (cm)	Split	Ht. Resist. Grains (Mx) (cm)	Exfoliation ± Spalling	Boulder Relief (cm)	Intermediate Axis (cm)	Long Axis (cm)	Short Axis (cm)	Angularity	Ventifaction	Ventifaction Orientation (°)	Mx. Ventifaction (cm)	Avg. Ventifaction (cm)	Fracture	Composition	GPS ID#	Comments
51	N	-	-	N	0.7	N	27.4	36.1	45.9	27.4	SR	Y	319	2.6	1.5	N	I	df4-bc51	
52	Y	1.5	0.72	N	0.4	N	25.1	36.3	40.5	25.1	SR	Y	316	-	-	N	I	df4-bc52	
53	N	-	-	N	0.1	N	29.9	41.8	71	29.9	SR	Y	334	-	-	N	I	df4-bc53	
54	N	-	-	N	0.6	N	40.7	53.2	75.5	40.7	SA	Y	310	1.5	0.944	N	I	df4-bc54	
55	N	-	-	N	0.3	N	21.3	54.7	82	21.3	SR	Y	314	-	-	Y	I	df4-bc55	
56	Y	0.4	0.25	N	0.2	N	30.2	36.7	60.3	30.2	SR	Y	311	1.2	0.89	N	I	df4-bc56	
57	Y	0.2	0.11	N	0.7	Y	35	38.5	50.7	35	SR	Y	296	6.7	1.86	Y	I	df4-bc57	
58	Y	0.5	0.2	N	1.4	Y	23.2	35.4	58.5	23.2	SA	Y	316	-	-	N	I	df4-bc58	
59	N	-	-	N	1.3	N	23.9	40	56.8	23.9	SR	Y	327	-	-	N	I	df4-bc59	
60	N	-	-	N	2	N	27	48.9	53.6	27	SR	Y	304	3	1.71	N	I	df4-bc60	
61	N	-	-	N	0.4	N	21.9	70	85.5	21.9	SA	Y	300	-	-	N	I	df4-bc61	
62	Y	0.3	0.19	N	0.3	N	32.6	35	43.8	32.6	R	Y	-	-	-	N	A	df4-bc62	
63	N	-	-	N	0.3	N	31.6	47.2	62.4	31.6	SR	Y	323	-	-	N	I	df4-bc63	
64	N	-	-	N	0.1	N	12.4	33.2	42	12.4	SA	Y	325	1.8	0.85	N	I	df4-bc64	
65	Y	0.4	0.233	N	0.2	N	21.2	31.2	45.3	21.2	R	Y	336	-	-	N	I	df4-bc65	
66	Y	2.1	1.16	N	1.1	N	52.3	61.8	83.2	52.3	R	Y	329	-	-	N	I	df4-bc66	
67	N	-	-	N	0.4	N	50.9	72	77.7	50.9	SA	Y	294	1.7	0.78	Y	I	df4-bc67	
68	N	-	-	Y	1	N	27.7	34.6	46	27.7	SR	Y	301	1.1	0.688	Y	I	df4-bc68	
69	Y	0.1	0.1	N	-	N	21.2	37.5	47	21.2	R	Y	-	-	-	N	A	df4-bc69	
70	N	-	-	N	0.2	N	25.4	35	95	25.4	SA	Y	316	-	-	N	I	df4-bc70	
71	N	-	-	N	0.6	N	30.2	33.6	62.5	30.2	SA	Y	326	1.6	0.63	N	I	df4-bc71	
72	N	-	-	N	0.2	N	24.7	57	69.8	24.7	SA	N	-	-	-	N	I	df4-bc72	
73	Y	1.3	0.45	N	0.3	Y	51.8	51.8	107.2	32.3	SA	Y	326	-	-	N	I	df4-bc73	
74	N	-	-	N	1.3	N	29.5	59.8	75	29.5	SR	Y	293	-	-	N	I	df4-bc74	Shielded
75	Y	0.1	0.1	N	-	N	28.6	47.7	54	28.6	R	Y	-	-	-	N	A	df4-bc75	
76	N	-	-	N	0.7	N	47.2	61.2	81	47.2	SR	Y	305	-	-	N	I	df4-bc76	
77	N	-	-	N	1.5	N	41.5	53	82.9	41.5	SA	Y	287	-	-	N	I	df4-bc77	Shielded
78	N	-	-	N	0.9	N	20	42.8	60	20	SA	Y	-	-	-	N	I	df4-bc78	
79	N	-	-	N	0.5	N	39.6	39.8	53.7	22.3	SA	Y	310	2	1.05	N	I	df4-bc79	

Angularity- R: Rounded, SR: Subrounded, SA: Subangular, A: Angular. *Lithology*- A: Andesite, I: Ignimbrite. *Ventifaction/Split/Pitting/Exfoliation/Fractur*e- Y: Yes, N: No.

Debris Flow ID#: Qd1A,Debris Flow #4, Proximal								Date: 7/28/2014										
Comments: 30m x 30m Quadrant, Includes Boulders w/ Intermediate Axis ≥ 30 cm. Declination: 5°2' W																		
Boulder ID#	Pitted	Mx. Pit Dpth (cm)	Avg. Pit Dpth (cm)	Split	Ht. Resist. Grains (Mx) (cm)	Exfoliation ± Spalling	Boulder Relief (cm)	Intermediate Axis (cm)	Long Axis (cm)	Short Axis (cm)	Angularity	Ventifaction	Ventifaction Orientation (°)	Mx. Ventifaction (cm)	Avg. Ventifaction (cm)	Fracture	Composition	GPS ID#	Comments
1	Y	0.5	0.3	N	0.5	N	36.2	36.2	43.8	18.2	A	Y	309	22.5	6.09	Y	I	df4-bc1	
2	N	-	-	N	-	N	11.5	11.5	60	10.6	A	Y	311	9.1	4.83	Y	I	df4-bc2	
3	N	-	-	N	-	N	6	14.3	22	6	SA	Y	303	7.7	4.25	N	I	df4-bc3	
4	Y	1.3	0.6	N	-	N	12.4	16.3	27.3	12.4	R	Y	315	-	-	N	A	df4-bc4	
5	Y	1.4	0.85	N	1.6	N	19	28.3	30.1	19	A	Y	314	15.7	8.96	N	I	df4-bc5	
6	Y	0.5	0.2	N	-	N	6.5	13.2	20.9	6.5	A	Y	322	11.6	5.73	N	I	df4-bc6	
7	Y	0.9	0.56	N	0.3	N	12.3	31.5	32	12.3	SR	Y	322	4.6	3.05	N	I	df4-bc7	
8	Y	0.5	0.2	N	0.4	N	19.6	27	32.2	19.6	SR	Y	297	8.3	5.09	Y	I	df4-bc8	
9	Y	0.3	0.11	N	0.4	N	34.8	34.8	48.2	25.4	A	Y	315	13	4.1	N	I	df4-bc9	
10	Y	0.7	0.38	N	1.3	N	22	26	35.3	22	SR	Y	317	6.8	3.45	N	I	df4-bc10	
11	N	-	-	N	0.2	N	9.6	17.3	20.3	9.6	SR	Y	310	10.4	4.12	N	I	df4-bc11	
12	Y	1.3	0.7	N	0.5	N	21.7	33.8	49.8	21.7	SR	Y	327	10.4	5.17	N	I	df4-bc12	
13	Y	1.3	0.6	N	0.7	N	33	40.2	57.4	33	R	Y	307	18.3	9.78	N	I	df4-bc13	

Angularity- R: Rounded, SR: Subrounded, SA: Subangular, A: Angular. *Lithology*- A: Andesite, I: Ignimbrite. *Ventifaction/Split/Pitting/Exfoliation/Fractu*re- Y: Yes, N: No.

Debris Flow ID#: Qd1F, Debris Flow #5, Distal								Date: 7/29/2014											
Comments: Random Walk used to select 30 boulders. Declination: 5°2' W. Quick Boulder Count, No GPS locations of boulders taken.																			
Boulder ID#	Pitted	Mx. Pit Dpth (cm)	Avg. Pit Dpth (cm)	Split	Ht. Resist. Grains (Mx) (cm)	Exfoliation ± Spalling	Boulder Relief (cm)	Intermediate Axis (cm)	Long Axis (cm)	Short Axis (cm)	Angularity	Ventifaction	Ventifaction Orientation (°)	Mx. Ventifaction (cm)	Avg. Ventifaction (cm)	Fracture	Composition	GPS ID#	Comments
1								70			SR						I		
2								51.2			SA						I		
3								51			R						A		
4								52			SR						A		
5								46			SR						I		
6								83.1			SR						A		
7								62			SA						I		
8								127.5			SA						A		
9								34			SA						A		
10								62			R						I		
11								37.5			R						I		
12								64.5			SR						A		
13								65.8			SA						I		
14								56.5			R						A		
15								121			SR						I		
16								42			SR						A		
17								39.5			R						A		
18								32			SR						I		
19								50			SA						I		
20								26.5			SR						I		
21								46			R						A		
22								31			SR						A		
23								33			SR						I		
24								24.5			SR						I		
25								55			SR						I		
26								52.5			SR						A		
27								54			SR						I		
28								47.5			R						A		
29								53.2			SA						A		
30								53.1			SR						I		

Angularity- R: Rounded, SR: Subrounded, SA: Subangular, A: Angular. *Lithology*- A: Andesite, I: Ignimbrite. *Ventifaction/Split/Pitting/Exfoliation/Fractu*re- Y: Yes, N: No.

Qd1E, Debris Flow ID#: Debris Flow #6, Distal									Date: 7/29/2014										
Comments: Random Walk Boulder Count. Declination: 5°2' W. No GPS locations taken for selected boulders.																			
Boulder ID#	Pitted	Mx. Pit Dpth (cm)	Avg. Pit Dpth (cm)	Split	Ht. Resist. Grains (Mx) (cm)	Exfoliation ± Spalling	Boulder Relief (cm)	Intermediate Axis (cm)	Long Axis (cm)	Short Axis (cm)	Angularity	Ventifaction	Ventifaction Orientation (°)	Mx. Ventifaction (cm)	Avg. Ventifaction (cm)	Fracture	Composition	GPS ID#	Comments
1	Y	0.1	0.1	N	-	N	32	72	75	32	SR	Y				N	I		
2	N	-	-	N	-	N	13	36	37	13	R	Y				N	I		
3	N	-	-	N	-	N	12	27	32	12	SR	Y				N	I		
4	N	-	-	N	-	N	20	47	60	20	SR	Y				N	I		
5	Y	0.3	0.17	Y	0.5	N	41	69	93	41	R	Y				Y	I		
6	Y	0.1	0.1	N	0.1	N	12	30	39	12	R	Y				N	I		
7	N	-	-	N	0.1	N	24.2	61	69	24.2	R	Y				N	I		
8	N	-	-	Y	-	Y	18.1	35	47	18.1	SA	Y				N	I		
9	N	-	-	N	-	N	9.1	13	21	9.1	R	Y				N	I		
10	Y	0.1	0.1	N	0.1	N	35	35	44	35	R	N				N	I		
11	N	-	-	N	-	N	12.8	23	32	12.8	R	N				N	I		
12	N	-	-	Y	-	N	47	82	75	47	R	Y				N	I		
13	Y	0.1	0.1	N	0.1	N	13	28	35	13	R	Y				N	I		
14	N	-	-	N	-	N	11.1	22	26	11.1	R	N				N	I		
15	Y	0.1	0.1	N	-	N	14.6	27	34	14.6	R	Y				N	I		
16	N	-	-	Y	-	Y	48	80.2	108	48	SA	Y				N	I		
17	N	-	-	N	-	Y	14	23	27	14	R	N				N	I		
18	Y	0.1	0.1	N	-	N	10	41	48	10	R	N				N	I		
19	N	-	-	N	-	N	25.5	41	60	25.5	R	Y				N	I		
20	Y	0.1	0.1	N	-	N	26.3	32	43	26.3	R	Y				N	I		
21	Y	0.1	0.1	N	0.1	N	20.4	38	62	20.4	SR	Y				N	I		
22	Y	0.1	0.1	N	-	N	28.7	32	59	28.7	SA	Y				N	I		
23	N	-	-	N	-	N	19	21	29	19	R	N				N	I		
24	N	-	-	N	-	Y	23	31	45	23	R	Y				N	I		
25	Y	0.1	0.1	N	-	N	13	27	31	13	R	N				N	I		
26	N	-	-	N	-	N	20	33	28	20	R	N				N	I		

Angularity- R: Rounded, SR: Subrounded, SA: Subangular, A: Angular. *Lithology*- A: Andesite, I: Ignimbrite. *Ventifaction/Split/Pitting/Exfoliation/Fractu*re- Y: Yes, N: No.

Qd1E, Debris Flow ID#: Debris Flow #6, Middle								Date: 7/29/2014										
Comments: Random Walk Boulder Count. Declination: 5°2' W. No GPS locations taken for selected boulders.																		
Boulder ID#	Pitted	Mx. Pit Dpth (cm)	Avg. Pit Dpth (cm)	Split	Ht. Resist. Grains (Mx) (cm)	Exfoliation ± Spalling	Boulder Relief (cm)	Intermediate Axis (cm)	Long Axis (cm)	Short Axis (cm)	Angularity	Ventifaction	Ventifaction Orientation (°)	Mx. Ventifaction (cm)	Avg. Ventifaction (cm)	Fracture	Composition	GPS ID#	Comments
19	N	-	-	N	-	N	17	55	77	17	SA	Y				Y	A		
1	Y	0.4	0.27	N	0.1	Y	110	174	206	110	SR	Y	325			Y	I		
2	Y	0.6	0.36	N	0.1	N	87	133	211	87	R	Y	310			Y	I		
3	Y	0.2	0.14	Y	-	Y	92	193	281	92	SR	Y	311			N	I		
4	N	-	-	N	-	N	36	41	47	36	SA	Y				Y	I		
5	Y	0.3	0.15	N	-	Y	61	115	151	61	SA	Y				N	I		
6	Y	0.3	0.13	N	-	Y	58	83	96	58	SA	Y				N	I		
7	N	-	-	Y	0.2	Y	66	116	138	66	SR	Y				Y	I		
8	N	-	-	N	-	Y	22	49	85	22	SR	Y				N	I		
9	Y	0.5	0.34	N	-	Y	30	106	111	30	R	Y				N	I		
10	N	-	-	Y	0.1	Y	42	132	190	42	SR	Y				Y	I		
11	N	-	-	N	-	Y	18	54	87	18	R	Y				N	I		
12	Y	0.2	0.15	Y	0.1	Y	42	119	143	42	SR	Y				Y	I		
13	N	-	-	N	0.1	N	17	35	75	17	SR	Y				N	I		
14	Y	0.1	0.1	N	0.1	N	30	44	86	30	R	Y				N	I		
15	N	-	-	N	-	Y	51	157	222	51	R	Y				Y	I		
16	N	-	-	N	-	Y	37	62	80	37	R	Y				N	I		
17	N	-	-	N	-	Y	81	218	293	81	SR	Y				N	I		
18	Y	0.3	0.17	N	0.1	Y	39	87	107	39	SR	Y				N	I		
20	Y	0.1	0.1	N	-	N	30	45	75	30	R	Y				N	I		
21	N	-	-	Y	-	Y	34	75	105	34	R	Y				N	I		
22	Y	0.1	0.1	N	-	Y	34	79	120	34	R	Y				N	I		
23	Y	0.1	0.1	Y	-	N	21	28	34	21	R	Y				N	I		
24	Y	0.2	0.1	N	-	N	55	47	71	55	R	Y				N	I		
25	Y	0.5	0.28	N	-	Y	42	127	161	42	SR	Y				N	I		
26	Y	0.1	0.1	N	-	N	35	35	55	35	R	Y				N	I		

Angularity- R: Rounded, SR: Subrounded, SA: Subangular, A: Angular. *Lithology*- A: Andesite, I: Ignimbrite. *Ventifaction/Split/Pitting/Exfoliation/Fractu*re- Y: Yes, N: No.

Debris Flow ID#: Qd1G, Debris Flow #7, Canyon								Date: 7/28/2014											
Comments: Random Walk Boulder Count, Canyon Flow. Declination: 5°2' W. No GPS Locations taken for individual boulders.																			
Boulder ID#	Pitted	Mx. Pit Dpth (cm)	Avg. Pit Dpth (cm)	Split	Ht. Resist. Grains (Mx) (cm)	Exfoliation ± Spalling	Boulder Relief (cm)	Intermediate Axis (cm)	Long Axis (cm)	Short Axis (cm)	Angularity	Ventifaction	Ventifaction Orientation (°)	Mx. Ventifaction (cm)	Avg. Ventifaction (cm)	Fracture	Composition	GPS ID#	Comments
1	Y	0.4	0.28				48	56	75	48	R	N				N	A		
4	Y	0.3	0.23				51.5	37	43.8	51.5	R	N				N	A		
6	Y	0.3	0.18				28.3	36	72	28.3	SR	N				N	A		
8	N	-	-				29.8	73	96	29.8	SA	N				N	A		
15	Y	0.5	0.24				32	125	148.6	32	SR	N				N	A		
18	Y	0.2	0.18				46	48	51.6	46	R	N				N	A		
20	Y	0.1	0.1				24	30	47	24	SR	N				N	A		
21	Y	0.2	0.14				25	34	39.5	25	R	N				N	A		
23	N	-	-				13.7	32	37	13.7	SA	N				N	A		
24	N	-	-				28	32	64	28	SA	N				N	A		
25	Y	0.4	0.22				32	37	43	32	R	N				N	A		
26	Y	0.3	0.16				33.4	46.2	47	33.4	SR	N				N	A		
27	N	-	-				30.2	82	85	30.2	SR	N				N	A		
28	N	-	-				39	55	87.4	39	SR	N				N	A		
30	Y	0.4	0.27				36	44	62	36	R	N				N	A		
2	N	-	-				15	32	32.2	15	SA	N				N	I		
3	N	-	-				39.8	63	82	39.8	SR	N				N	I		
5	N	-	-				87	100.3	124	87	SR	N				Y	I		
7	Y	2.2	0.87				64	86	177	64	SA	N				N	I		
9	Y	0.4	0.16				23	50	81	23	R	N				N	I		
10	N	-	-				47.2	95	110	47.2	SR	N				Y	I		
11	Y	0.4	0.2				96	104	130	96	R	N				N	I		
12	Y	0.3	0.18				52.4	73	84.5	52.4	SR	N				N	I		
13	Y	0.3	0.13				20	47..2	52.8	20	A	N				N	I		
14	Y	0.9	0.48				29.6	52.4	77	29.6	SA	N				N	I		
16	Y	0.2	0.12				17	33	44.8	17	SR	N				N	I		
17	N	-	-				33	51.2	123	33	SA	N				N	I		
19	Y	0.3	0.15				31	70.2	75.4	31	SA	N				N	I		
22	N	-	-				41	85	112	41	SR	N				N	I		
29	Y	0.3	0.21				56	58	67.5	56	R	N				N	I		

Angularity- R: Rounded, SR: Subrounded, SA: Subangular, A: Angular. *Lithology*- A: Andesite, I: Ignimbrite. *Ventifaction/Split/Pitting/Exfoliation/Fractu*re- Y: Yes, N: No.

APPENDIX B: Accelerator Mass Spectrometry (AMS) Results

Purdue University PRIME Lab										
	Date: 12/3/2014							Ward & Cesta ^{36}Cl Results		
Sample Name	**User ID**	**Sample Mass(g)**	**Dilution Spike(mg)**	**^{36}Cl Ratio (x10^{-15})**	**^{35}Cl/^{37}Cl Stable Ratio**	**Total Weight Chlorine (mg)**	**Corrected Weight Chlorine (mg)**	**Corrected ^{36}Cl Atoms (x10^{6})**	**Corrected ^{36}Cl Atoms/Gr$_{Rock}$(x10^{6})**	**Chloride in Rock (ppm)**
DF1-B1-14	201402964	29.38	0.9817	336.15 ± 8.87	3.710 ± 0.012	6.9313 ± 0.1430	6.883 ± 0.143	45.168 ± 1.447	1.537 ± 0.049	234.3 ± 4.88
DF1-B2-14	201402961	29.63	0.991517	348.967 ± 8.56	3.604 ± 0.017	8.5594 ± 0.3056	8.511 ± 0.306	56.602 ± 2.284	1.910 ± 0.077	287.2 ± 10.32
DF1-B3-14	201402962	30.12	1.011151	2454.3 ± 45.62	4.015 ± 0.068	4.6822 ± 0.3596	4.633 ± 0.360	237.857 ± 15.634	7.897 ± 0.519	153.8 ± 11.95
DF6-B1-14	201402963	29.66	0.9817	276.643 ± 6.14	3.829 ± 0.042	5.7540 ± 0.3451	5.705 ± 0.345	31.621 ± 1.768	1.066 ± 0.046	192.4 ± 11.64
DF6-B2-14	201402965	30.12	1.011151	188.322 ± 4.79	3.811 ± 0.044	6.0829 ± 0.3922	6.034 ± 0.392	22.635 ± 1.382	0.751 ± 0.060	200.3 ± 13.03
DF6-B3-14	201402966	30.01	0.991517	207.768 ± 4.54	3.617 ± 0.037	8.3320 ± 0.6302	8.283 ± 0.630	32.856 ± 2.338	1.095 ± 0.078	276.0 ± 21.00
AF-6-14	201402967	30	1.001334	5325.59 ± 65.18	4.141 ± 0.076	4.0588 ± 0.3053	4.010 ± 0.305	458.951 ± 28.185	15.298 ± 0.940	133.7 ± 10.18
AF-5-14	201402968	30.01	0.991517	2438.32 ± 35.88	4.221 ± 0.038	3.7241 ± 0.1298	3.675 ± 0.130	195.799 ± 6.102	6.524 ± 0.0203	122.5 ± 4.34
AF-2-14	201402969	30.12	0.9817	1295.34 ± 20.33	4.699 ± 0.013	2.5618 ± 0.0213	2.513 ± 0.021	78.176 ± 1.315	2.595 ± 0.044	83.4 ± 0.79
AF-1-14	201402970	30.01	0.9817	1108.43 ± 17.98	7.037 ± 0.078	1.0216 ± 0.0207	0.973 ± 0.021	37.878 ± 0.729	1.262 ± 0.024	32.4 ± 0.78
AF-1-13	201403412	26.6746	1.04943675	2974.66 ± 86.61	10.550 ± 0.120	0.5682 ± 0.0094	0.287 ± 0.010	82.393 ± 2.448	3.088,811 ± 0.092	10.7 ± 0.39
AF-2-13	201403413	28.9308	1.05140005	3434.82 ± 72.03	10.530 ± 0.149	0.5708 ± 0.0118	0.289 ± 0.013	95.421± 2.117	3.298,244 ± 0.073	10.0 ± 0.43
AFDP-1-14	201403414	30.1948	1.02959706	3054.95 ± 64.77	7.834 ± 0.109	0.8875 ± 0.0209	0.606 ± 0.021	100.150 ± 2.386	3.316,798 ± 0.079	20.1 ± 0.71
AFDP-2-14	201403415	30.7352	1.05987325	4033.35 ± 83.86	9.294 ± 0.085	0.6938 ± 0.0098	0.412 ± 0.011	121.075 ± 2.607	3.939,304 ± 0.085	13.4 ± 0.35
AFDP-35-14	201403416	29.6787	1.06255987	3182.55 ± 68.78	10.581 ± 0.032	0.5728 ± 0.0025	0.291 ± 0.005	89.127 ± 1.936	3.003,066 ± 0.065	9.8 ± 0.17
AFDP-65-14	201403417	30.5703	1.04086021	2317.45 ± 39.88	9.146 ± 0.044	0.6984 ± 0.0052	0.417 ± 0.007	68.958 ± 1.206	2.255,725 ± 0.059	13.6 ± 0.22
AFDP-200-14	201403418	29.7221	1.05284669	576.523 ± 11.75	8.426 ± 0.121	0.8045 ± 0.0187	0.523 ± 0.019	18.254 ± 0.418	0.614,152 ± 0.014	17.6 ± 0.65
AFDP-400-14	201403419	30.0059	1.09376604	174.487 ± 5.36	8.472 ± 0.145	0.8285 ± 0.0229	0.547 ± 0.023	5.664 ± 0.192	0.188,752 ± 0.006	18.2 ± 0.78
AFDP-500-14	201403420	30.219	1.03827692	136.063 ± 4.04	9.093 ± 0.136	0.7030 ± 0.0164	0.421 ± 0.017	3.979 ± 0.132	0.131,679 ± 0.004	13.9 ± 0.56
AFDP-600-14	201403421	30.0011	1.05388001	123.634 ± 4.22	9.661 ± 0.098	0.6503 ± 0.0100	0.369 ± 0.011	3.531 ± 0.130	0.117,693 ± 0.004	12.3 ± 0.36
Blanks										
AF-14-BLK1	201402972	-	0.991517	6.20317 ± 3.765	63.665 ± 11.182	-	-	-	-	-
AF-14-BLK2	201402971	-	1.001334	5.15013 ± 1.698	73.911 ± 21.227	-	-	-	-	-
AFDP-14-BLK1	201403422	-	1.03683028	2.28129 ± 1.632	15.532 ± 0.209					
AFDP-14-BLK2	201403423	-	1.03114703	4.77844 ± 1.788	20.278 ± 0.453					
CRASH 2A	201500504	-	-	14.78 ± 0.88	79.48 ± 4.26	-	-	-	-	-
CRASH 2B	201500505	-	-	15.81 ± 1.02	73.35 ± 2.86	-	-	-	-	-

Purdue University PRIME Lab										
	Date: 4/24/2015							Ward & Cesta ^{36}Cl Results		
Sample Name	User ID	Sample Mass(g)	Dilution Spike(mg)	^{36}Cl Ratio ($x10^{-15}$)	^{35}Cl/^{37}Cl Stable Ratio	Total Weight Chlorine (mg)	Corrected Weight Chlorine (mg)	Corrected ^{36}Cl Atoms ($x10^{6}$)	Corrected ^{36}Cl Atoms/Gr_{Rock} ($x10^{6}$)	Chloride in Rock (ppm)
AF-3-14	201500497	29.6693	1.13995531	1043.27 ± 25.57	4.85 ± 0.07	2.7095 ± 0.1122	2.185 ± 0.113	67.717 ± 2.602	2.282 ± 0.088	73.7 ± 3.80
AF-4-14	201500498	28.7964	1.24359701	29.74 ± 2.04	2.99 ± 0.02	-37.1866 ± 5.656	-37.711 ± 5.656	-18.961 ± 3.117	-0.658 ± 0.108	-1309.6 ± 196.2
Blanks										
AF14-Blank A	201500500	-	0.9954976	30.36 ± 1.82	9.15 ± 0.18	-	-	-	-	-
AF14-Blank B	201500501	-	1.23295384	24.98 ± 1.74	15.89 ± 0.16	-	-	-	-	-
CRASH 2A	201500504	-	-	14.78 ± 0.88	79.48 ± 4.26	-	-	-	-	-
CRASH 2B	201500505	-	-	15.81 ± 1.02	73.35 ± 2.86	-	-	-	-	-

Purdue University PRIME Lab										
	Date: 4/24/2015							Ward & Cesta ^{36}Cl Results		
Sample Name	User ID	Sample Mass(g)	Dilution Spike(mg)	^{36}Cl Ratio ($x10^{-15}$)	^{35}Cl/^{37}Cl Stable Ratio	Total Weight Chlorine (mg)	Corrected Weight Chlorine (mg)	Corrected ^{36}Cl Atoms ($x10^{6}$)	Corrected ^{36}Cl Atoms/Gr_{Rock} ($x10^{6}$)	Chloride in Rock (ppm)
AF-3-13	201402210	30.00	0.9817	2925.17 ± 84.88	7.560 ± 0.132	0.8994 ± 0.0272	0.859 ± 0.027	93.973 ± 3.048	3.132 ± 0.101	28.6 ± 0.91
AF-4-13	201402211	30.00	0.9817	2158.94 ± 78.61	5.625 ± 0.109	1.6070 ± 0.707	1.567 ± 0.071	95.262 ± 4.336	3.175 ± 0.144	52.2 ± 2.36
DF3-B1-14	201402212	29.29	0.9817	1124.9 ± 33.42	3.523 ± 0.065	10.2110 ± 1.6783	10.171 ± 1.678	213.981 ± 32.699	7.306 ± 1.116	347.2 ± 57.30
DF3-B2-14	201402213	29.89	0.9817	204.615 ± 6.62	3.514 ± 0.048	10.4488 ± 1.2977	10.409 ± 1.298	39.605 ± 4.691	1.325 ± 0.156	348.2 ± 43.42
Blanks										
AF13-Blank A	201402986	-	1.0779066	6.13 ± 1.49	23.78 ± 1.58	-	-	-	-	-
AF13-Blank B	201402985	-	0.9817023	144.13 ± 7.83	35.33 ± 0.30	-	-	-	-	-
CRASH 1A		-	-	16.23 ± 1.07	70.74 ± 1.80	-	-	-	-	-
CRASH 1B		-	-	16.10 ± 1.03	81.29 ± 1.73	-	-	-	-	-

APPENDIX C: Optically Stimulated Luminescence (OSL) Aliquot Results

Sample Name		Disk Type	Thin	Weighted Mean		Sample Dose Rate	
TOC-OSL1		0.1165	0.0023	Calculation (Gy)		2.53	0.13
Dose (Sec)		Dose (Gy)		μ/s²	1/s²	Indiv. Alq Age(ka)	
979.89	43.86	114.12	5.58	3.66	0.03	45.20	3.25
1232.58	57.67	143.55	7.29	2.70	0.02	56.85	4.16
2694.26	248.79	313.79	29.63	0.36	0.00	124.27	13.44
1200.73	56.33	139.84	7.12	2.76	0.02	55.38	4.06
793.95	30.81	92.47	4.03	5.70	0.06	36.62	2.50
762.52	45.81	88.81	5.62	2.82	0.03	35.17	2.89
1080.44	35.18	125.83	4.79	5.48	0.04	49.83	3.24
883.59	30.09	102.91	4.05	6.27	0.06	40.76	2.68
1072.54	30.60	124.91	4.33	6.65	0.05	49.47	3.12
1021.37	29.07	118.95	4.12	7.01	0.06	47.11	2.97
1592.50	50.86	185.47	6.96	3.82	0.02	73.45	4.75
827.79	50.87	96.41	6.22	2.49	0.03	38.18	3.18
1009.32	35.95	117.55	4.79	5.13	0.04	46.55	3.10
1037.17	34.12	120.79	4.63	5.62	0.05	47.84	3.12
652.65	19.93	76.01	2.76	9.95	0.13	30.10	1.93
1007.46	38.56	117.33	5.05	4.59	0.04	46.47	3.16
3582.01	222.75	417.18	27.22	0.56	0.00	165.22	13.85
1282.44	47.04	149.36	6.22	3.86	0.03	59.15	3.97
1095.07	55.15	127.54	6.90	2.68	0.02	50.51	3.81
855.65	33.49	99.65	4.37	5.22	0.05	39.47	2.70
926.20	25.94	107.87	3.70	7.89	0.07	42.72	2.68
1355.70	48.44	157.89	6.45	3.80	0.02	62.53	4.17
674.05	22.93	78.50	3.09	8.23	0.10	31.09	2.04

Sample Name		Disk Type	Thin	Weighted Mean		Sample Dose Rate	
CHAJ-OSL1		0.1165	0.0023	Calculation (Gy)		2.85	0.14
Dose (Sec)		Dose (Gy)		μ/s^2	$1/s^2$	Indiv. Alq Age(ka)	
1546.92	52.37	178.01	7.00	3.63	0.02	62.48	3.90
1036.86	27.12	119.31	3.93	7.73	0.06	41.88	2.45
918.58	22.34	105.70	3.33	9.55	0.09	37.10	2.14
950.64	26.75	109.39	3.78	7.67	0.07	38.40	2.28
944.56	28.02	108.69	3.89	7.19	0.07	38.15	2.30
1703.45	52.72	196.02	7.22	3.76	0.02	68.80	4.19
1380.54	37.91	158.86	5.40	5.46	0.03	55.76	3.30
1033.76	36.46	118.96	4.82	5.12	0.04	41.75	2.64
1114.44	37.60	128.24	5.03	5.07	0.04	45.01	2.81
958.27	33.65	110.27	4.46	5.55	0.05	38.70	2.44
1026.88	46.97	118.16	5.90	3.40	0.03	41.48	2.88
560.82	22.41	64.53	2.88	7.76	0.12	22.65	1.49
588.21	28.78	67.69	3.58	5.29	0.08	23.76	1.70
1406.10	71.59	161.80	8.85	2.07	0.01	56.79	4.15
1002.91	53.86	115.41	6.61	2.64	0.02	40.51	3.04